# *µPlasma patterning and inkjet printing to enhance localized wetting and mixing behaviour*

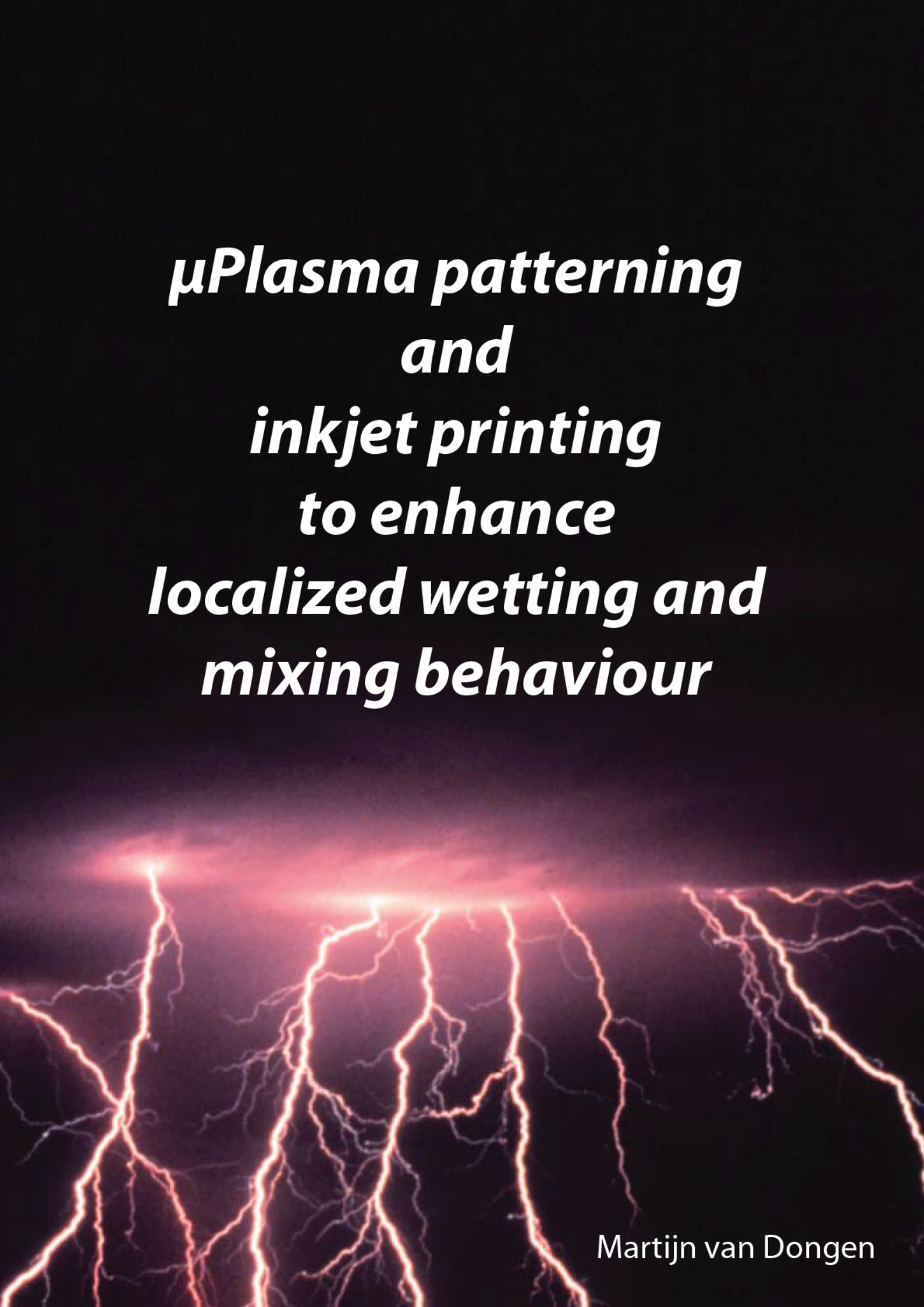

Martijn van Dongen

# µPlasma patterning and inkjet printing to enhance localized wetting and mixing behaviour

Martijn van Dongen
2014

**Samenstelling promotie commissie:**

| | |
|---|---|
| Voorzitter: | Prof. dr. ir. J.W.M. Hilgenkamp |
| Promotor: | Prof. dr. ir. J.F. Dijksman |
| Copromotor: | Dr. J.P.C. Bernards (Fontys Hogescholen) |
| Leden: | Prof. dr.ing. C.W.M. Bastiaansen (Queen Mary University of London) |
| | Prof. dr.ir. A.J. Huis in 't Veld |
| | Prof. dr. D. van der Meer |
| | Prof. dr.ir. J.M.J. den Toonder (Technische Universiteit Eindhoven) |

Nederlandse titel:
µPlasma patroneren en inkjet printen om lokaal de bevochtiging en menging te verbeteren.

Publisher:
M.H.A. van Dongen

Cover illustration:
Time-lapse photography captures multiple cloud-to-ground lightning strokes during a night-time thunderstorm,
NOAA Photo Library, NOAA Central Library; OAR/ERL/National Severe Storms Laboratory (NSSL), Photographer: C. Clark

Print:
Ipskamp Drukkers


ISBN: 978-94-6259-244-5

# μPLASMA PATTERNING AND INKJET PRINTING TO ENHANCE LOCALIZED WETTING AND MIXING BEHAVIOUR

PROEFSCHRIFT

ter verkrijging van
de graad van doctor aan de Universiteit Twente,
op gezag van de rector magnificus,
Prof.dr. H. Brinksma
volgens besluit van het college voor Promoties
in het openbaar te verdedigen
op woensdag 2 juli 2014 om 14.45 uur

door

Martinus Henricus Adrianus van Dongen
Geboren op 16 maart 1970
te Eindhoven

Dit proefschrift is goedgekeurd door:

| | |
|---|---|
| De promotor: | Prof. dr. ir. J.F. Dijksman |
| en de copromotor: | Dr. J.P.C. Bernards (Fontys Hogescholen) |

# *Table of Contents*

# 1 Introduction

This thesis represents the work done on two topics concerning the deposition of functional materials for organic electronics. With a market demand for low cost, easy to produce, flexible and portable applications in healthcare, energy, biomedical or electronics markets, large research programs are initiated to develop new technologies to provide this demand with new innovative ideas. One of these fast developing technologies is organic printed electronics. As the term printed electronics implies, functional materials are printed via, e.g. inkjet, flexo or gravure printing techniques, on to a substrate material. Applications are, among others, organic light emitting diodes (OLED), sensors, radio frequency identification (RFID) tags and Lab-on-a-chip devices. For all these applications, in some way, the interaction of fluids with the substrate is of great importance. The most used substrate materials for these low-cost devices are (coated) paper or plastic. Plastic substrates have a relatively low surface energy which is comparable with the often organically based functional fluids used in printed electronics. This combination of fluids and substrates frequently leads to poor wetting and/or poor adhesion of the fluids on the substrates during printing and post processing. In Lab-on-a-chip devices, liquid samples need to be transported through small capillaries towards test sites. Poor wetting of the liquid in the capillary can prevent the liquid to reach these sites. In order to improve wetting behaviour, several methods have been developed to change the surface energy of both liquid, for instance by adding surfactants, or pre-treatment of the substrate, by e.g. plasma treatment or chemical modification.

The first part of this thesis, i.e. chapter two, is dedicated to gaining knowledfge of the effect of atmospheric plasma treatment on the wetting behaviour of, primarily, plastic substrates by patterned µPlasma treatment. Usually, plasma treatment is used to treat complete surfaces of substrates in order to change its surface energy. In the above mentioned applications, it is not always needed or even wanted to treat the complete surface. Often it is only required to treat selected areas where the functional material will be deposited or capillaries need to be formed. The µPlasma tool investigated in this thesis makes it possible to locally treat substrates with an atmospheric dielectric barrier discharge. An example of this localized change in wetting behaviour is shown in Figure

1.1. A comparison of this tool will be made with industrial UV-Ozone treatment on improving the wettability of polycarbonate and polyethylene naphthalate films. Also, it will be shown that the µPlasma tool can be used as a deposition tool for functional materials by adding precursor materials to the plasma in order to decrease wettability. The last section of chapter two is dedicated to the investigation of the patterning aspect of the µPlasma apparatus, as we study the achievable resolution of the tool.

**Figure 1.1: An example of the change in wettability created by patterned plasma treatment. A monolayer of dodecyl-trichlorosilane (DTS) has been deposited on glass to create a hydrophobic surface. Locally this DTS-layer was removed by patterned atmospheric plasma treatment to create a hydrophilic channel. Liquid placed on the substrate will wet the channel, but not the hydrophobic DTS-layer. The experimental work for this figure was carried out by Tom Vercoulen.**

For printing applications, printing of consecutive droplets onto, or close to each other is standard practice. An important aspect, next to the wetting of the ink on the substrate, is the interaction of the ink droplets with their neighbors on the substrate. This is especially important, if the ink droplets are of different composition and/or volume. When droplets are printed close to each other, under the influence of wetting on the substrate, they can touch and coalesce. In case of different compositions, internal transport of the ink components can take place over time, either driven by convective, due to merging, or diffusive flows, due to concentration gradients inside the merged droplets. Gaining knowledge of the duration and intensity of these flows can be important in the development of specific kinds of printing applications, like for instance in reactive or colour printing.

In the second part of this thesis, i.e. chapter three, the coalescence and internal mixing of droplets is studied both experimentally and numerically. To begin with, the coalescence dynamics of relatively large silicone droplets will be studied experimentally, tracking the formation of the bridge between the droplets over time. Next, the transport of fluorescent dyes in two small coalescing inkjet printed droplets is studied, both experimentally and numerically. The dye transport is followed as it advances across the

coalescence bridge, enabling it to identify the contribution of convective and diffusive flows for both equally and unequally sized droplets.

The third part, chapter four, is a showcase of potential applications which were developed using the µPlasma patterning tool, introduced in chapter two, as well as some applications made by inkjet printing. The examples include concepts of a Lab-on-Chip, a gas sensor and a RFID-tag. The thesis ends with general conclusions and recommendations for future work in chapter five.

# 2 Surface modification of polymer and glass substrates by plasma treatment

In this chapter the surface modification of substrates by plasma treatment is described. First a general introduction on plasma, and in specific atmospheric µPlasma patterning and wetting is given. This is followed by the results of experimental work on the surface modifications by µPlasma patterning. The surface chemistry and wettability of polymers is investigated before and after plasma treatment for a selection of gas compositions. In the last part of this chapter, the selective modification of substrates is investigated for applications in printed electronics. The results of this chapter are published and presented at international conferences [1-5].

## 2.1 Introduction

Plasma has interested mankind for ages. In nature, plasma is perceived among the most impressive phenomena with the sun, lightning and the aurora borealis as stunning examples. Since the invention of W. Siemens in 1857 of the ozone discharge tube, plasmas and in particular dielectric barrier discharge (DBD) plasmas have become widely used in industrial applications [6]. Dielectric barrier discharge is the electric discharge between two electrodes separated by an insulating dielectric layer. Even though ozone generation is still the most used application in industry, in the last decades with improvements in the DBD plasma technology, new applications have emerged. These applications include, among others surface modification, layer deposition, pollution control, lasers and display technology [7-10]. In principle, plasmas are partially ionized gasses roughly consisting of equal amount of positively and negatively charged particles. Two main categories can be distinguished in plasmas. Hot near-equilibrium plasmas are characterized by very high temperatures, e.g. several thousands of Kelvins, of electrons and heavy particles, mostly ions, and are almost fully ionized. Examples of thermal plasmas are plasma torches or arc plasmas. Cold non-equilibrium plasmas are characterized with relatively high electron

temperatures, but the heavy species are often near room temperature and have a lower degree of ionisation [11, 12]. With the improvements in operating DBD plasmas at atmospheric pressure in a controlled manner, it is possible to treat materials which cannot sustain heat or vacuum, like biological materials or bulky rolls of plastic sheets [13].

A typical dielectric barrier discharge plasma setup consists of two discharge electrodes with one or more insulating layers placed in between.

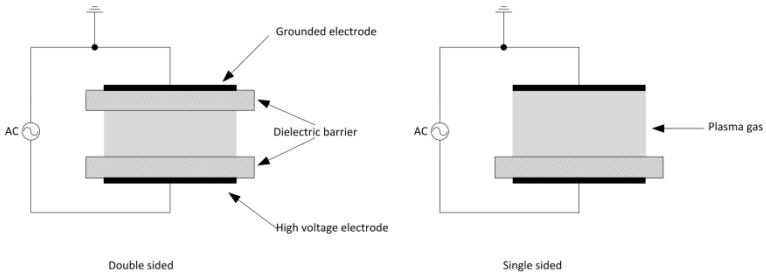


**Figure 2.1: Electrode arrangements for dielectric barrier discharge.**

Besides planar configurations as shown in Figure 2.1, also annular shaped configurations are widely used. The discharge gap between the electrodes and dielectrics can range from 0.1 mm to several centimetres. Due to the capacitive nature of the dielectric layer(s), DBD plasmas can only be driven by AC voltages. To initiate a discharge, an electrical field of several kV needs to be applied. Electrons and ions, present in the gas are accelerated and collide with neutral atoms and molecules. On collision, energy is transferred from one species to the other resulting in ionisation and or excitation of the species. In the case of ionisation, new charged particles are created thus sustaining the plasma. In the case of excitation, energy is released as light or can be used for chemical reactions with species in the plasma or in the surrounding area like the dielectric material. As an electron moves through the gas from one electrode to the other, the number of atoms or molecules it encounters is an important parameter in creating and sustaining the plasma. If too little atoms or molecules are met by an electron during the passage, the plasma dies out. If too many atoms or molecules are present, the electron loses too much energy in the collisions and the plasma will not ignite. In 1889, Paschen experimentally described this relationship between pressure and gap distance and the breakdown voltage needed to create a plasma as shown in Figure 2.2 for different gas compositions [11, 14-16]. When the applied voltage is above the breakdown voltage for a combination of pressure time's distance, the plasma ignites. Dependent on the gas composition and applied voltage and driving frequency, the plasma discharge can either be filamentary or

glow. A filamentary discharge is formed by micro discharges or streamers that develop on the dielectric layer surface. The micro discharges are weakly ionized plasma channels which due to the fast charge build up at the dielectric surface are short lived and normally result in little gas heating. In a micro discharge a large amount of the available energy can be used for exiting atoms or molecules in the gas, starting chemical reactions.

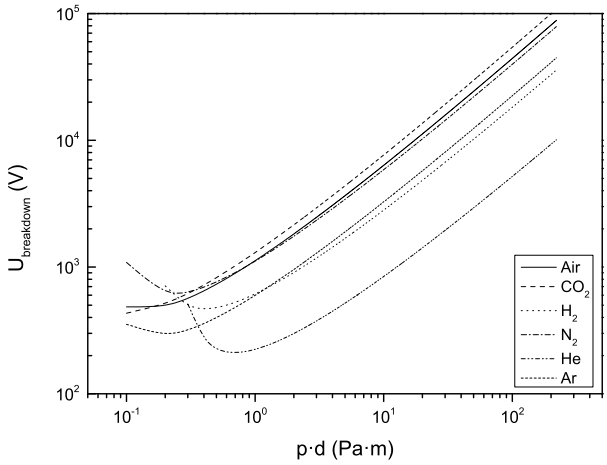


**Figure 2.2: Paschen curve for various gas compositions. Data from [11, 14, 15, 17].**

With increasing driving frequency, the growth and decay of the micro charges cannot follow the rapid changes in electrical field. In this case, under certain conditions, glow discharge can be obtained [9]. The chemically active species contained within the plasma can react with the surrounding environment in different ways according to its application. At this point, we will only focus on surface treatment. Many ways are possible to treat surfaces: cleaning, etching, structural improvement, deposition, activation or functionalization as visualized in Figure 2.3 for polymer materials.

- *Surface cleaning: S*urface cleaning is about removing organic contaminants like chemical or biological materials, oil or dust from the surface of a material. UV-Ozone treatment is widely used as an effective surface cleaning method to remove a variety of contaminants on a substrate. The cleaning is mainly a result of a photosensitized oxidation of the contaminants, removing them from the substrate. A negative side effect of the cleaning of polymer substrates is the oxidation of the polymer itself, damaging the material [18, 19].

- *Surface etching:* During etching material is removed from the substrate surface. The etching rate depends on plasma composition, substrate nature and working conditions like power, gas flow and operating pressure.

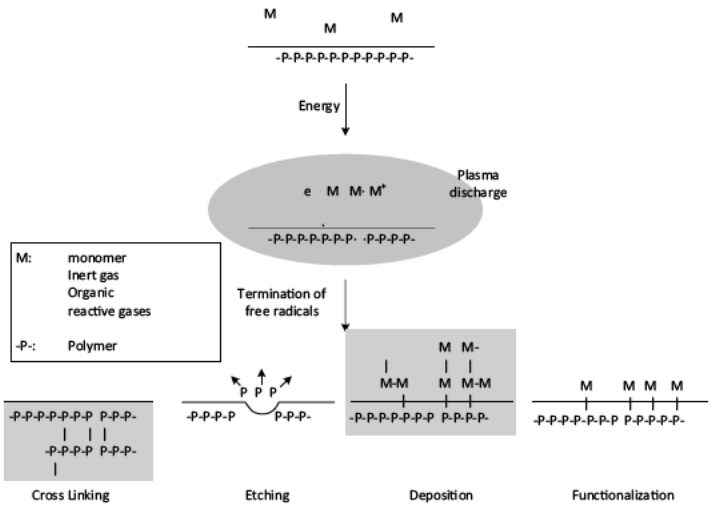


**Figure 2.3: Types of surface modifications by dielectric barrier discharge on polymers.**

- *Surface functionalization:* Surface activation or functionalization is a process that grafts plasma active chemical species on the substrate surface in order to give it special properties. The composition of the plasma gas largely influences the wetting properties of the treated surface. For instance, air plasmas oxidize the surface, making the substrate surface more hydrophilic, whilst plasmas containing silanes or fluor-based species make the substrate surface more hydrophobic. Paragraph 2.1.2 will explain wetting in more detail.
- *Cross-linking:* Radicals generated in plasmas can also lead to improvement of the subsurface structure of polymers by crosslinking polymer chains in the first few molecular layers of the substrate.
- *Surface deposition:* Plasmas are also used to deposit layers of functional materials onto the substrate surface. In most cases a plasma gas, e.g. Argon, is used to bombard a target of a functional material, etching the target material. The released functional material will move through the gas phase towards the substrate forming a layer of deposited material [20-24].

### 2.1.1 µPlasma patterning

Most available atmospheric plasma treatment systems are built to homogenously treat (large) surfaces or generate plasmas with a diameter in the order of a centimetre. µPlasma patterning is a technology recently developed by Innophysics, that combines plasma treatment with digital (inkjet) printing [13, 25]. Instead of printing small inkjet droplets onto a substrate, the plasma is briefly ignited at pre-selected locations to locally treat the surface of the substrate. Without the use of a mask, it is possible to create local differences in surface properties. An example of the local treatment is shown in Figure 2.4. The logo was µPlasma printed onto a pre-silanized hydrophobic glass substrate, locally removing the silane layer forming a hydrophilic area.

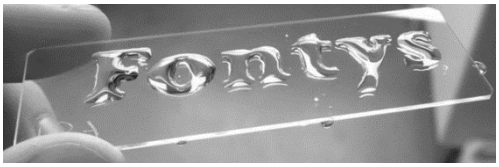


**Figure 2.4: Effect of local µPlasma patterning on silanized glass.**

The µPlasma print head POD24 developed by Innophysics consists of 24 needles, positioned in two rows and is mounted on the modular R&D LP50 inkjet printer from Roth & Rau. In Figure 2.5 the Roth & Rau LP50 printer with the Innophysics POD24 µPlasma print head is shown.

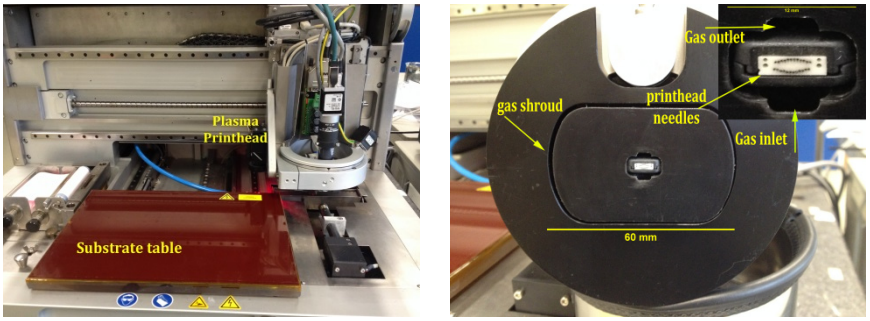


**Figure 2.5: Roth & Rau LP50 printer (left) with Innophysics POD24 print head (right).**

The principle of µPlasma patterning is shown in Figure 2.6. A print head consisting of two rows of twelve needles is positioned above a substrate table. The needles on the print head act as ground electrodes, whilst the substrate table is kept at high voltage to complete the electrical circuit as shown in Figure 2.1. The substrate located on the substrate table acts as the dielectric barrier. The needles in the print head can individually,

move up and down mechanically. Referring to the Paschen curve (Figure 2.2), as the needle moves closer to the substrate table, at a pre-set applied voltage and chosen gas composition, the Paschen curve is crossed and plasma ignites. As the needle moves back and crosses the Paschen curve to the outside, the plasma expires.

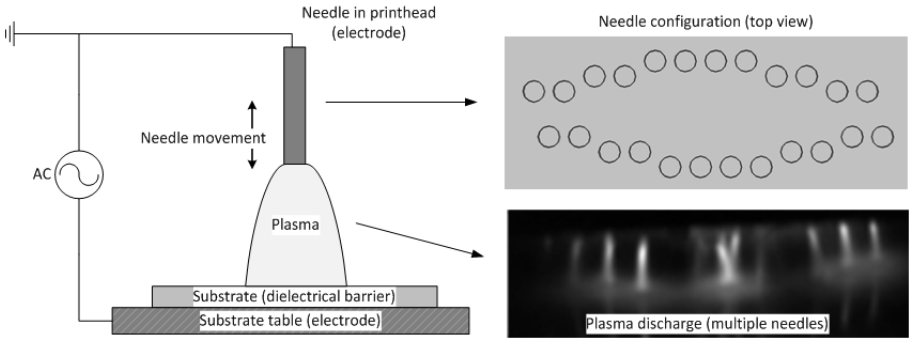


**Figure 2.6: Schematic drawing of µPlasma printer setup. 24 needles are placed in two rows, separated 0.28 mm horizontally and 0.14 mm vertically in a single row. The two rows are separated 0.56 mm at the smallest distance on both ends. This is schematically shown in the top right image. The bottom right image shows an example of micro discharges of the plasma for multiple needles.**

The µPlasma setup works at ambient pressure and temperature in an open system with direct contact to the external environment. In normal operation mode, this means that the plasma will be generated in air at room temperature (22-24$^{o}$C) and with a relative humidity present at that moment in time. The µPlasma setup also accommodates throughput of different gas (mixtures) like dry (compressed) air, nitrogen, argon or precursor materials to influence the reactivity of the plasma gas or to be able to deposit layers on top of the substrate. For this, gas is led through a mass flow controller, and in case of a mixture with a precursor material through a wash bottle with bubbler. Approx. 200 ml/min of gas (mixture) is needed to create a small overpressure of approx. 5 Pa in between the print head and substrate to expel (most) of the air during the µPlasma patterning.

## *2.1.2 Surface energy and wetting behaviour of a substrate*

For plasma treatment and inkjet printing alike, the surface energy of a substrate is an important parameter. Atmospheric dielectric barrier discharge plasma can activate the surface of a substrate by grafting chemically active species onto the surface modifying the surface energy of the substrate. This in turn changes the wetting behaviour of a liquid

deposited by for instance inkjet printing on the plasma treated substrate. The relationship between the surface energy or interfacial tension of a liquid-gas interface ($\sigma_L$), solid-gas interface ($\sigma_S$) and solid-liquid interface ($\gamma_{SL}$) at the 3-phase contact line was formulated in 1805 by Young (Figure 2.7) [26].

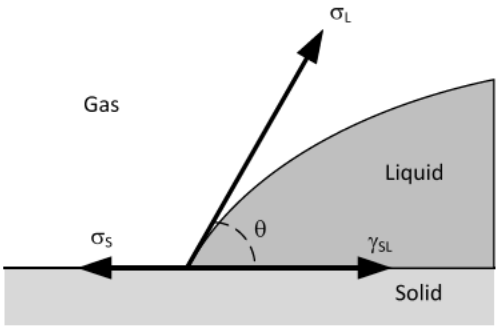


**Figure 2.7: Contact angle on a solid surface according to Young [26, 27].**

$$\sigma_S = \gamma_{SL} + \sigma_L \cdot \cos(\theta) \tag{2.1}$$

According to Young, complete wetting occurs when the interfacial tension of the substrate ($\sigma_S$) is (much) larger than the interfacial tension of the liquid gas interface ($\sigma_L$). In this case, the contact angle ($\theta$) will be equal to zero. No wetting ($90^0 \leq \theta \leq 180^0$) occurs when the opposite is true. In the case of partial wetting ($0^0 \leq \theta \leq 90^0$) the interfacial tensions are comparable in magnitude and the actual contact angle is determined by the interaction between the solid and the liquid interface ($\gamma_{SL}$). Fowkes defined the solid-liquid interfacial tension as the sum of the interfacial tensions of the surface and the liquid and its interactions as shown in equation [28].

$$\gamma_{SL} = \sigma_L + \sigma_s - 2\left(\sqrt{\sigma_S^D \cdot \sigma_L^D} + \sqrt{\sigma_S^P \cdot \sigma_L^P}\right) \tag{2.2}$$

The second part of equation (2.2) is the geometric mean of the dispersive part and polar part of the surface free energies of the solid and liquid respectively. The polar and dispersive parts describe the interaction forces between atoms and molecules like dipole-dipole, ion-dipole, hydrogen bonds on the one hand and van der Waals forces on the other hand [27]. Together the polar ($\sigma^P$) and dispersive part ($\sigma^D$) form the total surface free energy. Building on equation (2.2), Owens, Wendt, Rabel and Kaelble introduced method to calculate the interfacial tension of a solid. This method uses a linear equation,

*y=mx+b* , in which the slope *m* corresponds to the square root of the polar component, and intercept *b* corresponds to the square root of dispersive component and of the substrate surface free energy as shown in equation (2.3) and Figure 2.8a.

$$\frac{\left(1+\cos\left(\theta\right)\right)\sigma_L}{2\sqrt{\sigma_L^D}}=\sqrt{\sigma_S^P}\sqrt{\frac{\sigma_L^P}{\sigma_L^D}}+\sqrt{\sigma_S^D} \tag{2.3}$$

By measuring the contact angle of multiple liquids with known polar and dispersive parts of the interfacial tension and using regression they could determine the interfacial tension of the liquid (Figure 2.8a) can be determined [29-31].

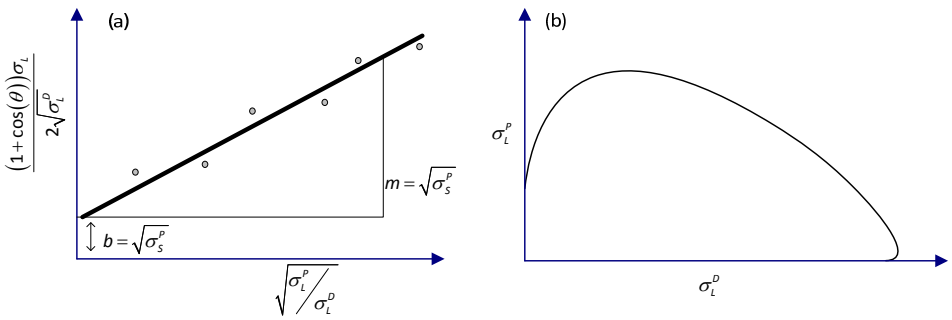


**Figure 2.8: (a) Determination of the polar and dispersive part of the interfacial tension according to the OWRK-method. (b) Predicting the wetting behaviour of a liquid by using the wetting envelope.**

The wetting behaviour of liquids on a substrate can also be predicted from equation (2.3) if the polar and dispersive parts of the solid interfacial tension are known. If the polar and dispersive parts of the interfacial tension of the solid are known, the so-called wetting envelope can be determined (Figure 2.8b).In the wetting envelope, the polar and dispersive parts of the liquids interfacial tension are determined for a contact angle of zero degrees from equation (2.3). Liquids with an interfacial tension that fall within the enclosed area will completely wet. Liquids outside the envelope will partially wet or not wet at all. The OWRK method is commonly used when investigating the effect of polar and dispersive interactions on wettability and adhesion. In particular, the contact between surfaces of different polarity and the effect of change in polarity, for example plasma treatment, can be assessed and optimized with the help of the OWRK method.

## 2.2 Surface characterization of PEN and PC after atmospheric µPlasma and UV ozone treatment

### 2.2.1 Introduction

Organic and printed electronics, like organic LEDs, solar cells, sensors and RFIDs, are an expanding market with a large variety of applications. Advantages of plastic electronic devices are, among others, the relative low cost as a consequence of high throughput and the flexibility in choice of polymer films. Devices can be produced by various printing techniques, such as inkjet printing or screen printing, using liquid functional inks [32-34]. A major challenge in the production of organic printed electronics is to control the wettability and adhesion of the functional inks on the substrate, especially on a polymer substrate. It is well known that polymers have a low surface energy in the range of 20 – 40 mN/m. As most functional inks for printed electronics are either solvent or water based with typical surface tensions in the range of 30-70 mN/m, the wetting of these inks on polymer films is often poor [35]. An indication of the wetting properties of a substrate for a particular ink can be obtained by the use of the wetting envelope. A common method used to increase the polar part of the surface energy, and therefore enlarging the wetting envelope of a substrate, is atmospheric dielectric barrier discharge plasma. Atmospheric dielectric barrier discharge plasma, with air as plasma gas, is known to make polar groups on the surface of the substrate. This enlarges both the total surface energy and the wetting envelope of the substrate, significantly improving the wetting behaviour. Various studies have shown that oxygen incorporation in the surface occurs due to plasma treatment [21, 36-42].

In this investigation, we will compare the surface modification of Polycarbonate (PC) and polyethylene naphthalate (PEN) by UV-Ozone and µPlasma patterning. To investigate the relationship between the change in interfacial tension and the change in chemical composition of the substrate for both methods, the composition of the substrate is also analysed by X-Ray Photoelectron Spectroscopy (XPS) and Attenuated Total Reflectance-Fourier Transform Infrared Spectrometry (ATR-FTIR) [43-46].

## 2.2.2 Experimental

### Preparation of the samples

In this study polycarbonate (PC) and polyethylene naphthalate (PEN) (Goodfellow UK, thickness 125 µm) substrates were modified using UV ozone treatment and µPlasma patterning. The UV-Ozone treatments were carried out using a commercial UV-Ozone cleaner (UVOCS T10X10) which generates UV emissions in the 254 and 185 nanometre range to obtain ozone and atomic oxygen. Both PC and PEN were treated within a range of 1 to 60 minutes of UV-Ozone exposure. µPlasma patterning was carried out using a Roth & Rau Pixdro LP50 inkjet printer equipped with an Innophysics POD24 µPlasma head. The plasma was generated at ambient pressure in air using 5 kV peak tot peak and a gap distance between needles and substrate of 300 µm. Rectangles of 30x60 $mm^2$ were treated on PC and PEN substrates. Each rectangle was printed at the print head native DPI (dots per inch) of 181 at a print head movement speed of 50 mm/s. This corresponds to approx. 17 ms of actual plasma exposure with a maximum energy density of 40 $mJ/cm^2$ after a single treatment of the rectangle. Both polymers exposed to a range of 1 to 500 plasma treatments.

### Analysis of the samples

To assess the effect of both types of plasma treatments on PEN and PC, the change in interfacial tensions was measured by comparing the polar and dispersive parts of the treated and untreated PC and PEN substrates using the OWRK-method. To determine the polar and dispersive parts of the solid interfacial tension and wetting envelope of the substrates, contact angle measurements were performed using deionized water and diiodomethane (Sigma-Aldrich, purity 99%) as test liquids. The dispersive and polar part of the liquid interfacial tension for deionized water and diiodomethane were taken from Ström et al. [47]. Ten droplets of 5 µl, alternating deionized water and diiodomethane, were positioned 7 mm apart on the substrate. The contact angle was measured with a Dataphysics OCA30 contact angle measurement device. The contact angle profile was extracted from the images using Young-Laplace fitting. All ten measurements per sample were used to calculate the solid interfacial tension and wetting envelope with an accuracy of ±2 mN/m.

Changes in chemical composition between treated and untreated PEN and PC were measured by ATR-FTIR and XPS. ATR-FTIR measurements were carried out on a Thermo Avator 330 spectrometer equipped with a Golden Gate Single Reflection Diamond ATR.

The angle of incidence on the diamond crystal was 45°. The spectra were collected with a resolution of 4 $cm^{-1}$ and averaged over 32 scans for wavenumbers from 4000 to 600 $cm^{-1}$. To clarify the surface modification by the treatment spectral subtraction was used. The spectrum of an untreated PC or PEN substrate was measured and used as a reference. Morent et. al. [48] showed ATR-FTIR can be used for the detection of surface oxidation caused by plasma treatment even though the penetration depth is relatively deep compared to the modification depth. XPS measurements were performed on a Thermo Scientific K-Alpha KA1066 spectrometer using a monochromatic Al Kα X-ray source (hv =1486.6 eV). Photoelectrons were collected at a take-off angle of 60°. An X-ray spot 400 µm in diameter was used in the analysis. The samples were neutralized using a flood gun to correct for differential or non-uniform charging. All spectra were corrected for sample charging using the C 1s peak in adventitious carbon (binding energy = 284.0 eV) as an internal reference [49]. High-resolution XPS scans were performed for the O 1s and C 1s regions at a threshold energy of 50 eV.

## *2.2.3 Results and discussion*

### *Wetting and surface energy*

In Figure 2.9, the wetting envelopes for both PC and PEN are shown after either UV-Ozone treatment (a,b) or µPlasma patterning (c,d). If the polar and dispersive part of the liquid is known and falls within the wetting envelope, the liquid will wet completely. If not, only partial wetting will take place. As can be seen, the wetting envelope increases rapidly for both methods after only a short treatment. This indicates a large improvement in wetting for a wide range of liquids compared to untreated PC and PEN. For the UV-Ozone treated samples, the wetting envelope maximizes after approx. 10 min. for PC and 5 min. for PEN. For the plasma treatment, the maximum wetting envelope is reached after 2 treatments for PC and 3-4 treatments for PEN.

For a better understanding of the wetting properties, the surface energy of the substrate is measured as a function of the treatment time. This is shown in Figure 2.10 for both UV-Ozone and µPlasma treated PC and PEN. As can be seen, for all experiments an increase in total surface energy was observed. The UV-Ozone treated substrates show an increase from 40±2 mN/m to 68±2 mN/m for PC and 45±2 mN/m to 65±2 mN/m for PEN. The maximum surface energies are reached after approx. 10 min. for PC and 5 min. for PEN.

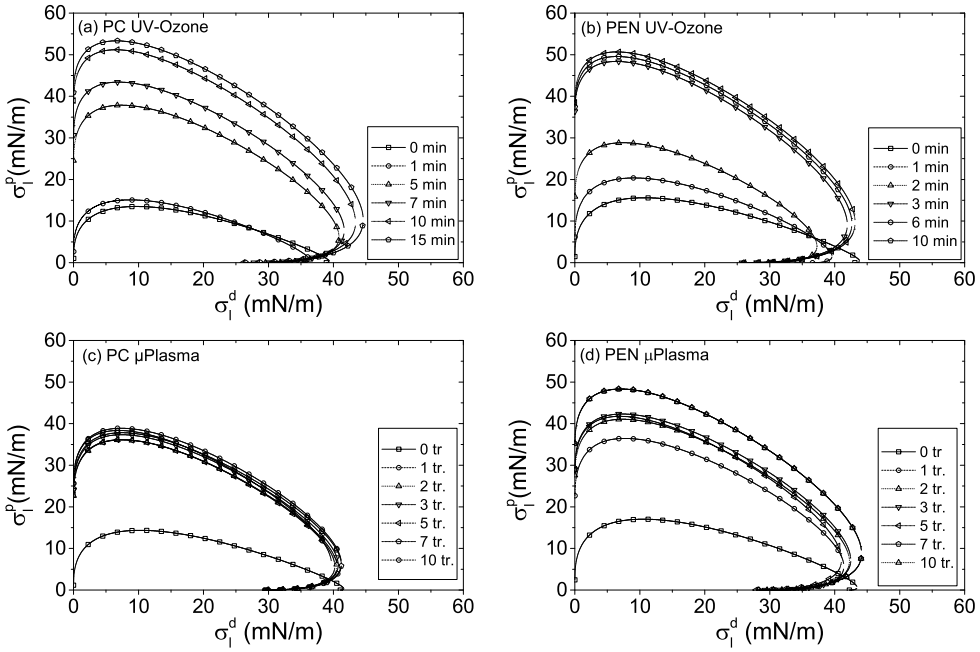


**Figure 2.9: Wetting envelopes for UV-Ozone treated PC (a) and PEN (b) as a function of treatment time and µPlasma treated PC (c) and PEN (d) as a function of number of treatments. The axes show the polar and dispersive parts of the liquid surface energy (markers are added for clarity).**

The increase in total surface energy can be fully attributed to an increase in the polar part of the surface energy, which increases from 0 mN/m to approx. 40±2 mN/m for both PC and PEN. The dispersive part for both polymers decreases by approx. 15±2 mN/m. The µPlasma treated substrates show a similar trend, as for both polymers the total surface energy increases with increasing number of treatments (Figure 2.10c and d). However, this increase is much faster, already reaching its maximum after 2 treatments of approx. 55±2 mN/m for PC and 60±2 mN/m for PEN. This is slightly less compared to the UV-Ozone treatment, resulting in a smaller wetting envelope (Figure 2.9). The increase in total surface energy can also be fully attributed to the increase in the polar part of the surface energy. For PC and PEN, the increases measured in the polar parts of the surface energies equal approx. 25±2 mN/m and 28±2 mN/m, respectively. For both polymers a similar decrease of approx. 15±2 mN/m in the dispersive part of the surface energy is measured. This is comparable to the UV-Ozone treatment.

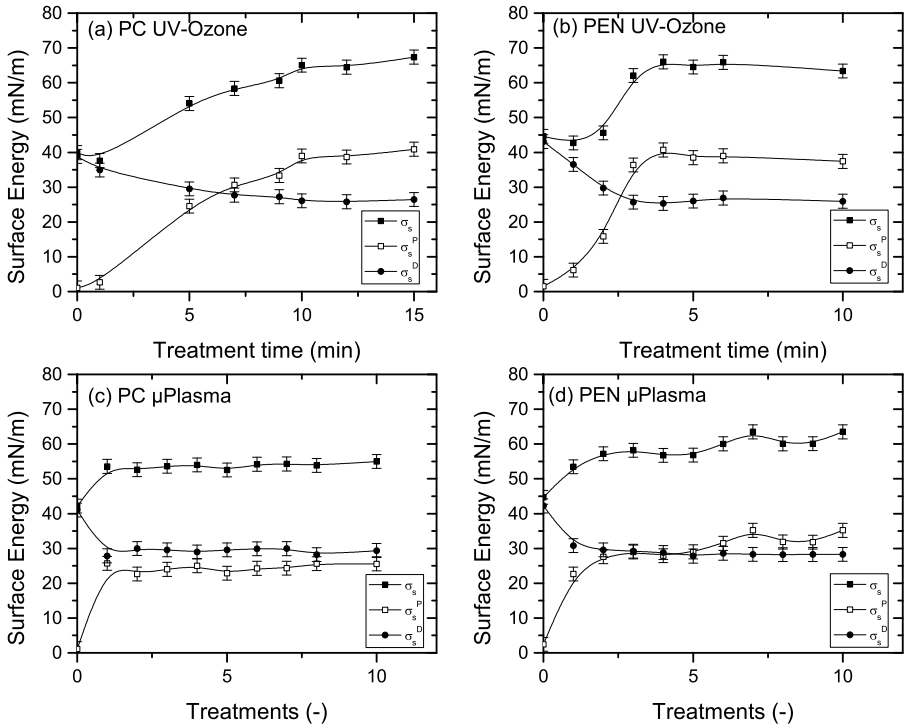


**Figure 2.10: Total, polar and dispersive part of the surface energy ( $\sigma_S, \sigma_S^P, \sigma_S^D$ ) for UV-Ozone treated PC (a) and PEN (b) as a function of treatment time and µPlasma treated PC (c) and PEN (d) as a function of number of treatments.**

Summarized, when comparing UV Ozone and µPlasma treated PC and PEN, a strong increase in the wetting envelope for both methods is found. However, the wetting on both polymers shows to be more susceptible for µPlasma treatment, reaching the maximum wetting envelope much faster. The increase in wetting envelope can be attributed to an increase in the polar part and a smaller decrease of the dispersive part of the surface energy, resulting in an overall larger surface energy.

## *ATR-FTIR analysis*

For atmospheric DBD plasma experiments in air, the increase of the polar surface energy is caused by incorporation of oxygen-containing functionalities into the polymer. These oxygen containing groups provide more interaction between substrate and test fluids, increasing the wetting envelope [50]. To confirm the incorporation of oxygen by UV-Ozone and µPlasma treatment, ATR-FTIR measurements were performed on both untreated and treated PC and PEN films. Although a strong increase in wetting is obtained after short treatment times by either UV-Ozone or µPlasma treatment, the chemical modification of the surface is too small to be determined by ATR-FTIR due to the large penetration depth of infrared light in PC and PEN compared to the modification depth. Therefore, in the case of µPlasma patterning, 500 treatments were performed to obtain a sufficiently intensive modification measurable with ATR-FTIR.

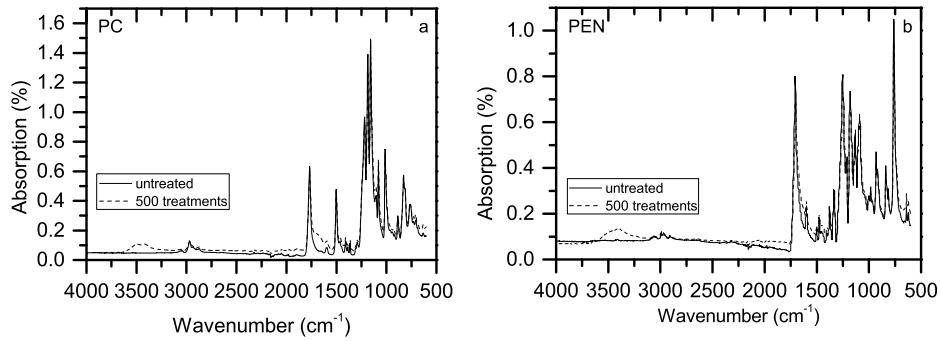


**Figure 2.11: ATR-FTIR spectra as measured for untreated and µPlasma treated PC (a) and PEN (b).**

Figure 2.11 shows the ATR-FTIR spectra for both PC (a) and PEN (b), before and after 500 µPlasma treatments. The spectrum of the untreated polymers can be attributed to specific bonds within the chemical structure of the material. The characteristic bands for the most interesting bonds are listed in Table 2.1 for both PC and PEN. Comparing the ATR-FTIR spectra of the µPlasma treated PC with the untreated PC, the overall intensity of the characteristic bands has decreased. A new broad absorption band appears between 3600 and 3000 $cm^{-1}$. This band can be attributed to –OH stretching vibrations, indicating the appearance of hydroxyl groups on the PC surface. In addition, another band appears at 1675 $cm^{-1}$. This band can be assigned to a C=O stretch vibration. For µPlasma treated PEN a similar effect can be seen in the ATR-FTIR spectra with the appearance of the same

broad absorption band at 3600-3000 $cm^{-1}$, also indicating the appearance of hydroxyl groups on the surface. Similar results were obtained with UV-Ozone treatment.

**Table 2.1: Characteristic ATR-FTIR bands for PC and PEN [43].**

| Substrate | Wavelength ($cm^{-1}$) | Bond vibration |
|---|---|---|
| PC | 2960, 2980 | Symmetric and Asymmetric stretching $CH_3$ |
| | 1774 | C=O stretching from carbonate ester |
| | 1509 | Aromatic C-C in phenyl ring structure |
| | 1165, 1194,1228 | C-O stretch |
| PEN | 2930, 2865 | Symmetric and Asymmetric stretching $CH_2$ |
| | 1710 | C=O stretching from carbonate ester |
| | 1250,1175,1095,1090 | C-O stretching |
| | 755 | $CH_2$ rocking in -C-$(CH_2)_2$-C- |

For further comprehension of the modification caused by the UV-Ozone and µPlasma treatment, spectral subtraction was performed for a series of experiments with different treatment times. The results are presented in Figure 2.12. The subtracted spectra are shown for wavenumbers in the range of 4000 to 2000 $cm^{-1}$ as most interesting region. For all subtracted spectra a baseline correction is performed and they are vertically shifted with increasing intensity of treatment for clarity. For both treatment methods and both polymers an increase in the absorption band between 3600 and 3000 $cm^{-1}$ is visible with increasing intensity of the treatments. As mentioned above, this absorption band shows the existence of hydroxyl groups on the surface of the substrate. As no hydroxyl groups previously existed before treatment, these groups have to be formed due to the UV-Ozone and µPlasma treatment. The µPlasma treatments also seems to form more hydroxyl groups on the substrate compared to UV-Ozone, as the intensity of the hydroxyl-band shows a stronger response with increasing number of treatments. This indicates a more specific chemical modification on the surface for the µPlasma treatment compared to the UV-Ozone treatment. This is interesting, as a single µPlasma treatment on a single spot last approx. 17 ms. With 500 treatments, this equals to roughly 9 seconds of treatment time compared to the 60 minutes for UV-Ozone.

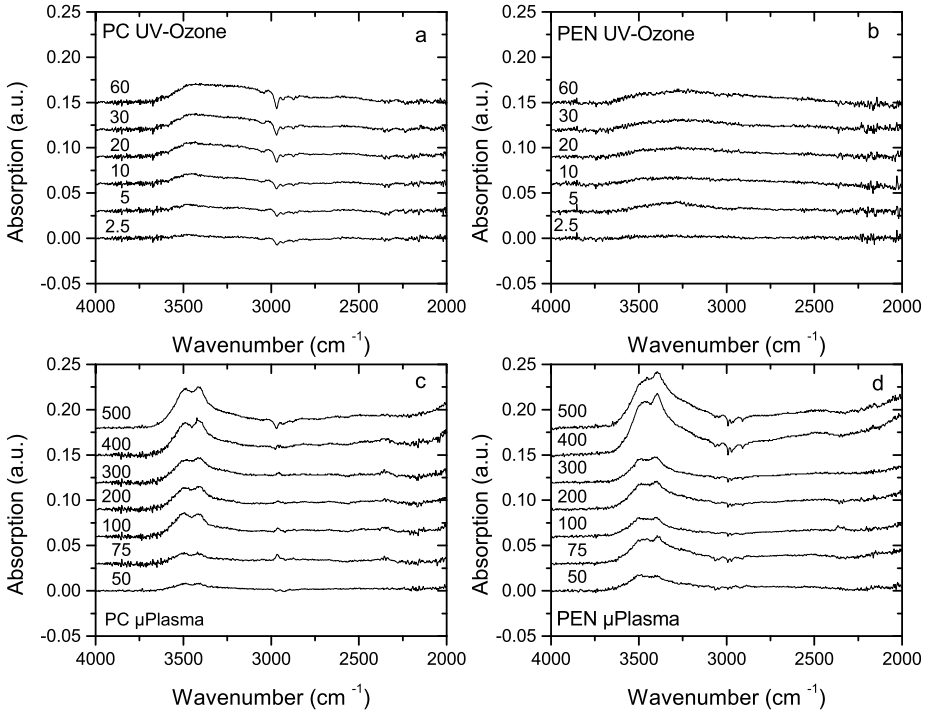


**Figure 2.12: Subtracted ATR-FTIR spectra of UV-Ozone treated PC (a) and PEN (b) and µPlasma treated PC (c) and PEN (d). The spectra are shifted for clarity, the intensity of the treatment increases in vertical direction. For (a) and (b) the intensity is shown in minutes of UV-Ozone treatment, for (c) and (d) in number of µPlasma treatments.**

## *XPS analysis*

To complement the surface energy and ATR-FTIR analyses, XPS-analyses were performed on the PC and PEN substrates. For both substrates and treatment methods, three different treatment intensities were used. First, an untreated substrate was measured as a reference. Second, a treated substrate, just saturated in surface energy was measured to determine the chemical composition of the samples used for the surface energy measurements. Third, substrates with intensive treatment, i.e. 30 min UV-Ozone or 500 µPlasma treatments, were analysed to compare with the ATR-FTIR results.

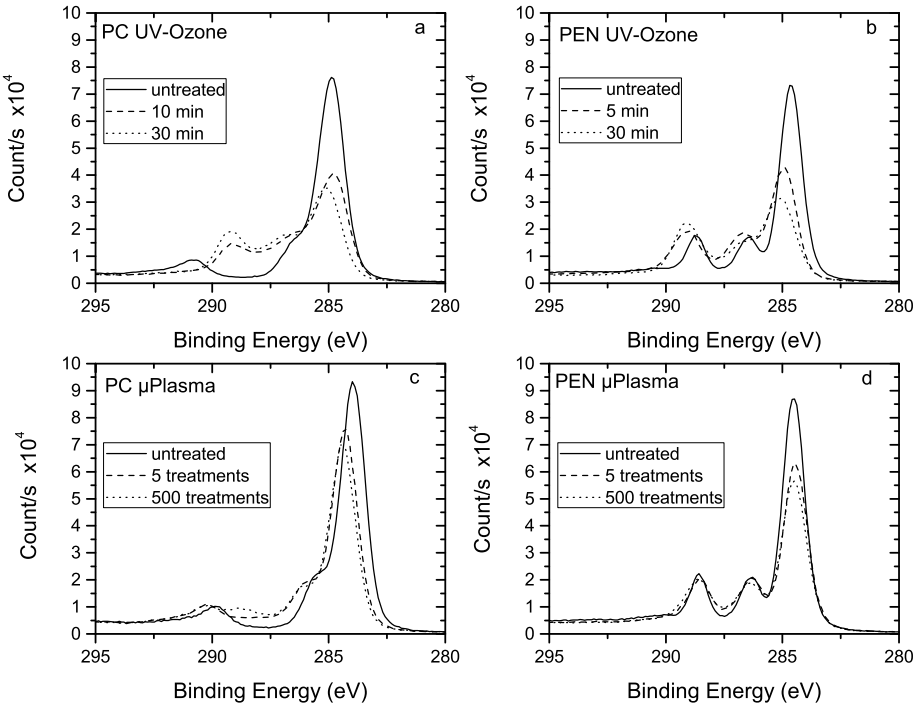


**Figure 2.13: Carbon 1s High resolution XPS spectra for UV-Ozone treated PC (a) and PEN (b) and µPlasma treated PC (c) and PEN (d).**

Figure 2.13 shows the high resolution Carbon 1s XPS spectra for both PC an PEN and both UV-Ozone and µPlasma treatment. For both methods and both polymers an increase in effect of the treatment can be seen in the XPS spectra. Untreated PC displays a peak at 285.0 eV for C-C aromatic and C-C aliphatic, 286.3 eV for C-O groups and 290.6 eV for O-(C=O)-C groups [49, 51]. After UV-Ozone treatment a peak appears at 289.3 eV for C=O groups and the peak at 286.3 (C-O groups) becomes more distinct. Also, a strong decrease of the peak at 285.0 eV is visible, indicating a decrease in aromatic C-C bonds. For the µPlasma treatment a decrease in aromatic C-C bonds at 285.0 eV is also visible, but the decrease is less strong. Also a peak at 298.3. eV appears for C=O groups. The Carbon 1s XPS spectrum for untreated PEN shows three peaks at the binding energies of 285.0, 286.5 and 289.8 eV, corresponding to C-C aromatic, C-O-C and O-C=O groups, respectively. A decrease in the C-C aromatic peak can be seen in both the spectra for UV-Ozone and µPlasma treatment, although the decrease for the µPlasma treatment is much less. For the UV-Ozone treatment a slight increase at 289.8 eV (O-C=O groups) is also visible. Table 2.2 shows the XPS O/C ratio for PC and PEN before and after treatment with UV-Ozone

and µPlasma. An increase in O/C ratio is seen for both methods with prolonged exposure, as expected from the other measurements. Less oxygen is incorporated in the substrate for the µPlasma treatment. These results support the findings from the surface energy and ATR-FTIR measurements above, in which an increase in the polar part of the surface energy was found as well as an increase of oxygen containing groups. It also shows that UV-Ozone treatment does more damage to the substrate by degrading the C-C aromatic bonds, replacing these for oxygen containing groups.

**Table 2.2: XPS O/C ratio of PC and PEN for untreated, Surface Energy saturated (i.e. 10 min and 5 min UV Ozone treatment for PC and PEN respectively or 5 µPlasma treatments for both PC and PEN) and intensive treatment (i.e 30 min UV-Ozone or 500 µPlasma treatments).**

| O/C ratio [%] | PC | | PEN | |
|---|---|---|---|---|
| | UV-Ozone | µPlasma | UV-Ozone | µPlasma |
| untreated | 17 | 19 | 27 | 29 |
| SE saturation | 49 | 32 | 51 | 45 |
| intensive treatment | 60 | 39 | 69 | 51 |

## *2.2.4 Conclusion*

In this study we investigated the effects of UV-Ozone and µPlasma treatments on the surface modification of PC and PEN. In particular we focused on the change in wettability due to these treatments and its relationship to the chemical modification of the substrate surface. Both UV-Ozone and µPlasma patterning are an effective way to modify the wettability, increasing the wetting envelope of both polymer substrates substantially after a short treatment period. The increase in wetting envelope is primarily caused by the increase of the polar part of the surface energy indicating the formation of polar groups on the surface of the substrate. This was confirmed by the ATR-FTIR and XPS-analysis which show an increase in oxygen containing groups and degradation of the C-C aromatic bonds on the surface of the polymer films. For both polymers, the formation of C=O, C-O-C and O-C=O groups was detected as a result of the UV-Ozone and µPlasma treatment. The ATR-FTIR and XPS-analysis also show that this chemical modification continues with on-going treatment even as the wetting envelope reaches a maximum and no further improvement in wetting was seen. This means, that the wetting effect is a surface effect, and that deeper layers do no contribute. Comparing the UV-Ozone treatment with the µPlasma treatment, a difference in intensity was seen. The wettability of both polymers can be more easily controlled using UV-Ozone treatment as after two µPlasma treatments the maximum wetting envelope is already reached whilst for the UV-Ozone treatment this

occurs more gradually. The chemical modification of the substrate surface also shows differences for both treatment methods. For the samples with saturated surface energy and intensively treated samples, the increase in O/C ratio after UV-Ozone treatment is larger than after µPlasma treatment. This was visible in the larger decrease in C-C aromatic bonds for the UV-Ozone treatment. Also, a difference in the formed oxygen containing groups was found. Whereas the formation of C=O, C-O-C and O-C=O groups is seen for both treatment methods, the formation of those groups is more intense after UV-Ozone treatment, while hydroxyl groups are more present after µPlasma patterning. This indicates that UV-Ozone does more damage to the substrate surface compared to µPlasma patterning. This is probably due to the differences in the chemistry and reactivity of the plasma-generated species and UV-Ozone-generated species. Overall, it can be concluded that µPlasma patterning results in a more chemically selective modification as compared to UV-Ozone. In the case that chemical selectivity and treatment duration time are considered important, µPlasma patterning is favourable over UV Ozone.

## 2.3 Surface characterization of atmospheric µPlasma printed HMDSO films on polycarbonate

### 2.3.1 Introduction

Organic thin films are widely used in applications for their mechanical, chemical, optical and electrical properties. Example applications include sensors, optics and microelectronic devices [52, 53]. One method of producing these organic thin films is plasma polymerization. In plasma polymerization, polymers are deposited from a plasma discharge containing polymer vapours in the plasma carrier gas. In the plasma, the plasma species from the carrier gas and polymer molecules react with each other and with the surface of the substrate [54]. Hexamethyl-disiloxane (HMDSO) has been extensively used as monomer material for plasma polymerization. Numerous authors found that substrates plasma treated with HMDSO, showed the formation of highly cross-linked layers of polymerized HMDSO on the surface [20, 54-57]. (P)HMDSO films create a hard inorganic surface structure due to the Si-O-Si bond, toughening and making it more resistant to chemical and mechanical abrasion. Also by lowering the surface energy the material becomes more hydrophobic. In this study, HMDSO and nitrogen as carrier gas are used to deposit (P)HMDSO layers on polycarbonate using atmospheric µPlasma patterning. The resulting layers are examined on changes in wetting behaviour, as well as its chemical composition through ATR-FTIR and XPS analysis.

### 2.3.2 Experimental

#### Deposition of the hexamethyl-disiloxane

Hexamethyl-disiloxane (HMDSO, $C_6H_{18}OSi_2$) was deposited on polycarbonate (PC) (Goodfellow UK, thickness 125 µm) substrates by atmospheric dielectric barrier discharge plasma using a gas mixture of nitrogen and hexamethyl-disiloxane molecules. Nitrogen carrier gas (Praxair, 99.999% purity) was led through a washing bottle filled with hexamethyl-disiloxane precursor (Sigma Aldrich, purity 98.5%) at 40 ml/min to produce a nitrogen saturated HMDSO-mixture at room temperature. To this mixture 160 ml/min of nitrogen was added to produce a continuous 200 ml/min $N_2$-HMDSO gas mixture, which was fed to an Innophysics POD24 µPlasma print head mounted on a Roth & Rau Pixdro LP50 inkjet printer. The $N_2$-HMDSO gas mixture is fed directly in between the µPlasma head and the substrate to create an area with a slightly higher than atmospheric pressure

to expel the air from the plasma treatment area. Rectangles of 30x60 $mm^2$ were printed on polycarbonate substrates. Each rectangle was printed at the print head native DPI (dots per inch) of 181 at a print head movement speed of 50 mm/s. This corresponds to approx. 17 ms of actual plasma exposure with a maximum energy density of 40 $mJ/cm^2$ after a single treatment of the rectangle. The polycarbonate substrates were treated within a range of 1 to 500 plasma treatments.

## *Analysis of the samples*

To assess the effect of the HMDSO deposition on the PC, the change in interfacial tension was measured by comparing the polar and dispersive parts of the treated and untreated PC substrates using the OWRK-method. To determine the polar and dispersive parts of the solid interfacial tension and wetting envelope of the substrates, contact angle measurements were performed using deionized water and diiodomethane (Sigma-Aldrich, purity 99%) as test liquids. The dispersive and polar part of the liquid interfacial tension for deionized water and diiodomethane were taken from Ström et al. [47]. Ten droplets of 5 µl, alternating deionized water and diiodomethane, were positioned 7 mm apart on the substrate. The contact angle was measured with a Dataphysics OCA30 contact angle measurement device. The contact angle profile was extracted from the images using Young-Laplace fitting. All ten measurements per sample were used to calculate the solid interfacial tension and wetting envelope with an accuracy of ±2 mN/m. Changes in chemical composition were measured by ATR-FTIR and XPS. ATR-FTIR measurements were carried out on a Thermo Avator 330 spectrometer equipped with a Golden Gate Single Reflection Diamond ATR. The angle of incidence on the diamond crystal was $45^o$. The spectra were collected with a resolution of 4 $cm^{-1}$ and averaged over 32 scans for wavenumbers from 4000 to 600 $cm^{-1}$. To clarify the surface modification by the treatment spectral subtraction was used. The spectrum of an untreated PC substrate was measured and used as a reference. XPS measurements were performed on a Thermo Scientific K-Alpha KA1066 spectrometer using a monochromatic Al Kα X-ray source (hv =1486.6 eV). Photoelectrons were collected at a take-off angle of 60°. An X-ray spot 400 µm in diameter was used in the analysis. The samples were neutralized using a flood gun to correct for differential or non-uniform charging. All spectra were corrected for sample charging using the C 1s peak in adventitious carbon (binding energy = 284.0 eV) as an internal reference [49]. High-resolution XPS scans were performed for the Si 2p, O 1s and C 1s regions at a threshold energy of 50 eV.

## 2.3.3 Results and discussion

### Wetting and surface energy

The used polycarbonate has a surface energy of approx. 43 mN/m with a large dispersive part (42 mN/m) and a small polar part (1 mN/m). Due to this small polar part, it is expected that water with a high polar part equal to 46.8 mN/m will show poor wetting and a high contact angle. Diiodomethane, being a dispersive liquid with no polar part [47] is expected to have good to moderate wetting. In Figure 2.14, the contact angles of these liquids are shown as a function of µPlasma treatment with the $N_2$/HMDSO gas mixture. As expected, a high contact angle of 85 degrees for water and a moderate contact angle of 33 degrees for diiodomethane are measured for the untreated polycarbonate. Upon treatment, the water contact angle does not significantly change, while for diiodomethane the contact angle increases to 53 degrees after two treatments. No significant change in the contact angles was seen after further increasing the number of treatments. The initial change in contact angle of diiodomethane from 33 to 53 degrees does indicate a change in the surface morphology of the plasma treated substrate. This is confirmed when computing the surface energy and wetting envelope using the method of Owens, Wendt, Rabel and Kaelble as discussed in paragraph 2.1.2 and shown in Figure 2.15.

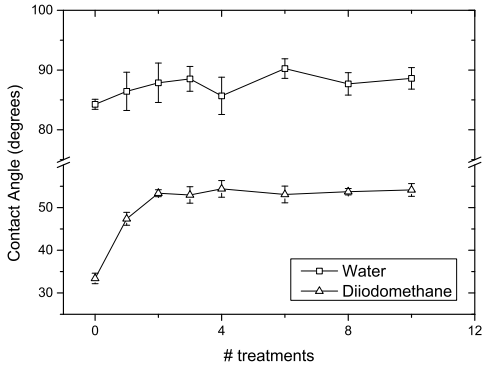


**Figure 2.14: Contact angles of water and diiodomethane after µPlasma treatment with hexamethyl-disiloxane.**

The surface energy of the polycarbonate decreases from 45 mN/m to 31 mN/m after only 2 µPlasma treatments. Further increasing the amount of treatments does not have a significant effect on the surface energy. The decrease in surface energy can be entirely

contributed to the decrease in the dispersive part of the surface energy. The polar part appears not to be influenced by the µPlasma treatment. The wetting envelope of the plasma treated polycarbonate, as shown in Figure 2.15b, becomes smaller with up to two plasma treatments, after which it stabilizes. This means that fewer liquids will perfectly wet on the treated substrates. The wetting envelope decreases most strongly for dispersive liquids, which is in accordance with the contact angle measurement of diiodomethane. Paulussen reports for silicon substrates, treated with HMDSO in atmospheric pressure $N_2$ plasma, a total, dispersive and polar surface energy of 24.2, 23.9 and 0.3 mN/N respectively [58]. Although these values are not reached with the µPlasma printer with 31.3, 29.2 and 2.1 mN/m for the total, dispersive and polar surface energy respectively, the decrease in surface energy can be attributed to the formation of a HMDSO-layer on the surface of the polycarbonate.

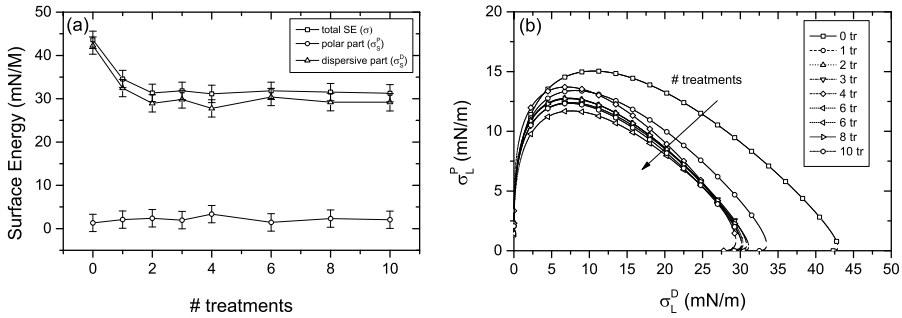


**Figure 2.15: (a) Change in the polar, dispersive and total surface energy after HMDSO/$N_2$ µPlasma treatments. (b) Wettability of the HMDSO/$N_2$-plasma treated polycarbonate.**

## *ATR-FTIR analysis*

To confirm the addition of HMDSO to the surface of the polycarbonate, the chemical composition and structure of the µPlasma treated polycarbonate was investigated with ATR-FTIR. In Table 2.3 the characteristic bond vibrations for both PC and HMDSO-films are shown [43, 54, 58-60].

**Table 2.3: Characteristic bond vibrations for polycarbonate and HDMSO-films [43, 54, 58-60].**

| Material | Wavelength ($cm^{-1}$) | Bond vibration |
|---|---|---|
| Polycarbonate | 2960, 2980 | Symmetric and Asymmetric stretching $CH_3$ |
| | 1774 | C=O stretching from carbonate ester |
| | 1509 | Aromatic C-C in phenyl ring structure |
| | 1165, 1194,1228 | C-O stretch |
| HMDSO | 2970-2940 | C-H stretch |
| | 1260-1235 | Si-CH3 (C-H Bend) |
| | 1080-1010 | Si-O Stretch |
| | 860-800 | Si-C Stretch |

Figure 2.16 shows the ATR-FTIR spectra of both untreated polycarbonate and polycarbonate, µPlasma treated up to 500 times with the $N_2$/HMDSO gas mixture as well as the subtracted ATR-FTIR spectra with PC as reference. Comparing the ATR-FTIR spectra of untreated polycarbonate with the µPlasma treated substrate, the wavelengths at 2970, 1770, 1510, 1230, 1190 and 1165 $cm^{-1}$ become less pronounced with increasing number of treatments. These wavelengths correspond to the characteristic bonds of polycarbonate. The wavelengths at 1090, 1035, 1010, 840 and 800 $cm^{-1}$ become more distinct as the number of plasma treatments increase. These wavelengths correspond with the characteristic vibrations bonds of HMDSO-films. This would indicate a formation of a HMDSO-film on to the surface, concealing the polycarbonate from the ATR-FTIR.

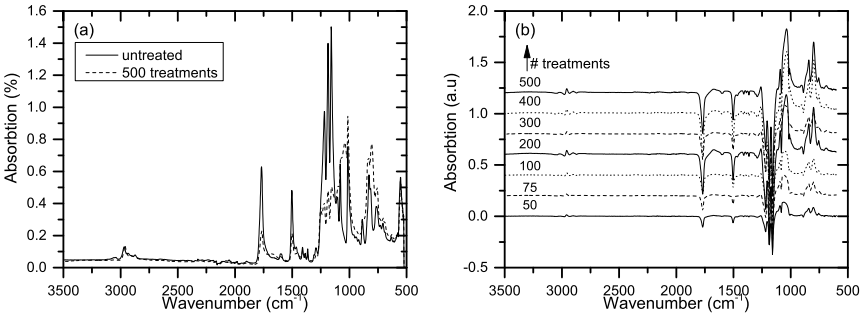


**Figure 2.16: (a) ATR-FTIR spectra as measured for untreated and HMDSO/$N_2$ µPlasma treated polycarbonate. (b) Subtracted ATR-FTIR spectra of HMDSO/$N_2$ treated PC. Untreated PC was used as a reference. The spectra are shifted for clarity, the number of µPlasma treatments increases in vertical direction.**

## *XPS analysis*

To complement the chemical analysis, X-ray photoelectron spectroscopy was performed on the untreated and the $N_2$/HMDSO µPlasma treated polycarbonate substrates. The resulting spectra of the high resolution scans of the carbon 1s and the silicon 2p peaks are shown in Figure 2.17. For untreated polycarbonate, the C1s peak can be deconvoluted into three individual peaks. The carbon peaks present in the untreated polymer are observed at 284.0, 285.6 and 290.0 eV corresponding to aromatic C-C bonds, aliphatic C-C bonds and O-(C=O)-O, respectively [49]. After treatment with the $N_2$/HMDSO µPlasma, the peaks in the carbon 1s spectrum decrease. A slight increase in the C1s spectrum can be seen at 287.4 eV, at increasing number of treatments, which corresponds to the presence of C-Si bonds in the sample [49]. The high resolution silicon 2p spectrum shows no silicon is present at the untreated polycarbonate, as expected. As the HMDSO-film grows with increasing amount of plasma treatments, the Si2p spectrum shows an increasing amount of silicon present. This confirms the presence of a HDMSO-film on the surface of the polycarbonate.

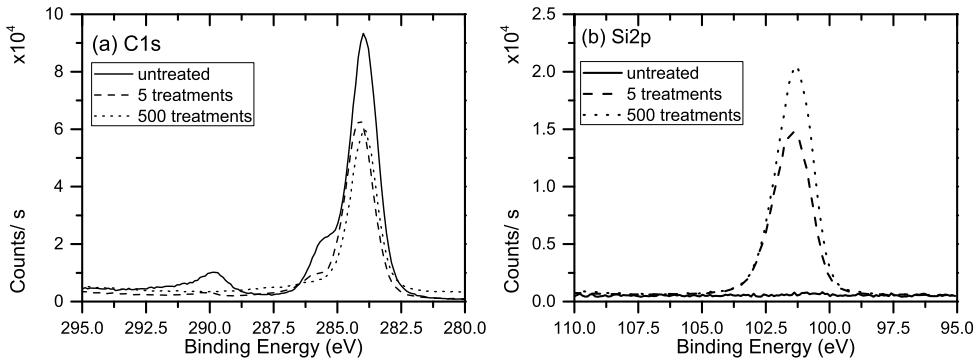


**Figure 2.17: High resolution Carbon 1s XPS (a) and Silicon 2p XPS spectra of PC.**

Table 2.4 shows the atomic carbon, oxygen and silicon percentage of the substrates versus the number of $N_2$/HMDSO plasma treatments. Here, it is clear that the amount of carbon decreases from 84.1% to 51.8% for 500 µPlasma repetitions. Just like ATR-FTIR, XPS has a limited penetration depth into the polycarbonate substrate. As more HMDSO is deposited as film, less characteristic bonds in the polycarbonate excite an electron resulting in a less pronounced peak in both the ATR-FTIR and C1s XPS spectrum. The amount of oxygen in the sample increases with the number of plasma treatments. This is

caused by the Si-O-Si bond in the HMDSO, which was also found by ATR-FTIR. The amount of silicon in the sample increases from 0.2 to 23.2%. The atomic percentage of silicon in HMDSO is approximately 0.07%. When compared with the atomic percentage of Si in the deposited layer, it is observed that this is much lower. Due to the presence of the oxygen radicals in the plasma, the organic components are combusted [61, 62]. This results in the deposition of a Si-rich $SiO_2$ layer.

**Table 2.4: Atomic composition of carbon, oxygen and silicon (in at. %) of the surface as a function of the number of repetitions.**

| XPS peak | untreated | 5 repetitions | 500 repetitions |
|---|---|---|---|
| **C 1s** | 84.1 | 59.5 | 51.8 |
| **O 1s** | 15.7 | 21.7 | 21.5 |
| **Si 2p** | 0.2 | 16.4 | 23.2 |

## *2.3.4 Conclusions*

Polycarbonate substrates were exposed to a nitrogen plasma containing hexamethyl-disiloxane molecules using the µPlasma setup. After multiple plasma treatments, it was found that the water contact angle did not significantly increase. The contact angle of diiodomethane increased from 33 to 53 degrees after just 2 treatments. Additional number of treatments did not increase the contact angle any further. From the wetting envelopes, it can be concluded that polar liquids, like water, will not show any change in wetting behaviour, as the polar part of the surface energy of the treated polycarbonate is hardly influenced upon treatment. Dispersive liquids will show a moderate change in wetting behaviour, especially if their dispersive part is small as well. In total, the wetting envelope becomes smaller upon treatment with the $N_2$/HMDSO gas mixture in the µPlasma setup. Chemical analysis of the µPlasma treated polycarbonate was performed by ATR-FTIR and XPS. Upon increasing number of treatments the peaks of the original polycarbonate ATR-FTIR and XPS spectra became less pronounced, whereas new peaks appeared indicating the presence of silicon on the substrate surface. Overall it can be concluded that silicon dioxide layers were successfully deposited onto the polycarbonate substrates, modifying the wetting behaviour and chemical properties of the substrate surface.

## 2.4 Wettability and aging of polymers after µPlasma patterning

### 2.4.1 Introduction

In the area of printed electronics, polymer materials like polycarbonate (PC), polyimide (PI) and others are used as carrier materials in the production of, among others, organic light emitting diodes, sensor applications and organic solar cells. Via e.g. inkjet printing, screen printing or spin coating, liquids are applied on the polymer to produce functional layers [20, 63-65]. Control of wettability, either uniform or locally is of utmost importance to preserve production levels. In paragraph 2.2, the surface properties of polycarbonate and PEN were changed as a result of atmospheric dielectric barrier discharge treatment by UV-Ozone or µPlasma treatment in air. In both cases, the oxygen content in the surface of the treated polymers as well as the wettability was considerably increased. In time, the wetting properties of a plasma treated polymer surface slowly revert to their original untreated state. This so-called "ageing effect" depends on different parameters like temperature, humidity or polymer type. Hamamatsu et al. found that increasing storage temperature and humidity had an increased ageing effect [66]. It has also been shown that crystalline polymers show a reduced hydrophobic recovery. This is due to the more rigid crystalline polymer structure compared to an amorphous polymer, which has higher chain mobility [67-69]. Various other authors showed changes in wetting behaviour over time due to this ageing effect for polymers treated in dielectric barrier discharge plasmas. De Geyter et al. showed that oxygen containing polar groups introduced by plasma treatment on to the surface of Polyethylene Terephthalate (PET) films improved the wetting properties of such films. After storage in air, the wetting decreased due to reorientation of these polar groups from the surface to the bulk of the material. The ageing effect proceeds slower in air with relative low humidity and low temperature [50, 70, 71]. Similar ageing results were found for polytetrafluoroethylene (PTFE) Borcia et al. [21]. Borcia also found that although the contact angle drastically changes, the amount of bound oxygen is very small in comparison to other polymers investigated, reflecting the high C-F and C-H bond strengths. For nitrogen plasmas on Polypropylene (PP), Polyimide (PI) and PET, it was found that the contact angle rapidly changes in five days after treatment after which it stabilizes to a value roughly halfway between the initially treated and untreated value of the contact angle after one month. An increase in both N/C and O/C ratios was measured indicating the formation of nitrogen

and oxygen containing groups on the polymer surface [42, 72, 73]. The oxygen containing groups are most likely formed due to impurities in the feed gas.

In this investigation the ageing effect in wettability after plasma treatment will be studied on a broad range of polymers used in the printed electronics industry. The polymers will be plasma treated with the µPlasma printer.

## *2.4.2 Experimental*

Polyethylene terephthalate (PET), Polyethylene naphthalate (PEN), Polyimide (PI), Fluorinated ethylene propylene (FEP), and Polycarbonate (PC)-foils were purchased from Goodfellow (UK). All films had a thickness of 125 µm with the exception of FEP, which had a thickness of 100 µm. All films were stored at room temperature (22-24$^{o}$C) and at 30-40% relative humidity for at least 24 hours, before being plasma treated. Just before plasma treatment, the protective film covering the PC-film was removed. The other films were wiped with a clean dry cloth to remove dust particles before treatment. Although no measurements were made, it is expected that the surface of all used films was contaminated with adsorbed water. For the plasma treatment, a Roth & Rau PixDro LP50 inkjet printer, equipped with an Innophysics POD24 µPlasma head, is used (Figure 2.5). For the ageing experiments, an area of 30x60 mm$^2$ of each film was treated with plasma at the following settings. At atmospheric pressure, 200 ml/min nitrogen (99.999% purity, Praxair) was flushed between the needles and the substrate to create a slight overpressure in the open chamber expelling surrounding air. The gap between the needles, in their lowest position, and the top of the polymer film was 300 µm. The peak-to-peak voltage applied was 5.0-5.2 kV with an automatically tuned resonance frequency of approx. 61 kHz. A single plasma treatment is defined as the printing of a bitmap, for example an area of 30x60 mm$^2$, at 181 dots-per-inch (dpi) with a print head movement speed (print speed) of 40 mm/s at the above mentioned voltage and gap settings. Each polymer film was subjected to a single up to twenty identical treatments at the same position of the substrate, increasing the energy delivered to the affected area of the substrate. The energy dissipated in the plasma, per needle per dot, is estimated in the range of 1 to 10 µJ [25, 74]. As this value cannot be measured exactly within the current setup and is dependent on the printing parameters, the maximum value of 10 µJ of dissipated energy per needle per dot will be used to determine the maximum energy density applied to the substrate. For a single treatment with the above-mentioned settings, this corresponds to a maximum energy density on the substrate of 40 mJ/cm$^2$. The plasma treated samples were stored at room temperature (22-24$^{o}$C) with a relative humidity of 30-40% for up to 30 days, after which the surface energy was determined using a Data Physics OCA30

contact angle measuring instrument. Three 5 µl droplets of diiodomethane (Sigma Aldrich) and deionized water were placed within the plasma treated area, at least 5 mm from the edge of the treated area. The contact angle was measured and the total, polar and dispersive parts of the surface energy of the substrate were determined by the Owens-Wendt-Rabel-Kaelbe (OWRK) method (see also paragraph 2.1.2) [29]. In Table 2.5 the polar and dispersive parts of diiodomethane and deionized water, used in the calculations are shown.

**Table 2.5: Total, dispersive and polar part of the surface energy (σ) of the test liquids[47].**

| **Liquids** | $\sigma_L$ **[mN/m]** | $\sigma_L^D$ **[mN/m]** | $\sigma_L^P$ **[mN/m]** |
|---|---|---|---|
| Deionized Water | 72.8 | 26 | 46.8 |
| Diiodomethane | 50.8 | 50.8 | 0 |

## *2.4.3 Results and Discussion*

In order to evaluate the effectiveness of the µPlasma setup to create patterned plasma treated areas, three single pixel wide plasma lines were patterned at a gap distance of 300 µm between the plasma needles on a PC-film at 5.0-5.2 kV with 90 dpi and a table movement speed of 40 mm/s. The lines were separated 5 mm and identically treated twice at the same location. After plasma treatment, the entire PC-film was inkjet printed upon at 110 dpi with diethyleneglycol-dimethacrylate (DEGDMA, Sigma Aldrich) to visualize the change in wetting behaviour between plasma treated and untreated areas. Figure 2.18 shows the result of this experiment. Cleary visible are the plasma treated lines in which the ink shows increased wetting behaviour. The contact angle for DEGDMA changes from 32 degrees in the untreated area to 20 degrees in the plasma treated areas. Using this experimental setup, the size of an individual plasma dot was determined as a function of the gap between the plasma head and substrate, and number of plasma treatments. For a single plasma dot, printed at 5.0-5.2 kV and at a gap of 300 µm, the size of the affected area is approx. 1 mm in diameter. With 20 treatments this increases to 1.6 mm in diameter. The smallest affected area of approx. 300 µm in diameter was found at a gap of 50 µm and 4.2 kV with a single treatment [2, 5]. For consistent evaluation of the ageing effect of the polymers after plasma treatment, first the influence of the number of plasma treatments on the surface energy was investigated. films, until after 4-5 treatments (approx. 200 mJ/cm$^2$), the surface energy reaches a maximum for all films

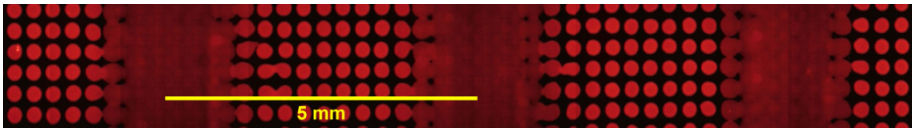


**Figure 2.18: Inkjet printed DEGDMA droplets on plasma treated PC-film ($N_2$, 200 ml/min) with increased wetting at the treated areas (coalesced droplets) compared to the untreated areas (individual droplets). Three single pixel wide lines at intervals of 5 mm were identically plasma printed on the same location twice at intervals of 5 mm and are approx. 1.6 mm wide [2, 5].**

As shown in Figure 2.19, the surface energy increases as a function of number of plasma treatments for the different. This saturation is probably dependent on surface properties like affected sites, roughness and molecular structure of the polymer [24, 70, 71, 75]. Therefore, for consistent evaluation of the ageing effect in the following experiments, all samples were treated 5 times to achieve the maximum change in surface energy. The results of the ageing experiments on the surface energy are shown in Figure 2.20 and Figure 2.21. Figure 2.20 shows the change in water contact angle (WCA) as a function of storage time. For all polymers the WCA decreases directly after treatment. In the following 5 days, the WCA for PEN, PET, PC and PI increases by 10 to 15 degrees and stabilizes after approx. 10 to 15 days. A similar change is seen in Figure 2.21, which shows the change in surface energy for the treated polymers. Directly after treatment PEN, PET, PC and PI show a strong increase in surface energy of approx. 11-24 mN/m compared to the untreated films.

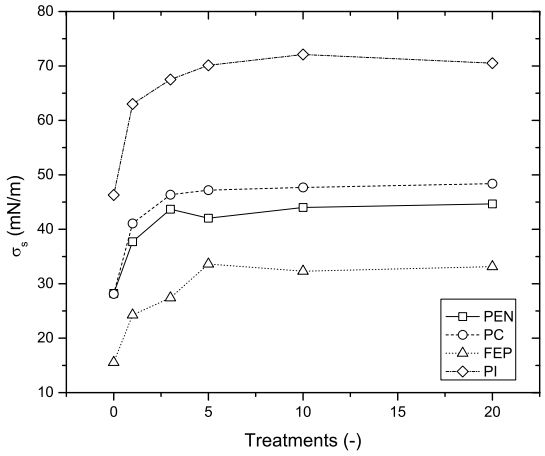


**Figure 2.19: Change in Surface Energy as a function of number of treatments. A single treatment corresponds to an estimated maximum energy density of 40 mJ/cm$^2$.**

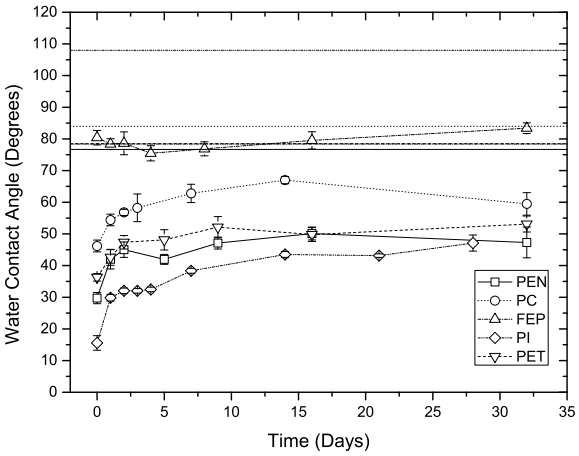


**Figure 2.20 Change in water contact angle (WCA) as function of the storage time. The lines without marker show the WCA of the untreated polymer film.**

This is followed by a strong decrease in the following 5 days until the surface energy stabilizes after approx. 10-15 days. After one month, the WCA, on average, is still 27 degrees smaller compared to the untreated PEN, PET, PC and PI. The surface energy, on average, remains 9 mN/m higher compared to the untreated films. Thus showing a long-lasting improved wetting behaviour after plasma treatment. Figure 2.22 shows the polar and dispersive parts of the surface energy, respectively.

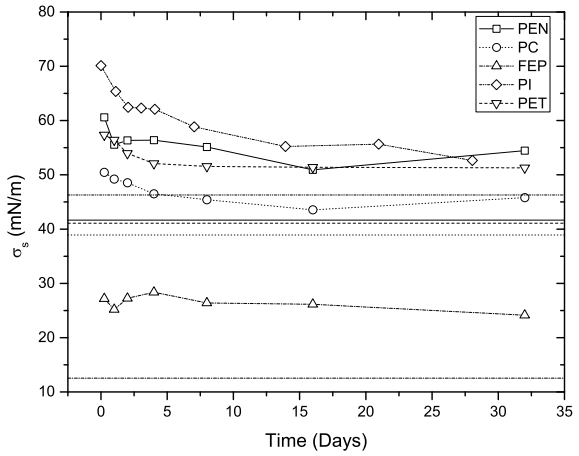


**Figure 2.21: Change in total surface energy as function of storage time. The lines without marker show the surface energy of the untreated polymer film.**

Directly after treatment the polar part of the surface energy increases sharply while the dispersive part decreases to a lesser extent. The increase in the polar part is due to changes in the chemical structure of the polymer surface due to the plasma treatment as discussed in paragraph 2.2. The formation of oxygen containing groups are due adsorbed water on the substrate surface as well as the presence of oxygen and water vapour in the plasma due the open-to-air plasma chamber of the µPlasma setup, even though nitrogen is continually flushed in between the plasma head and substrate.

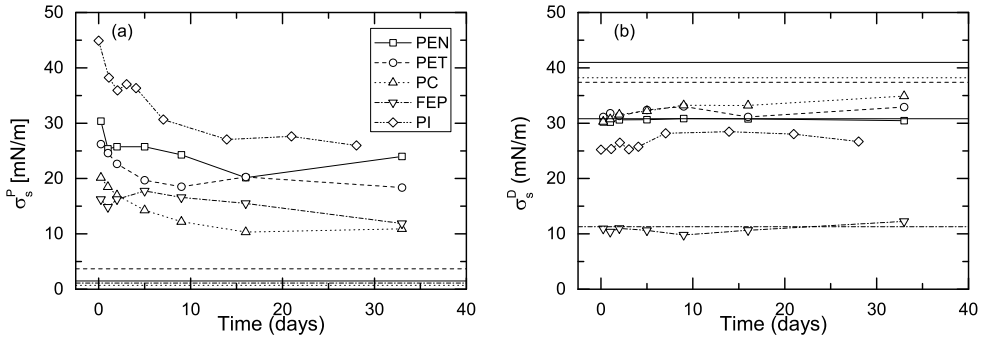


**Figure 2.22: Change in the polar part (a) and dispersive part (b) of the surface energy as a function of ageing time (gap distance 300 µm, print speed 40 mm/s, 181 dpi, $N_2$ – plasma 200 ml/min, 5 treatments). The lines without marker show the surface energy of the untreated polymer film.**

In time, the decrease in the polar part as well as the slight increase in the dispersive part of the surface energy point toward a restructuring of the functional groups on the surface to the bulk of the polymer, as described in literature[42, 70, 72]. XPS experiments on µPlasma printed samples treated with air plasma showed a decrease in O/C ratio with increased storage time[76]. FEP responds differently compared to the other films. Even though an initial decrease of 30 degrees in WCA and an increase of 16 mN/m in surface energy is measured directly after treatment, during storage the WCA and surface energy barely change. This is comparable to results found by Borcia with an atmospheric pressure air DBD plasma on PTFE [21].

### *2.4.4 Conclusions*

In this investigation we studied the ageing effect on the wetting behaviour of PEN, PET, PC, FEP and PI polymer films after plasma treatment. The plasma treatment was performed using a localized maskless plasma print technology at ambient pressure. Under the treatment conditions used, we found that the wetting behaviour of all tested polymer films increased substantially after plasma treatment. The results clearly show that the major changes in wettability occur after a small amount of treatments. More treatments have little beneficial effect on the wettability. The changes in surface energy are mainly due to changes in the polar part of the surface energy, indicating chemical changes on the surface of the polymers. With the exception of FEP, during storage of the plasma treated polymers, the wettability partially declines in the first five days after which it stabilizes to approx. 50% of its original change. FEP showed only little recovery after one month of storage. As the storage time between production steps is mostly under 2 days, the localized plasma print technology shows good promise as pre-treatment step in the production for printed electronics.

## 2.5 Selective modification of wetting behaviour of substrates for printed electronics

### 2.5.1 Introduction

In the previous paragraphs, it was shown that plasma treatment has a profound effect on the surface properties of a material. Dielectric barrier discharge with the µPlasma setup with carrier gasses like air and nitrogen showed an incorporation of oxygen into the polymer substrates, increasing the wettability significantly. Adding a precursor like hexamethyl-disiloxane to the carrier gas deposited a silicon layer on top of the surface, decreasing the wettability. The use of plasma treatment in the production of organic electronics as a means to improve the wettability of a substrate is well known [7, 36, 37]. As in most cases, plasma treatment is done over the complete surface; deposited functional materials like e.g. inkjet printed conductive inks will spread further, creating broader lines. This lowers the highest obtainable resolution of the printed pattern, which in some cases is not wanted. By selectively changing the wettability of the substrate, changing it from hydrophilic to hydrophobic and back when needed, inkjet printed line widths could potentially be controlled. Selective control of wettability using plasma or other technologies is very difficult without the use of masking [65]. However, with the recent development of the µPlasma patterning technology, this might be possible. µPlasma printing is able to selectively and maskless treat the surface with an atmospheric plasma using digital patterning technology similar to drop-on-demand inkjet printing [13]. This control of wettability is especially interesting for polymers which are dominantly used as films and foils for packaging, and more recently as carrier for organic electronics [21, 41, 50, 56, 77, 78]. In recent years, inkjet printing has become a rapidly growing technology for depositing functional materials like conductive inks or light emitting polymers on substrates for low cost manufacturing of organic electronics [33, 79-81]. Challenges lie, among others in the printing of high resolution patterns with high aspect ratio of functional materials to obtain the needed functionality, like e.g. conductivity whilst maintaining good wetting and adhesion. By selectively changing the wettability of the substrate, changing it from hydrophilic to hydrophobic and back when needed, inkjet printed line widths could potentially be controlled. In this paragraph we will continue to investigate µPlasma treatment focusing on determining the minimal µPlasma print resolution. First, we will experimentally determine the minimal obtainable single µPlasma pixel track width using atmospheric air plasma creating hydrophobic tracks. Second, using the data from the first experiment we determine the minimal track width for a nitrogen

with hexamethyl-disiloxane (HMDSO) plasma creating hydrophobic tracks. Third, we will combine the hydrophilic and hydrophobic µPlasma treatments to potentially further decrease the track width.

## 2.5.2 Experimental

All experiments were performed using a Roth & Rau LP50 platform. The LP50 is a modular printer, which means that print heads can be easily exchanged from µPlasma patterning to inkjet printing without large changes to the printer setup. For the µPlasma treatment an Innophysics POD24 plasma head was used. The diameter of the needles in the print head equals 200 µm. Inkjet printing was performed using a Dimatix Spectra SE128 print head (Figure 2.23).

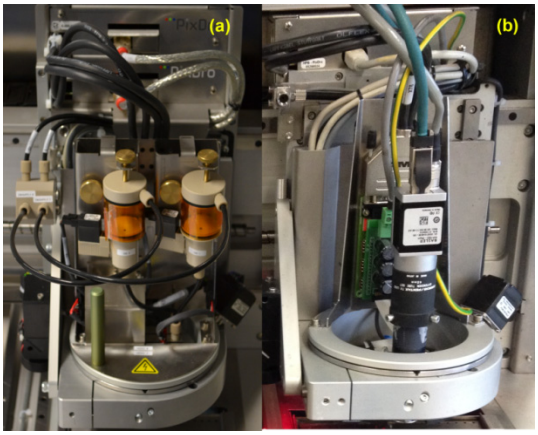


**Figure 2.23: (a) Dimatix Spectra dualhead inkjet print head, (b) Innophysics POD24 plasma print head.**

Three plasma experiments were conducted. The first experiment was to determine the minimal track width of a single pixel wide µPlasma treated line. A bitmap consisting of three, single pixel wide 3 cm long lines, separated 0.5 cm, were plasma treated on either glass (76x22 $mm^2$ glass slides) or polycarbonate (PC) (Goodfellow, thickness 125 µm) substrates. The statistical method of Design of Experiments was used to select the experimental settings using a Central Composite Response Surface Model design with 5 centre points and $\alpha$=1.31. In total two sets of 13 experiments were performed on polycarbonate and glass with different gaps between plasma head and substrate (Table 2.6). In both sets ambient air at atmospheric pressure was used as plasma gas. In the second experiment the plasma was changed to a mixture of saturated HMDSO (Sigma

Aldrich) vapour in $N_2$ (99.999% Praxair) in a ratio of 40:160 ml/min. Squares of 20x20 $mm^2$ were printed for contact angle measurements (Dataphysics OCA30) of deionized water on plasma polymerized HMDSO layers on glass. Also a series of 8 single pixel wide lines with decreasing interspatial distance were plasma printed using the $N_2$/ HMDSO gas mixture (Figure 2.24).

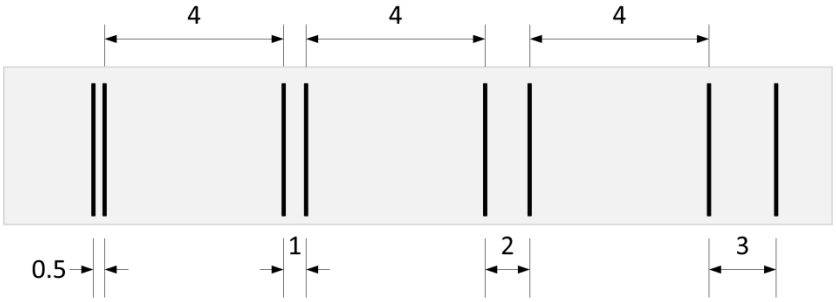


**Figure 2.24: Bitmap used for $N_2$/HMDSO plasma single pixel wide printed lines. Distances between lines in mm.**

In the third experiment, the previous experiments were combined. In this experiment, first a glass slide was air plasma treated 5 successive times in a rectangle of 70x20 $mm^2$, with a 75 µm gap between plasma head and substrate to create a hydrophilic area. Next, the same area was treated with the above mentioned $N_2$/HMDSO gas mixture using the bitmap shown in Figure 2.25. All plasma experiments were performed at 90 dpi.

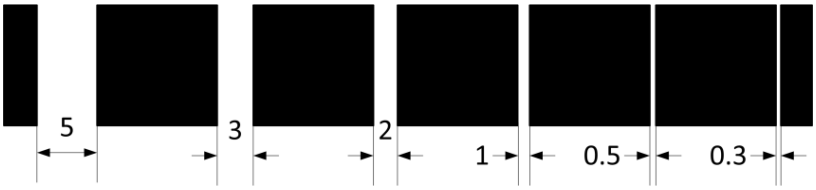


**Figure 2.25: Bitmap used for experiment 3. Distances between treated (black) are shown in mm. The black areas are respectively 5 (first and last) and 10 mm wide and 20 mm high.**

After µPlasma treatment differences in wettability were visualized by inkjet printing 20 pl sized diethyleneglycol-dimethacrylate (DEGDMA, Sigma Aldrich) droplets with 0.01 wt% Coumarin 153 (fluorescent dye, Sigma Aldrich) added to enhance contrast during analysis. The DEGDMA droplets were inkjet printed at 115 or 315 dpi over the complete polycarbonate or glass substrates, respectively. Changes in droplet diameter, as indication of changes in wettability due to µPlasma treatment were measured by fluorescent

microscopy (Olympus BX60) and image analysis software (National Instruments Vision Assistant).

**Table 2.6. Central Composite design (α=1.31, 5 center points, total 13 runs per set).**

| Parameters | | Substrate | Minimum | Maximum |
|---|---|---|---|---|
| 1: | plasma gap | Polycarbonate | 200 µm | 880 µm |
| | nr. of treatments | | 1 | 9 |
| 2: | plasma gap | Glass | 50 µm | 280 µm |
| | nr. of treatments | | 1 | 9 |

## *2.5.3 Results*

Two Central Composite designs (Table 2.6) were performed on polycarbonate and glass substrates to determine the relationship between the plasma gap and number of treatments and the width of a single pixel wide µPlasma printed line. The glass substrates were used, as differences in wetting of DEGDMA due to the plasma treatment on glass were larger, as compared to polycarbonate. In addition, for the glass substrates the minimum gap between plasma head and substrate was lowered to 50 µm. A selection of microscope fluorescent images of the 13 runs on polycarbonate and glass are shown in Figure 2.26 and , respectively. The dots on the images are the inkjet printed DEGDMA droplets. Changes in droplet diameter indicate changes in wetting behaviour due to µPlasma printed single pixel wide line. The corresponding track widths extracted from the images are shown in Table 2.7.

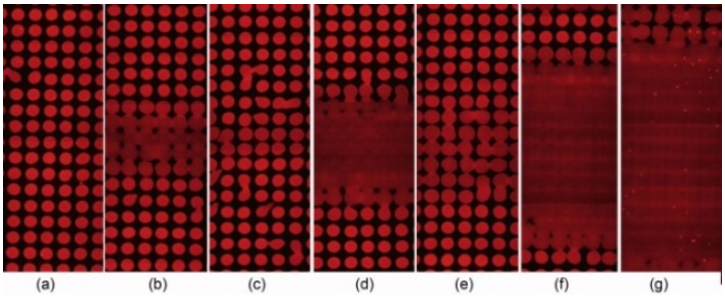


**Figure 2.26. A selection of fluorescent microscopic images of CC-design set 1 on polycarbonate. Inkjet droplets are printed at 115 dpi.**

As can be seen, both plasma gap and number of treatments have a profound influence on the resulting line width of a single pixel wide µPlasma printed line. Although the µPlasma was always carried out as a single pixel wide line, the affected area on the substrate increases with increasing gap and number of treatments. The latter effect, the

number of treatments, was reported earlier by the same authors for larger treated surfaces [82].

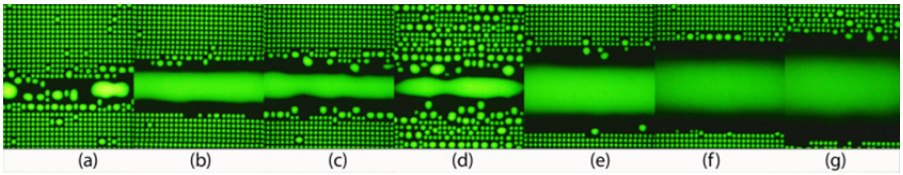


**Figure 2.27. A selection of fluorescent microscopic images of CC-design set 2 on glass. Inkjet droplets are printed at 300 dpi.**

The collected track widths of both 13 runs were collected and analysed as a Central Composite response surface model (RSM) using Design Expert (Stat Ease). For the RSM-design on polycarbonate, the following model equation for the track width (*W*) was found:

$$W_{PC} = -2.72 + 1.22 \cdot 10^{-2} \cdot PH + 0.43 \cdot T - 7.4 \cdot 10^{-6} \cdot PH^2 - 0.026 \cdot T^2 \quad (2.4)$$

For the RSM-design on glass, the following model equation for the track width was found:

$$W_{glass} = -0.074 + 2.85 \cdot 10^{-3} \cdot PH + 0.186 \cdot T - 0.011 \cdot T^2 \quad (2.5)$$

Both models were significant for the gap (*PH*) and number of treatments (*T; $T^2$*), with p-values<0.05 and a p-value for the lack of fit >0.05. The squared gap ($PH^2$) was significant for the polycarbonate experiment, but not for the glass experiment. The adjusted R-square values of the RSM-models for polycarbonate and glass were *0.96* and *0.93,* respectively. Contour plots of the two models are shown in Figure 2.28. The minimum track width of 650 µm, was found for 2 plasma treatments at a gap of 280 µm between plasma head and polycarbonate substrate. On glass, a minimum track width of 320 µm was found at a gap of 50 µm after one plasma treatment. No changes in wetting were visible on polycarbonate after a single treatment at the lowest gap of 200 µm. Although a slight difference in the two model equations exist, the trend of the two experiments show great similarity. The squared dependence on gap height and number of treatments can probably be ascribed to the shape and behaviour of the plasma cloud. Visual observations of the plasma cloud at higher gap heights with the on-board camera show a conical shape which behaves slightly irregular in time.

**Table 2.7: Width of a single pixel line for selected air plasma treated glass experiments from Figure 2.26 and Figure 2.27.**

| **Figure 2.26** | **a** | **b** | **c** | **d** | **e** | **f** | **g** |
|---|---|---|---|---|---|---|---|
| Gap (µm) | 200 | 200 | 280 | 280 | 540 | 540 | 800 |
| Nr. of treatments | 1 | 5 | 2 | 8 | 1 | 5 | 8 |
| Width (mm) | n/a | 0.92 | 0.65 | 1.53 | 1.63 | 2.7 | 3.2 |
| **Figure 2.27** | **a** | **b** | **c** | **d** | **e** | **f** | **g** |
| Gap (µm) | 50 | 50 | 77 | 163 | 163 | 163 | 250 |
| Nr. of treatments | 1 | 5 | 2 | 1 | 5 | 9 | 8 |
| Width | 0.32 | 0.52 | 0.47 | 0.36 | 0.93 | 1 | 1.16 |

The base of the cloud visually grows for larger gaps. This visual irregularity of the discharge would probably affect the substrate at multiple treatments enlarging the affected area. With the needle diameter of 200 µm for a single needle and a conical shape of the plasma cloud, the 320 µm track width can probably not be lowered much without the risk of potentially damaging the substrate or plasma head by lowering the plasma head even further.

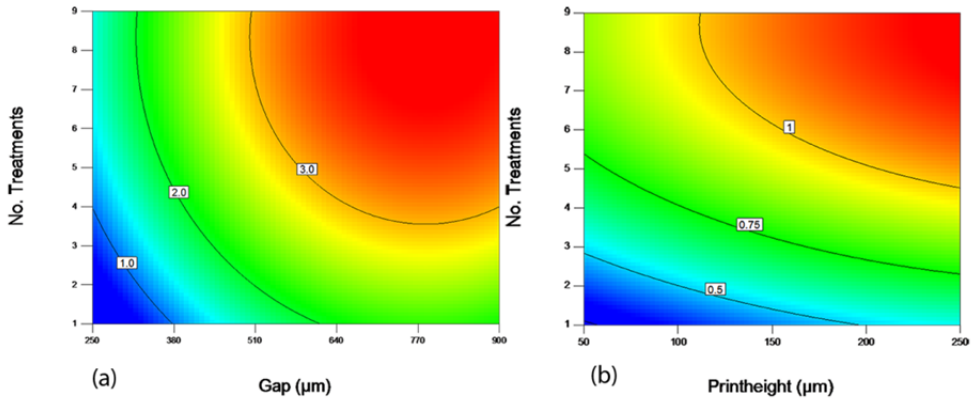


**Figure 2.28. Central Composite design contour plots of a single pixel wide µPlasma printed line on (a) polycarbonate and (b) glass substrates.**

Following the track width experiments with air as plasma gas, the second set of experiments were conducted to investigate the change in local wetting by depositing a series of single pixel wide lines of HMDSO on a glass substrate. For this, a gas mixture of 200 ml/min of $N_2$/HMDSO was fed to the µPlasma apparatus. Squares of 20x20 $mm^2$ were

µPlasma treated on glass at 90 dpi with increasing number of treatments and the contact angles of water and DEGDMA were measured (Figure 2.29). For water, the contact angle clearly increases from <5 degrees for no treatment to 105 degrees for 20 treatments. This is even a larger contact angle compared to the water contact angle measured on HMDSO treated polycarbonate from paragraph 2.3. Although the wetting envelope of the deposited HMDSO layer on glass has not been determined like in paragraph 2.3 for polycarbonate, it is likely it has also decreased in size as indicated by the increase in the water contact angle. This is confirmed with the more dispersive DEGDMA inkjet ink ($\sigma^D$=22.3 mN/m, $\sigma^P$=11.7 mN/m). For DEGDMA the contact angle on glass changes from 43 degrees to 30 degrees after 2 treatments. In comparison, DEGDMA will wet completely on glass after a single µPlasma treatment with air or $N_2$ as carrier gas.

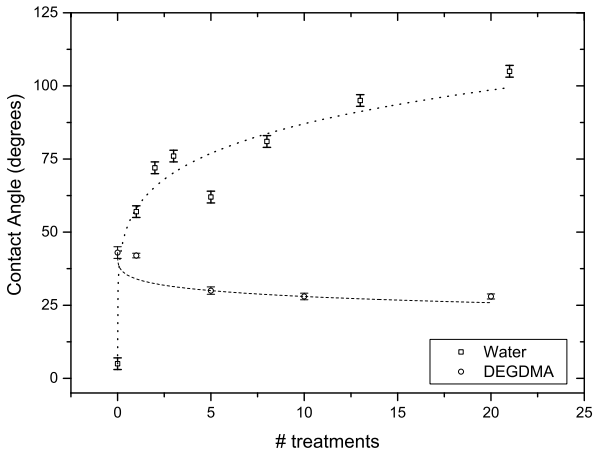


**Figure 2.29: Contact angle of water and DEGDMA on glass treated with $N_2$/HMDSO plasma. Plotted lines are for illustrative purposes only .**

Following the HMDSO printed squares, a bitmap consisting of eight single pixel wide lines (Figure 2.24) was µPlasma treated (two treatments) on glass at decreasing interspatial distance at 90 dpi with the $N_2$/HMDSO gas mixture with a gap of 200 µm. Next, DEGDMA droplets were inkjet printed over the HMDSO treated lines. The change in droplet diameter between untreated and locally µPlasma treated glass was measured (Figure 2.30). As can be seen, droplet diameters change from 125 µm in the untreated areas to approx. 75 µm for the treated areas. Also visible is when the lines approach each other, i.e. on the left of Figure 2.30, the treated areas overlap and no “hydrophilic” untreated area remains. At larger intervals between the lines, the treated areas show less overlap and the wetting of DEGDMA increases, producing larger droplets. The smallest, most

hydrophobic area was found to be approx. 1 mm wide with a transition of approx. 0.5 mm wide on both sides to the hydrophilic areas. Finally, both hydrophilic ($N_2$-plasma) and hydrophobic ($N_2$/HMDSO-plasma) µPlasma treatments were combined to create a large gradient in wettability. First, an area of 70x20 $mm^2$ of the glass slide was treated with $N_2$-plasma to make the surface hydrophilic (DEGDMA contact angle <5 degrees).

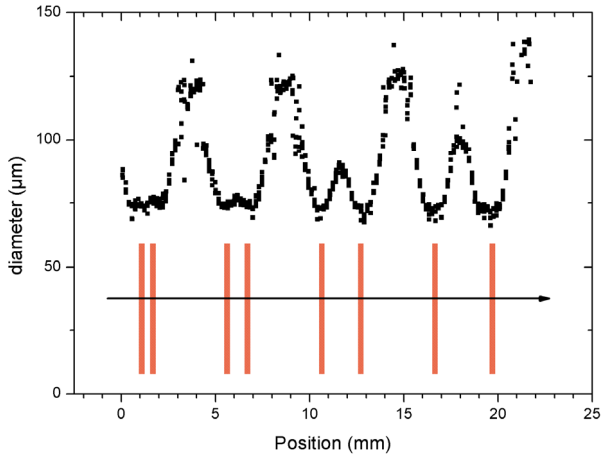


**Figure 2.30: Cross scan of droplet diameters of DEGDMA droplets on HMDSO µPlasma printed lines. (vertical lines show printed HMDSO lines from bitmap).**

Next, areas of decreasing size (Figure 2.25) were µPlasma printed with the $N_2$/HMDSO- gas mixture. In Figure 2.31, the results of the experiment are visualized by inkjet printing DEGDMA droplets.In Figure 2.31 the microscope images of the white areas on the bitmap are shown, for respectively the 5,3,2,1 mm wide white areas of Figure 2.25. The areas showing good wetting, were plasma treated with $N_2$, the surrounding areas were treated with N2/HMDSO-plasma. Clearly visible is the change in wetting behaviour between the good wetting, hydrophilic, areas and the hydrophobic areas at the top and bottom of the images, i.e. the black areas in Figure 2.25.

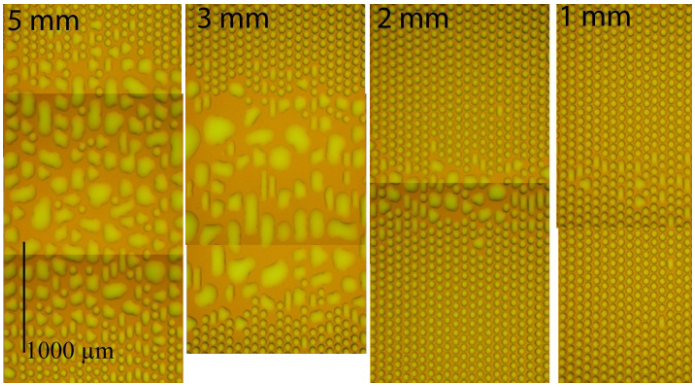


**Figure 2.31. Microscope images of the 5,3,2,1 mm wide "white" areas of the plasma printed Figure 2.25. The areas showing good wetting, were plasma printed with $N_2$, the surrounding areas were treated with $N_2$/HMDSO-plasma.**

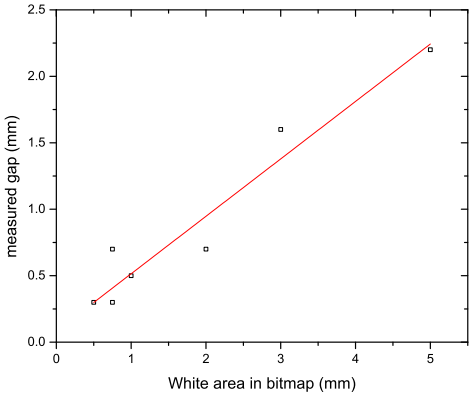


**Figure 2.32. Measured gap in between HMDSO treated areas versus original width of white area from bitmap.**

In Figure 2.32 the length of the hydrophilic gap is shown for the different white areas. The smallest measured gap was equal to 0.3±0.1 mm for the smallest white area of 0.5 mm. With a spot size of approx. 0.4 mm at a gap of 75 µm between the plasma head and substrate, this is as expected.

### *2.5.4 Conclusions*

In conclusion, we showed it is possible to selectively change the wetting behaviour of liquids using different types of plasma. For air and nitrogen plasma, increased wetting of printed materials could be achieved on both polycarbonate and glass substrates. We also showed that using HMDSO as precursor in the plasma gas increases the contact angle for water from less than 10 degrees up to 105 degrees and for DEGDMA from 32 to 46 degrees, making the substrate more hydrophobic. Furthermore, minimal track widths of approx. 300 µm were found for a single pixel wide plasma treated line, independent of the plasma gas used. The option to create small hydrophilic lines by hydrophilic pre-treatment of the substrate followed by hydrophobic HMDSO plasma treatment of the surrounding area showed no further gain in decreasing the minimal track width below 300 µm. With a plasma needle of 200 µm in the Innophysics POD24 plasma head it is believed that no further decrease in track width below 300 µm can be achieved. Further improvements in plasma print resolution should be sought in decreasing the size of the plasma cloud by possibly decreasing the size of the plasma needle.

## 2.6 References


1. Verkuijlen, R., M. van Dongen, A. Stevens, J. van Geldrop, and J. Bernards, *Surface modification of Polycarbonate and Polyethylene Naphtalate Foils by UV-Ozone treatment and µPlasma Printing.* Applied Surface Science, 2013.
2. M.H.A. van Dongen, E. Nieuwenhuis, L. Verbraeken, R. Verkuijlen, P. Ketelaars, and J.P.C. Bernards, *Digital printing of µPlasmas to selectively improve wetting behavior of functional inks for printed electronics*, in *NIP 28 and Digital Fabrication 2012*. 2012, IS&T: Quebec City, Canada. p. 436-439.
3. van Dongen, M., R. Verkuijlen, R. Aben, and J. Bernards, *Wettability and Aging of Polymer Substrates after Atmospheric Dielectrical Barrier Discharge Plasma on Demand Treatment.* Journal of Imaging Science and Technology, 2013. **57**(3): p. 30503-1.
4. Dongen, M.H.A.v., R.O.F. Verkuijlen, and J.P.C. Bernards. *Inkjet Printing of Functional Materials on Selectively Plasma Treated Surfaces*. in *Proc. LOPE-C*. 2011. Frankfurt.
5. van Dongen, M.H.A., E.J. Nieuwenhuis, L. Verbraeken, R.O.F. Verkuijlen, and J.P.C. Bernards, *µPlasma printing of hydrophobic and hydrophilic patterns to improve wetting behaviour for printed electronics.* Proceedings LOPE-C 2012, 2012.
6. Siemens, W., *Ueber die elektrostatische Induction und die Verzögerung des Stroms in Flaschendrähten.* Annalen der Physik, 1857. **178**(9): p. 66-122.
7. Kogelschatz, U. *Fundamentals and applications of dielectric-barrier discharges*. 2000.
8. Kogelschatz, U., *Dielectric-barrier discharges: Their history, discharge physics, and industrial applications.* Plasma chemistry and plasma processing, 2003. **23**(1): p. 1-46.
9. Kogelschatz, U., B. Eliasson, and W. Egli, *From ozone generators to flat television screens: history and future potential of dielectric-barrier discharges.* Pure and Applied Chemistry, 1999. **71**(10): p. 1819-1828.
10. Mark, H.F., *PLASMA PROCESSING OF POLYMERS*, in *Encyclopedia of polymer science and technology*. 2007, John Wiley & Sons, Inc.
11. Lieberman, M.A. and A.J. Lichtenberg, *Principles of plasma discharges and materials processing.* 1994.
12. Wagner, H.E., R. Brandenburg, K.V. Kozlov, A. Sonnenfeld, P. Michel, and J.F. Behnke, *The barrier discharge: basic properties and applications to surface treatment.* Vacuum, 2003. **71**(3): p. 417-436.
13. Brok, W., A. Stevens, E. Bos, T. Huiskamp, N.v. Hijningen, and H.d. Haan, *The potential of plasma printing.* Mikroniek, 2011(1): p. 32-39.
14. Go, D.B. and D.A. Pohlman, *A mathematical model of the modified Paschen's curve for breakdown in microscale gaps.* Journal of Applied Physics, 2010. **107**(10): p. 103303-103303-9.

15. Paschen, F., *Ueber die zum Funkenübergang in Luft, Wasserstoff und Kohlensäure bei verschiedenen Drucken erforderliche Potentialdifferenz.* Annalen der Physik, 1889. **273**(5): p. 69-96.
16. Raizer, Y.P., V.I. Kisin, and J.E. Allen, *Gas discharge physics*. Vol. 1. 1991: Springer-Verlag Berlin.
17. *Plasma physics: Paschen Curve*, in *Laboratory Experiments Physics*, P. systeme, Editor. 2013, PHYWE systeme GMBH: Göttingen.
18. Vig, J.R., *UV/ozone cleaning of surfaces.* Journal of Vacuum Science & Technology A: Vacuum, Surfaces, and Films, 1985. **3**(3): p. 1027-1034.
19. Oláh, A., H. Hillborg, and G.J. Vancso, *Hydrophobic recovery of UV/ozone treated poly (dimethylsiloxane): adhesion studies by contact mechanics and mechanism of surface modification.* Applied surface science, 2005. **239**(3): p. 410-423.
20. Tendero, C., C. Tixier, P. Tristant, J. Desmaison, and P. Leprince, *Atmospheric pressure plasmas: A review.* Spectrochimica Acta Part B: Atomic Spectroscopy, 2006. **61**(1): p. 2-30.
21. Borcia, G., C. Anderson, and N. Brown, *The surface oxidation of selected polymers using an atmospheric pressure air dielectric barrier discharge. Part I.* Applied surface science, 2004. **221**(1): p. 203-214.
22. Zhi, F., Q. Yuchang, W. Hui, and E. Kuffel, *Improving Hydrophobicity of Glass Surface Using Dielectric Barrier Discharge Treatment in Atmospheric Air.* Plasma Science and Technology, 2007. **9**: p. 582.
23. Zhi, F., Q. Yuchang, and W. Hui, *Surface treatment of Polyethylene terephthalate film using atmospheric pressure glow discharge in air.* Plasma Science and Technology, 2006. **6**(6): p. 2576.
24. Desmet, T., R. Morent, N. De Geyter, C. Leys, E. Schacht, and P. Dubruel, *Nonthermal Plasma Technology as a Versatile Strategy for Polymeric Biomaterials Surface Modification: A Review.* Biomacromolecules, 2009. **10**(9): p. 2351-2378.
25. Huiskamp, T., W. Brok, A. Stevens, E. van Heesch, and A. Pemen, *Maskless Patterning by Pulsed-Power Plasma Printing.* Plasma Science, IEEE Transactions on, 2012. **40**(7): p. 1913-1925.
26. Young, T., *An essay on the cohesion of fluids.* Philosophical Transactions of the Royal Society of London, 1805: p. 65-87.
27. De Gennes, P.-G., F. Brochard-Wyart, and D. Quéré, *Capillarity and wetting phenomena: drops, bubbles, pearls, waves*. 2004: Springer.
28. Fowkes, F.M., *Attractive forces at interfaces.* Industrial & Engineering Chemistry, 1964. **56**(12): p. 40-52.
29. Owens, D.K. and R. Wendt, *Estimation of the surface free energy of polymers.* Journal of Applied Polymer Science, 1969. **13**(8): p. 1741-1747.
30. Kaelble, D., *Dispersion-polar surface tension properties of organic solids.* 1970.
31. Rabel, W., *Einige Aspekte der Benetzungstheorie und ihre Anwendung auf die Untersuchung und Veränderung der Oberflächeneigenschaften von Polymeren.* Farbe und Lack, 1971. **77**(10): p. 997-1006.

32. Berggren, M., D. Nilsson, and N.D. Robinson, *Organic materials for printed electronics.* Nature materials, 2007. **6**(1): p. 3-5.
33. de Gans, B.J., P.C. Duineveld, and U.S. Schubert, *Inkjet Printing of Polymers: State of the Art and Future Developments.* Advanced Materials, 2004. **16**(3): p. 203-213.
34. Kelley, T.W., P.F. Baude, C. Gerlach, D.E. Ender, D. Muyres, M.A. Haase, D.E. Vogel, and S.D. Theiss, *Recent progress in organic electronics: Materials, devices, and processes.* Chemistry of materials, 2004. **16**(23): p. 4413-4422.
35. Geoghegan, M. and G. Krausch, *Wetting at polymer surfaces and interfaces.* Progress in polymer science, 2003. **28**(2): p. 261-302.
36. Merilampi, S., T. Laine-Ma, and P. Ruuskanen, *The characterization of electrically conductive silver ink patterns on flexible substrates.* Microelectronics Reliability, 2009. **49**(7): p. 782-790.
37. Kang, B.J., Y.S. Kim, Y.W. Cho, and J.H. Oh, *Effects of plasma surface treatments on inkjet-printed feature sizes and surface characteristics.* Microelectronic Engineering, 2011. **88**(8): p. 2355-2358.
38. Kogelschatz, U. *Fundamentals and applications of dielectric-barrier discharges*. in *HAKONE VII Int. Symp. On High Pressure Low Temperature Plasma Chemistry, Greifswald*. 2000.
39. Strobel, M., M.J. Walzak, J.M. Hill, A. Lin, E. Karbashewski, and C.S. Lyons, *A comparison of gas-phase methods of modifying polymer surfaces.* Journal of adhesion science and technology, 1995. **9**(3): p. 365-383.
40. Grace, J.M. and L.J. Gerenser, *Plasma treatment of polymers.* Journal of dispersion science and technology, 2003. **24**(3-4): p. 305-341.
41. Borcia, G., C. Anderson, and N. Brown, *The surface oxidation of selected polymers using an atmospheric pressure air dielectric barrier discharge. Part II.* Applied surface science, 2004. **225**(1): p. 186-197.
42. Petryakov, A., Y.S. Akishev, A. Balakirev, M. Grushin, and N. Trushkin. *On the Induced Ageing of Hydrophilic and Hydrophobic Properties of Polymer Films Treated by Non-Thermal Plasma*. in *Modification of Materials with Particle Beams and Plasma Flows*. 2010. Tomsk, Russia: Russian Academy of Sciences.
43. Lehocký, M., H. Drnovska, B. Lapčíková, A. Barros-Timmons, T. Trindade, M. Zembala, and L. Lapčík, *Plasma surface modification of polyethylene.* Colloids and Surfaces A: Physicochemical and Engineering Aspects, 2003. **222**(1): p. 125-131.
44. Chan, C.M., T.M. Ko, and H. Hiraoka, *Polymer surface modification by plasmas and photons.* Surface science reports, 1996. **24**(1): p. 1-54.
45. Holländer, A., R. Wilken, and J. Behnisch, *Subsurface chemistry in the plasma treatment of polymers.* Surface and coatings technology, 1999. **116**: p. 788-791.
46. Rochotzki, R., M. Nitschke, M. Arzt, and J. Meichsner, *Plasma modification of polymer films studied by ellipsometry and infrarot spectroscopy.* physica status solidi (a), 1994. **145**(2): p. 289-297.

47. Ström, G., M. Fredriksson, and P. Stenius, *Contact angles, work of adhesion, and interfacial tensions at a dissolving hydrocarbon surface.* Journal of Colloid and Interface Science, 1987. **119**(2): p. 352-361.
48. Morent, R., N. De Geyter, C. Leys, L. Gengembre, and E. Payen, *Comparison between XPS-and FTIR-analysis of plasma-treated polypropylene film surfaces.* Surface and Interface Analysis, 2008. **40**(3-4): p. 597-600.
49. Moulder, J.F., W.F. Stickle, P.E. Sobol, and K.D. Bomben, *Handbook of X-ray Photoelectron Spectroscopy*. 1995: Physical Electronics, Chanhassen, MN.
50. De Geyter, N., R. Morent, C. Leys, L. Gengembre, and E. Payen, *Treatment of polymer films with a dielectric barrier discharge in air, helium and argon at medium pressure.* Surface and Coatings Technology, 2007. **201**(16): p. 7066-7075.
51. Fricke, K., H. Tresp, R. Bussiahn, K. Schröder, K. Weltmann, and T. von Woedtke, *Modification of the physicochemical surface properties of polymers during the plasma-based decontamination.*
52. Mueller, K., C. Schoenweitz, and H.C. Langowski, *Thin Laminate Films for Barrier Packaging Application–Influence of Down Gauging and Substrate Surface Properties on the Permeation Properties.* Packaging Technology and Science, 2011. **25**(3): p. 137-148.
53. Biederman, H., *Plasma polymer films*. 2004: World Scientific.
54. Morent, R., N. De Geyter, S. Van Vlierberghe, P. Dubruel, C. Leys, L. Gengembre, E. Schacht, and E. Payen, *Deposition of HMDSO-based coatings on PET substrates using an atmospheric pressure dielectric barrier discharge.* Progress in Organic Coatings, 2009. **64**(2–3): p. 304-310.
55. Sarmadi, A., T. Ying, and F. Denes, *HMDSO-plasma modification of polypropylene fabrics.* European polymer journal, 1995. **31**(9): p. 847-857.
56. Höcker, H., *Plasma treatment of textile fibers.* Pure and Applied Chemistry, 2002. **74**(3): p. 423-427.
57. Shi, F.F., *Recent advances in polymer thin films prepared by plasma polymerization Synthesis, structural characterization, properties and applications.* Surface and Coatings Technology, 1996. **82**(1–2): p. 1-15.
58. Paulussen, S., O. Goossens, and D. Vangeneugden, *Chemical and physical properties of hydrophobic coatings obtained in a dielectric barrier discharge.*
59. Kasih, T.P., S. Kuroda, and H. Kubota, *A Nonequilibrium, Atmospheric-Pressure Argon Plasma Torch for Deposition of Thin Silicon Dioxide Films.* Chemical Vapor Deposition, 2007. **13**(4): p. 169-175.
60. Morent, R., N. De Geyter, S. Van Vlierberghe, P. Dubruel, C. Leys, and E. Schacht, *Organic–inorganic behaviour of HMDSO films plasma-polymerized at atmospheric pressure.* Surface and coatings technology, 2009. **203**(10): p. 1366-1372.
61. Magni, D., C. Deschenaux, C. Hollenstein, A. Creatore, and P. Fayet, *Oxygen diluted hexamethyldisiloxane plasmas investigated by means of in situ infrared absorption spectroscopy and mass spectrometry.* Journal of Physics D: Applied Physics, 2000. **34**(1): p. 87.

62. Wavhal, D.S., J. Zhang, M.L. Steen, and E.R. Fisher, *Investigation of gas phase species and deposition of SiO2 films from hmdso/O2 plasmas.* Plasma Processes and Polymers, 2006. **3**(3): p. 276-287.
63. Burns, S.E., C. Kuhn, K. Jacobs, J.D. MacKenzie, C. Ramsdale, A.C. Arias, J. Watts, M. Etchells, K. Chalmers, and P. Devine, *Printing of polymer thin-film transistors for active-matrix-display applications.* Journal of the Society for Information Display, 2004. **11**: p. 599.
64. Betton, E.S., W.K. Hsiao, G. D Martin, and I. M Hutchings, *Behavior of Ink Jet Printed Drops on a Corona-Treated Polymeric Film Substrate.* Journal of Imaging Science and Technology, 2011. **55**(5): p. 050606-050606-10.
65. Park, J.B., J.Y. Choi, S.H. Lee, Y.S. Song, and G.Y. Yeom, *Polymer surface texturing for direct inkjet patterning by atmospheric pressure plasma treatment.* Soft Matter, 2012. **8**(18): p. 5020-5026.
66. Nakamatsu, J., L.F. Delgado-Aparicio, R. Da Silva, and F. Soberon, *Ageing of plasma-treated poly(tetrafluoroethylene) surfaces.* Journal of adhesion science and technology, 1999. **13**(7): p. 753-761.
67. Yun, Y.I., K.S. Kim, S.J. Uhm, B.B. Khatua, K. Cho, J.K. Kim, and C.E. Park, *Aging behavior of oxygen plasma-treated polypropylene with different crystallinities.* Journal of adhesion science and technology, 2004. **18**(11): p. 1279-1291.
68. Kim, K.S., C.M. Ryu, C.S. Park, G.S. Sur, and C.E. Park, *Investigation of crystallinity effects on the surface of oxygen plasma treated low density polyethylene using X-ray photoelectron spectroscopy.* Polymer, 2003. **44**(20): p. 6287-6295.
69. Banik, I., K.S. Kim, Y.I. Yun, D.H. Kim, C.M. Ryu, C.S. Park, G.S. Sur, and C.E. Park, *A closer look into the behavior of oxygen plasma-treated high-density polyethylene.* Polymer, 2003. **44**(4): p. 1163-1170.
70. De Geyter, N., R. Morent, and C. Leys, *Influence of ambient conditions on the ageing behaviour of plasma-treated PET surfaces.* Nuclear Instruments and Methods in Physics Research Section B: Beam Interactions with Materials and Atoms, 2008. **266**(12–13): p. 3086-3090.
71. Morent, R., N. De Geyter, C. Leys, L. Gengembre, and E. Payen, *Study of the ageing behaviour of polymer films treated with a dielectric barrier discharge in air, helium and argon at medium pressure.* Surface and Coatings Technology, 2007. **201**(18): p. 7847-7854.
72. Vesel, A., I. Junkar, U. Cvelbar, J. Kovac, and M. Mozetic, *Surface modification of polyester by oxygen- and nitrogen-plasma treatment.* Surface and interface analysis, 2008. **40**(11): p. 1444-1453.
73. Shao, T., C. Zhang, K. Long, D. Zhang, J. Wang, P. Yan, and Y. Zhou, *Surface modification of polyimide films using unipolar nanosecond-pulse DBD in atmospheric air.* Applied surface science, 2010. **256**(12): p. 3888-3894.
74. Stevens, A., *Plasma Energy Dose per Needle*, M.H.A.v. Dongen, Editor. 2013, InnoPhysics B.V.: Eindhoven.

75. Liu, C., N.M.D. Brown, and B.J. Meenan, *Statistical analysis of the effect of dielectric barrier discharge (DBD) operating parameters on the surface processing of poly(methylmethacrylate) film.* Surface Science, 2005. **575**(3): p. 273-286.
76. Dongen, M.H.A.v., R.O.F. Verkuijlen, R. Aben, and J.P.C. Bernards, *Wettability and Ageing of Polymer Substrates after Atmospheric Dielectrical Barrier Discharge Plasma on Demand Treatment*. 2013, Fontys University of Applied Sciences, Eindhoven, The Netherlands.
77. Castro Vidaurre, E., C. Achete, F. Gallo, D. Garcia, R. Simão, and A. Habert, *Surface modification of polymeric materials by plasma treatment.* Materials Research, 2002. **5**(1): p. 37-41.
78. Tsuchiya, Y., K. Akutu, and A. Iwata, *Surface modification of polymeric materials by atmospheric plasma treatment.* Progress in organic coatings, 1997. **34**(1): p. 100-107.
79. Menard, E., M.A. Meitl, Y. Sun, J.U. Park, D.J.L. Shir, Y.S. Nam, S. Jeon, and J.A. Rogers, *Micro-and nanopatterning techniques for organic electronic and optoelectronic systems.* Chem. Rev, 2007. **107**: p. 1117–1160.
80. van Osch, T.H., J. Perelaer, A.W. de Laat, and U.S. Schubert, *Inkjet Printing of Narrow Conductive Tracks on Untreated Polymeric Substrates.* Advanced Materials- Deerfield Beach, 2008. **20**(2): p. 343.
81. Perelaer, J., B.J. de Gans, and U.S. Schubert, *Ink-jet Printing and Microwave Sintering of Conductive Silver Tracks*.* Adv. Mater, 2006. **18**: p. 2101-2104.
82. Dongen, M.H.A.v., R.O.F. Verkuijlen, and J.P.C. Bernards. *Inkjet Printing of Functional Materials on Selectively Plasma Treated Surfaces*. in *LOPE-C*. 2011. Frankfurt, Germany.

# 3 Coalescence and mixing of droplets

Coalescence and mixing of droplets on a solid surface is of great interest in many fields of applications, like inkjet printing. Next to the traditional printing industry with coloured inks, emerging markets like printable electronics, biological materials and microchemistry for e.g. Lab-on-a-chip devices are using inkjet printing to deposit materials. The advantages of inkjet printing to deposit droplets of varying composition and volume with high accuracy and consistency make it an interesting technology for these new fields of process technology [1-3]. For printing applications, the printing of consecutive droplets onto, or close to each other is standard practice. Understanding the following coalescence and mixing of the content of these droplets is therefore of upmost importance. Extensive investigations were done on the dynamics of two coalescing droplets on a solid substrate, both experimentally and numerically, driven by surface tension. Special attention has been spent in these studies to the formation of the bridge between the two droplets. Numerous authors describe this bridge formation in the early stage of coalescence of equally sized droplets distinguishing between two regimes governed by either viscous or inertial forces. Whether, viscous or inertial forces control the dynamics is determined by the Reynolds Number; $\mathrm{Re} = \rho\gamma R / \eta^2$ where $\rho$ is the density, $\gamma$ the surface tension, $R$ the width of the bridge and $\eta$ the viscosity. For $\mathrm{Re} \ll 1$, the merging process is dominated by viscous forces. For low viscosity fluids used in inkjet printing, the cross-over from the viscous regime to the inertial regime is normally very fast as the bridge radius quickly outgrows the viscous length ($l_v = \eta^2 / (\rho\gamma)$). For example, for water the viscous length equals approx. 10 nm. [4-7]. These fast coalescence dynamics prove it difficult to experimentally measure the bridge growth, demanding high speed imaging techniques or high viscous liquids [8-10]. More recently, the effect of geometry on the coalescence dynamics was investigated [11-13]. Ristenpart et al. found for silicone oil on perfectly wetting substrates that the droplet height and radius have a large influence on the growth rate of the bridge. Lee et al. investigated two coalescing drops on partially wetting substrates. The experiments were conducted in the viscous regime showing a power law dependency in the time evolution of the geometric details such as bridge height (exponent in the range of 0.56 to 0.86) and width (exponent equal to 0.29). Eddi et

al. investigated the coalescence dynamics of equally sized water drops for contact angles up to 90 degrees. They find for drops with a contact angle lower than $90^0$ a power law exponent of 2/3 and for contact angles at $90^0$ a power law exponent of 1/2 for the bridge growth.

Less investigated, but equally as important regarding printing applications, is the internal mixing during and after the coalescence. Several methods were used by different authors to visualize the internal flows during coalescence [14-16]. They particularly focused on the early time coalescence when large convective flows are still present in the merging droplets. Verdier and Brizard investigated the internal flows in equally sized droplets with particle image velocimetry, showing symmetry across the bridge in particle flows and no particles crossing the bridge. Castrejón-Pita et al. looked at the coalescence dynamics of coloured and uncoloured inkjet printed drops on partially wetting substrates and compared this to lattice-Boltzmann simulations showing good qualitative agreement [17]. In developing a novel process to synthesize nylon via inkjet printing, reactive components were printed using two reactive mixtures printed on top of each other to initiate the reaction on the substrate [18]. Other authors also used coloured droplets by using dyes to investigate the mixing and coalescence of two droplets for both equally and unequally sized droplets [6, 19]. Recently Liu et al. performed a computational study on binary collision of droplets. These experiments showed the importance of the droplet size ratios on the mixing between the two droplets. For equally sized drops, due to symmetry, the mixing is minimized. As the size ratio increases, the smaller droplet moves into the larger droplet creating a vortex. This vortex enhances local mixing. The energy for this mixing lies in the differences in internal pressure as described by Young et al. and Laplace et al. [20, 21]. The above-mentioned studies focus on the coalescence dynamics, either on the formation of the bridge, or on the mixing during the early stages of the coalescence. The studies do also show that mixing of the droplets after this early stage is not yet complete; however, no indications are given on the timescale needed to reach complete mixing either by convection driven flows due to the mixing by self-diffusion of solutes within the liquid.

In this chapter, droplet coalescence for relatively large drops and small inkjet printed droplets is investigated. The first part (paragraph 3.1) will focus specifically on the bridge formation of relatively large silicone drops of equal volume. The coalescence of these drops takes place in the inertial regime. The second part (paragraph 3.2 and 3.3) concerns the coalescence of small inkjet printed drops with the dynamics in the viscous regime. The emphasis of these paragraphs is focused on the time resolved material transport of fluorescent dyes, present in the drops and will be both experimentally performed and numerically simulated for droplets of equal and unequal volume. Parts of these results are published and presented at international conferences [22, 23].

## 3.1 Coalescence dynamics of spreading silicone droplets

### 3.1.1 Introduction

When two liquid drops on a wettable surface come into contact, they may merge into a single drop. The dynamics of the merger or coalescence of two droplets is of interest in many fields of applications, like sintering, inkjet printing, or condensation. In this paragraph, we focus on measurements of the development of the bridge between the two merging drops (Figure 3.1).

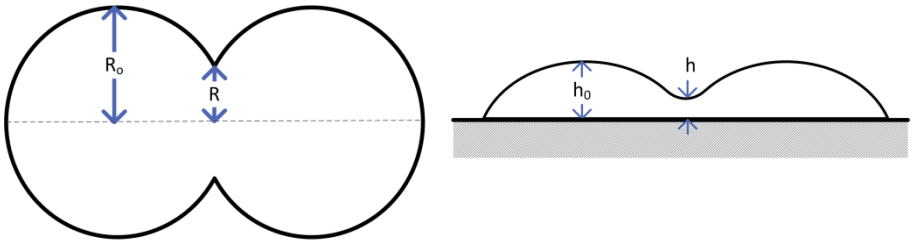


**Figure 3.1: Schematic representation of two coalescing drops of equal size with $R_0$, the initial drop diameters, R the half width of the emerging bridge (top view), $h_0$, the initial drop height and h, the height of the bridge.**

On formation of the bridge, viscous forces and inertial forces control the velocity of the formation speed of the bridge. The formation of the bridge and the associated fluid flows can be described by the Navier-Stokes equations [24, 25]. The change-over from the viscous to inertial regime is defined by the capillary number; $Ca = \eta \cdot v / \gamma = 1$ and the Reynolds number; $\mathrm{Re} = \rho\gamma R / \eta^2$, where $\eta$ is the viscosity, $v$ is velocity of the spreading bridge, $\gamma$ is the surface tension, $\rho$ is the density and $R$ the half width of the bridge. For Re<1, viscous forces dominate the merging of the droplets. The rate of the bridge growth in this regime is linear in time with a small logarithmic dependency with $R_0$ the radius of the initial droplet [26]:

$$R(t) = -\frac{\gamma t}{\pi\eta}\ln\left(\frac{\gamma t}{\eta R_0}\right) \tag{3.1}$$

The inertial regime, with Re> 1, is reached as the bridge radius becomes larger than the viscous length; $l_v = \eta^2 / (\rho\gamma)$. For low viscosity inks, this viscous length is very small,

e.g. for water $l_v \approx 10$ nm [4-7]. Only with high viscosity liquids and/or high speed imaging, the bridge formation in this regime can be experimentally accessed. Ristenpart et al. found for silicone oil on perfectly wetting substrates that the droplet height and radius have a large influence on the growth rate of the bridge (3.2).

$$R \sim \left( \frac{\gamma h_0^3}{\eta R_0^2} \right)^{0.5} t^{0.5} \tag{3.2}$$

Eddi et al. investigated the coalescence dynamics of equally sized water drops for contact angles up to 90 degrees [13]. They found for drops with a contact angle lower than 90 degrees, a power law exponent of 0.66 describing the time evolution of the bridge and for contact angles at 90 degrees a power law exponent of 0.5.

In this paragraph, the coalescence dynamics of silicone drops on glass substrates is investigated. With a viscous length $l_\upsilon \approx 0.5$ mm, the material properties of silicone oil place the experiments for the largest part in the inertial regime with Re≈40. This corresponds with the experiments of Ristenpart et al, with which the data will be compared.

## *3.1.2 Experimental*

40 µl spherical drops of silicone oil were spaced 16 mm apart from centre-to-centre on clean glass slides. The glass slides were thoroughly cleaned before use by washing them rigorously with detergent, isopropanol and deionized water before drying with air. Silicone oils with a viscosity of 10, 50, 100 and 500 mPa·s (Sigma-Aldrich) were used. The surface tension of the silicone oils is approx. 20±2 mN/m, yielding a contact angle on glass below 5 degrees. Two experimental setups were used. The first setup used an Olympus BX60 microscope and Canon EOS6D camera at 50 fps with a magnification of 40x. The second setup consisted of an overhead projector, projecting the coalescing drops on a projecting screen (Figure 3.2). The resulting image was filmed using a 25 fps Ueye USB camera connected to a PC. Both setups were capable of capturing the coalescence. The major differences in both setups are the magnification and contrast. The microscope method has an excellent contrast and resolution, but due to its magnification can only capture a small part of the droplets. This leads to a short time frame in which the coalescence can be monitored. The overhead projector method is able to capture both droplets completely for the whole time frame the coalescence partakes. The camera, however, has less contrast and resolution. The movies created by both methods were analysed using Labview with Vision Assistant (National Instruments).

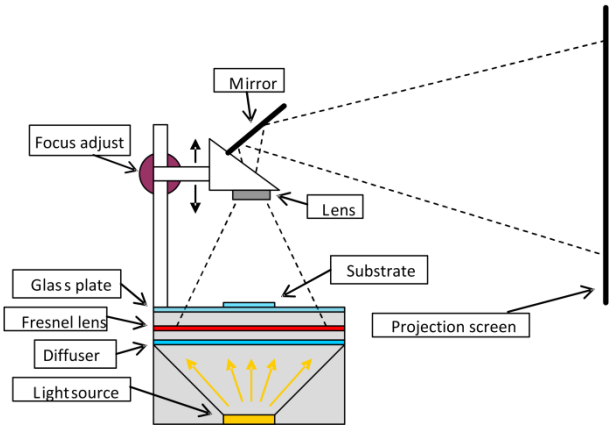


**Figure 3.2: Overhead projection setup.**

### *3.1.3 Results and Discussion*

A typical example of a coalescence experiment is shown in Figure 3.3. Two droplets of silicone oil spread out on the glass substrate prior to contact, due to their low contact angle. On contact, the droplets coalesce and a bridge is formed. Due to the size of the droplets and the minimum magnification of the optical microscope, only a small part of the droplets and bridge is shown on camera. As a result, for silicone oil with a viscosity of 100 mPa·s only the first 5 seconds could be visualized with this camera setup. To be able to measure the coalescence dynamics for a longer period of time, the overhead projector method was used for the following experiments. An example is shown in Figure 3.4.

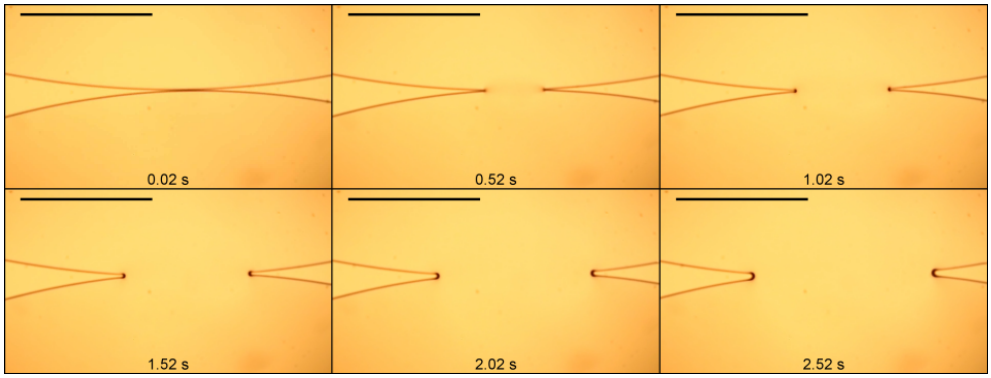


**Figure 3.3: Optical microscopy images of two silicone oil droplets of 970 mPa·s coalescing on a glass substrate. (Scale bar equals 1 mm, time between frames 0.5 s).**

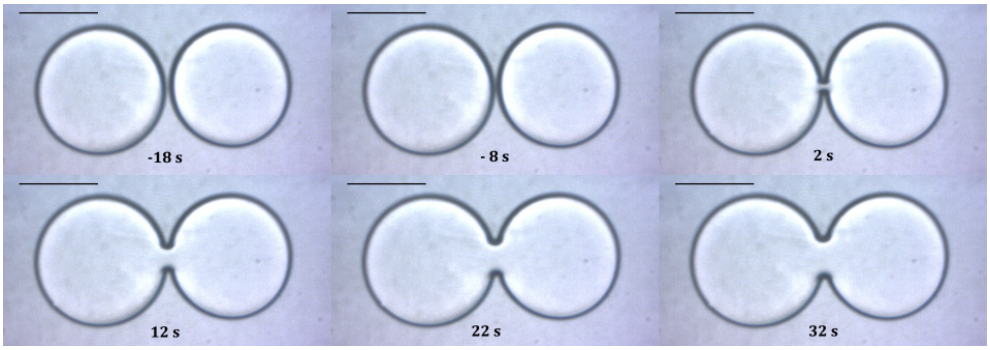


**Figure 3.4: Two silicone drops (η=100 mPa·s) coalescing on a glass substrate captured using the overhead projection method (scale bar is 10 mm, time between frames 10 s).**

The radius of the bridge is plotted versus time for three different viscosities (Figure 3.5). At t=0, the droplets merge and the bridge starts expanding. With increasing viscosity, the bridge grows slower as the capillary velocity ( $\eta / \gamma$ ) decreases.

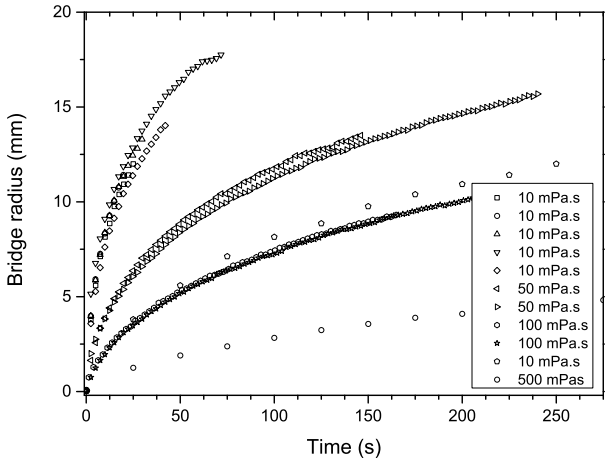


**Figure 3.5: Bridge radius plotted versus time for 40 µl coalescing silicone drops with viscosities of 10, 50, 100 and 500 mPa·s.**

Although the viscosity had a large influence on the velocity of the bridge growth, the coalescence dynamics take place primarily in the inertial regime, as depicted by the Reynolds number. At the cross-over between the viscous and inertial regime (*Re=1*), the bridge diameter for the 10, 50, 100 and 500 mPa·s silicone oils equals approx. 5 µm, 0.1 mm and 0.5 mm respectively. This corresponds with a time of 25 ms for the 100 mPa·s silicone oil and even less for the lower viscosity oils, placing the coalescence dynamics in

the inertial regime. In the inertial regime, the bridge diameter can be rescaled using equation(3.2). As the initial height ($h_0$) cannot be determined experimentally with the current measurement setup, the initial height is estimated via Tanner's Law [27].

$$h_0 \approx R_o \left( \frac{\eta}{\gamma} \frac{dR}{dt} \right)^{1/3} \tag{3.3}$$

By using Tanner's law, it is possible to take in account different droplet sizes and heights during the experiments. Rescaling the experiments from Figure 3.5 with the scaled bridge radius ($R/R_0$) and the dimensionless time ( $\tau = \left( \gamma \cdot h_0^3 / \eta \cdot R_0^4 \right)\left( t - t_0 \right)$ ) leads to Figure 3.6. At first glance, the data do not overlap as well as compared to curve presented by Ristenpart et al. Although, when plotted vs the power-law function of equation (3.2) with $R / R_0 \sim \tau^{0.5}$ on a log-log scale (Figure 3.6b) a good fit was found with a $R^2$=0.99.

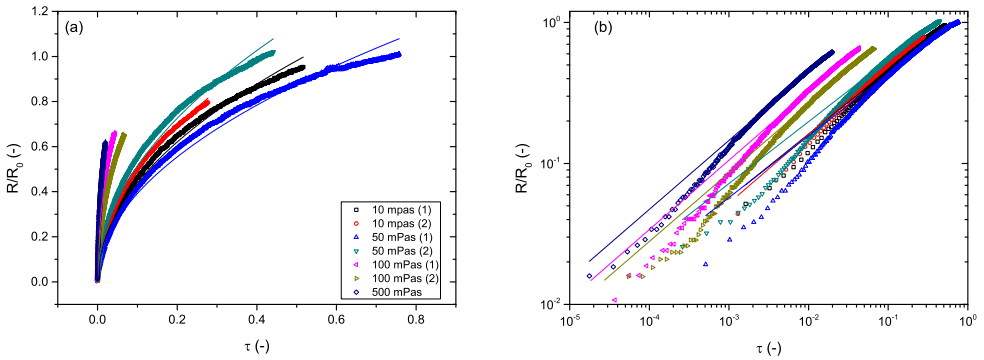


**Figure 3.6: (a) Scaled bridge diameter over initial drop radius $R/R_0$ versus $\tau$ and (b) in a log-log scale.**

Determination of the initial moment of coalesce from the is difficult as mentioned by Ristenpart et al and Lee et al. as well. In Figure 3.3 and Figure 3.4, the dark outline of the droplets is used to calculate the droplet diameter and thus determine the moment of coalescence and the initial height at this time. The analysis of the initial droplet growth velocity ( $dR / dt$ ) depends strongly on the grey-threshold value of the outline and is very sensitive to small changes therein. As a result, $t_o$, $\tau$ and $h_o$ change as well. Slight adjustments in the grey-threshold value for each video leads to new $t_o$, $\tau$ and $h_o$ values, and a correction of Figure 3.6 to Figure 3.7.

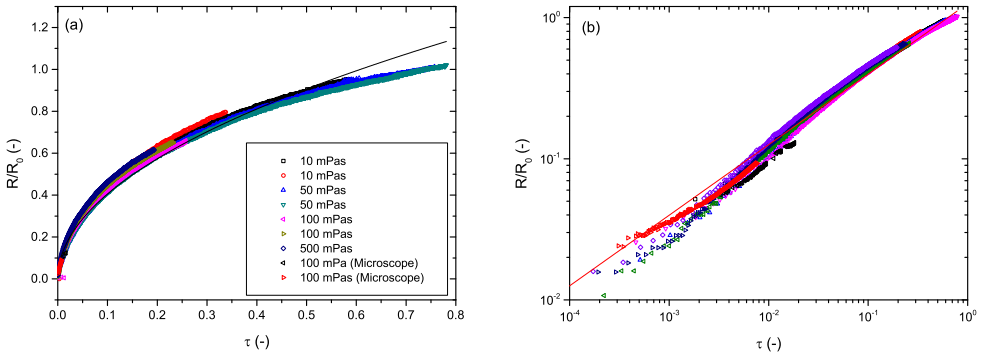


**Figure 3.7: (a) Scaled bridge diameter over initial drop radius R/$R_0$ versus $\tau$ and (b) in a log-log scale after re-estimation the initial height.**

After the re-estimation of the initial height, the scaled diameters for all experiments overlap onto the master curve as first described by Ristenpart. Furthermore, when the scaled data are plotted vs the power-law function of equation (3.2) with $R/R_0 \sim \tau^{0.5}$ on a log-log scale (Figure 3.7b), the results fit very well with a $R^2$=0.98. Although this shows that the determination of the initial height of the droplet is a very important parameter in the scaling of the data, the initial droplet height has limited influence on the time-scale of the bridge dynamics. This still follows $R \sim t^{0.5}$.

## *3.1.4 Conclusions*

The coalescence dynamics of silicone oil on a fully wetting glass substrate was investigated. The bridge radius scaled with a power law of $R/R_0 \sim \tau^{0.5}$, which is in good agreement with the experiments performed by Ristenpart et al.. The determination of the moment of coalescence, followed by a good approximation of the initial height of the bridge proved challenging with only top-view imaging available.

## 3.2 Time resolved coalescence and mixing of inkjet printed droplets

### 3.2.1 Introduction

In this paragraph, we will investigate the mixing of two coalescing drops of different volume ratios on a partially wetting glass substrate. Each deposited droplet contains a different fluorescent dye, dissolved in a low viscous liquid. The droplets are inkjet printed on glass slides with sufficient pitch to prevent coalescence on and directly after impact. The coalescence is initiated by exposing the glass substrate to UV-light decreasing the contact angle of the liquid. Increasing the wettability of glass by UV is well known effect and commonly used in UV-ozone cleaning apparatus [28-30]. The decrease in contact angle of the liquid is sufficient to increase the droplet radii, forcing them to touch and coalesce. Upon coalescence, the transport of the fluorescent dyes is monitored from above by fluorescent microscopy. The time-evolved concentrations of both dyes are calculated and compared to numerical 1D simulation. An indication of the duration and influence of the convective flows compared to diffusion-based transport of the dyes for both the equally and unequally sized drops is presented.

### 3.2.2 Experimental Details

Diethyleneglycol-Dimethacrylate (Sigma Aldrich), in short DEGDMA, was used with 0.1 wt% fluorescent dye. To follow the mixing behaviour during the merging of the two droplets two fluorescent dyes were chosen: Lumogen Red 94720 (Perylene, Kremer Pigmente GmbH) and Coumarin 153 (Sigma Aldrich), referred to in the following as dye A and dye B. The two liquids containing either dye A or dye B were inkjet printed with a Roth & Rau Pixdro LP50 inkjet printer equipped with two Spectra SE print heads. Two rows of droplets (dye A and B) of approx. 28 pl, were printed at a sufficiently large pitch such that they do not touch each other during impact on standard microscopic glass slides (76x24 $mm^2$). The glass slides were used as delivered from the box without any cleaning. Droplet volumes were measured in flight with the camera system on the LP50 inkjet printer. After impact, a single droplet changed into a hemisphere of approx. 100 µm in diameter on the glass slide with a contact angle of 30-34 degrees as measured with a Dataphysics OCA-30. For the experiments with unequally sized droplets, the row of droplets of one dye was printed repeatedly at the same position, creating droplets of multiples of 30 pl. Viscosity and interfacial tension were experimentally determined at 6.7 mPa·s (Rheometric

Scientific SR-5000) and 32 mN/m (Dataphysics OCA-30) for both liquids. After printing the glass slides with droplets were placed under a fluorescent microscope (Olympus BX60, magnification 100x, Osram 103/W2 Hg-lamp, 170000 cd/cm²) and filmed at 50 fps (Canon EOS 6D) to track the coalescence and mixing process. Experimentally it was found that, under UV-exposure, both fluorescent dyes and in particular, the green dye bleaches out after several minutes. In order to minimize the effect of this bleaching on the experimental results, only coalescence experiments with less than 2 minutes UV-exposure before coalescing were analysed. The effect of UV-light on the wetting behaviour of inkjet printed DEGDMA droplets on glass was measured by determining the droplet radius with and without UV-Exposure under the fluorescent microscope employing the UV-lamp of the microscope as UV-source. The position ($x(t)$) of concentration ratio ($C/C_0=0.1$) was calculated using National Instruments Labview from the intensities of the RGB profiles of the fluorescent dyes. An explanation of the conversion from RGB-profiles to the dye concentrations is discussed in the following section.

### *3.2.3 Determination of the Concentration Ratio*

When two droplets merge, the growth of the meniscus bridge is fed by the transport of material from the bulk of the droplet to the bridge. The velocity by which the material is transported is governed by the balance between viscous and inertial forces and can be described by the Navier-Stokes equations [24, 25]. For two droplets of equal size, symmetry exists across the bridge and material transport across the bridge will be negligible. For coalescing droplets of unequal volume, however this symmetry no longer is present. Due to the differences in drop radii, an internal pressure difference is present at the instant of coalescence, driving a net material flow from the small droplet into the larger droplet passing the initial bridge. This convective transport is strongest in the initial stages of the coalescence as the growth of the bridge is also strongest. In the later stages of the coalescence, as the pressure differences subside and the bridge growth slows down, this convective transport across the bridge also dies out. In the case of two droplets of different composition, e.g. containing different solutes, a second type of material transport is also present in the form of diffusion. The diffusion of a solute over time is determined by the concentration gradient and the diffusion coefficient $D$ of the solute in the solvent, as described by Fick's second law of diffusion [31]. Compared to the convective flows generated by the bridge opening, diffusion is much slower, but continues until no concentration gradient exists. To distinguish between the surface tension induced flows and diffusion, the concentration gradient of a dye is followed lengthwise along the droplet, perpendicular to the bridge direction (Figure 3.8). For droplets of equal volume,

no net material surface tension driven flows across the bridge are present. Transport of a dye across the bridge can therefore only be driven by diffusion due to the concentration gradient. Considering a 1D approximation along the centreline of the merging droplets, Fick's second law of diffusion equals:

$$\frac{C}{C_0} = \frac{x}{2\sqrt{\pi \cdot D \cdot t}} \exp\left(\frac{-x^2}{4 \cdot D \cdot t}\right) \tag{3.4}$$

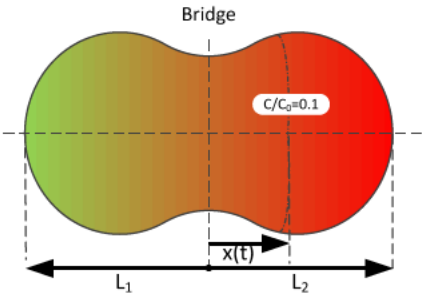


**Figure 3.8: Schematic drawing of a coalesced drop. The position, *x(t)*, of the concentration gradient *$C/C_0$=0.1* relative to the bridge is monitored in time along the length of the droplet for a single dye. *$L_1$* and *$L_2$* are the respective lengths of each original droplet from the edge to the bridge.**

Here $C_0$ and $x$ represent the initial concentration of a dye in the original droplet and the position of the concentration gradient $C/C_0$ at time $t$, respectively. For a concentration ratio $C/C_0=0.1$ and known diffusion coefficient, the position $x(t)$ can be calculated at any given time. In the experiments, the concentration ratio $C/C_0$ of a solute cannot be easily determined. Two different fluorescent dyes were therefore used as solutes. Under UV-exposure, the two dyes emit green or red light respectively. During an experiment, the RGB-profiles of the coalescing droplets are extracted frame by frame. For both dyes no light intensity is measured in the blue profile, therefore the blue profile is discarded and calculations are done with the red and green intensity profiles (Figure 3.9a). During the coalescence process, the dyes are transported across the bridge due to convection and/or diffusion, altering the RGB-intensity profiles on both sides of the bridge. The RGB-profiles can therefore not be used directly to determine the concentration ratio $C/C_0$ at a specific position and time and have to be corrected. The intensity $I$ for both dyes A (Perylene) and B (Coumarin 153) are described by:

$$I_a = \begin{pmatrix} I_{a,R} \\ I_{a,G} \end{pmatrix} \quad \text{and} \quad I_b = \begin{pmatrix} I_{b,R} \\ I_{b,G} \end{pmatrix} \tag{3.5}$$

The indices *a* and *b* indicate the dye and *R* and *G* indicate the red and green profile for specific dye. Under the assumption, that both dyes have a linear response in both the red and green intensity, the relationship between a dye and its concentration (*C*) can be formulated as:

$$I = C \cdot I^0 = C \begin{pmatrix} I_R^0 \\ I_G^0 \end{pmatrix} \tag{3.6}$$

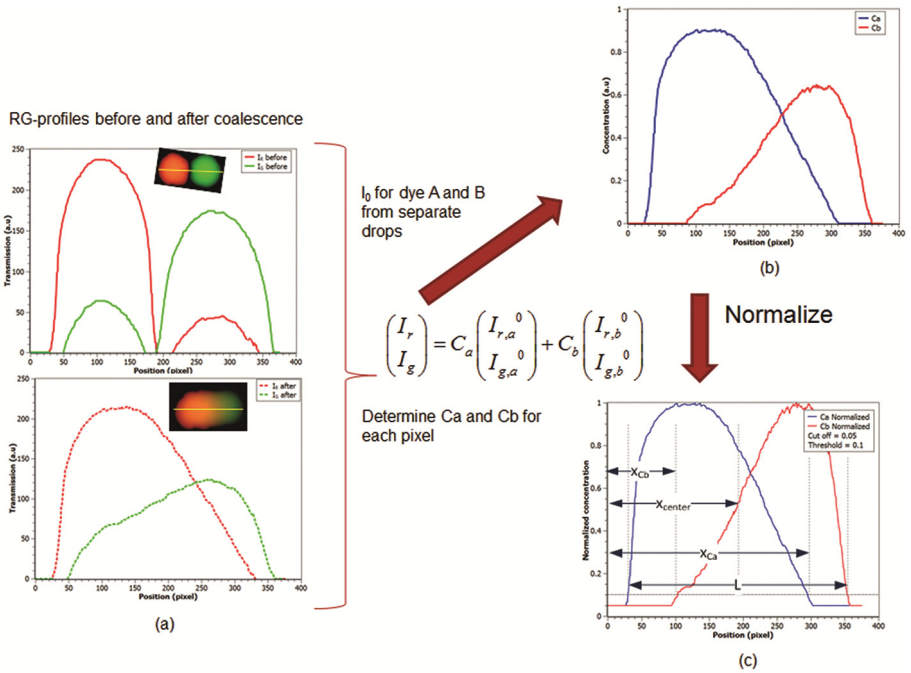


**Figure 3.9: Determination of the position *x(t)/L* from RGB-intensity measurements for the concentration ratio *$C/C_0$=0.1*. (a)The red and green (RG) intensity profiles are shown for the last frame before coalescence and a frame after coalescence for the image in the inset. From the intensity measurements in (a) the concentration of each dye (*$C_a$* and *$C_b$*) is calculated over the length of the coalesced drop (b). This profile is then normalized (*c*) for drop A and B and the frontline position *$x_{Ca}$* and *$x_{Cb}$* for both dyes as well as the length of the coalesced drop (*L*) are determined using a threshold of 0.1 in the normalized dye concentration.**

In equation (3.6), $I^0$ is the RG-intensity of the dye measured just before coalescence (top image in Figure 3.9a). After coalescence the droplets mix and transport of the dye from one side of the coalesced droplet to the other starts resulting in a combined RG intensity spectrum ($I_{a+b,x}$) over the length of the droplet (bottom image Figure 3.9a). Combining equations (3.5) and (3.6), the concentrations $C_a$ and $C_b$ for both dyes can be calculated at each position x for all frames (i.e. time) (Figure 3.9b):

$$I_{\mathrm{a+b},x} = \begin{pmatrix} I_R \\ I_G \end{pmatrix}_x = I_{a,x} + I_{b,x} \rightarrow I_{tot,x} = C_{a,x} \cdot I_a^0 + C_{b,x} \cdot I_b^0 \tag{3.7}$$

After normalization of dye intensity and differences in droplet sizes ($L$), the relative position of each dye $x(t)/L$ can be determined for a chosen concentration ratio of $C/C_0 = 0.1$ (Figure 3.9c). The experimentally determined $x(t)/L$ is then compared to the $x(t)/L$ based equation (3.4). If convective flows cross the coalescence bridge, deviations in the comparison between experimental and theoretical $x(t)/L$ should be visible.

## *3.2.4 Results and Discussion*

The coalescence of two inkjet printed drops is initiated by exposing the glass substrate containing the drops of DEGDMA with red and green fluorescent dyes to the UV-light of the fluorescent microscope. Experiments showed that upon UV-exposure, the wettability of DEGDMA on the glass substrate changes. This effect is also commonly seen in e.g. UV-ozone cleaning apparatus [28-30]. In our experiments, this change in wettability of the glass was sufficient to increase the drop radii of DEGDMA with 4-5% upon UV-irradiation as is shown in Figure 3.10. When printed sufficiently close to each other, this small increase in drop radii forced the drops to approach each other and, upon touching, to coalesce. If no coalescence occurred within two minutes after initiating UV-exposure, the experiment was stopped in order to prevent quenching effects of the fluorescent dyes influencing the concentration measurements.

Two sets of experiments were performed to investigate the internal flows of coalescing droplets with equally sized and unequally sized droplets up to a volume ratio of 4:1. The corresponding droplet radii range from 50 µm to approx. 75 µm. The larger droplet volumes were created by inkjet printing up to four times at the same spot creating the larger droplet.

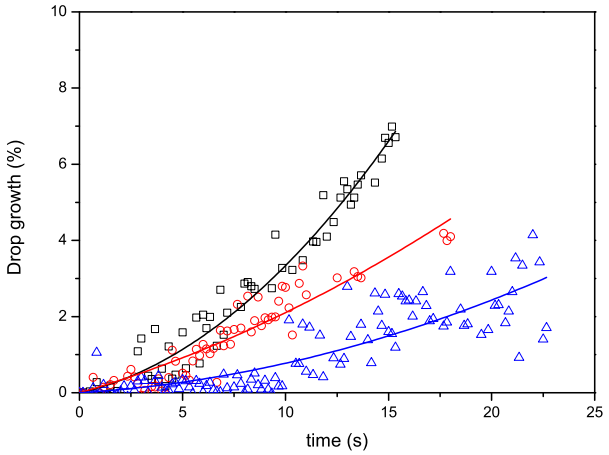


**Figure 3.10: Relative change in droplet radius of inkjet printed droplets under UV-exposure by a fluorescent microscope. At *t=0* s the UV-exposure is started. Starting droplet radii 50 µm (○), 48 µm ( □) and 41 µm (△). Solid lines are for clarification.**

This corresponds to Reynolds numbers ranging from 40-70 and a viscous length $l_v$ of approx. 13-20 µm, with a characteristic time of 2-3 µs to cross from the viscous to the inertial regime. Following the evolution of the bridge closely would require high-speed imagery equipment, which were unavailable for these set of experiments. Instead, we followed the merging of the droplets at a slower frame rate (50 fps) for a longer duration of up to two minutes with goal of tracking the transport of the dyes due to convection, at the early stages, and diffusion at later stages of the coalescence. Figure 3.11 shows a typical time resolved montage of two equally sized droplets during coalescing. Clearly visible is the fast growing bridge in the first few frames of the montage from 40 to 60 ms, in which the bridge radius reaches approx. 60% of the initial droplet diameters. From *t=60 ms* and on, the bridge growth slows down considerably. We found that the bridge stopped growing when the initial droplet diameters were approx. reached. In the time duration of the experiments, i.e. max. 2 minutes, the coalesced drop never showed any tendency to become hemispherical. This is the well-known viscosity effect, stopping the moving contact line of the bridge, pinning the droplet in a "tube"-like shape as described by among others [11, 12, 14] Also clearly visible is the dye transport over time. Directly after coalescence (*t=0.06 s*), a sharp division between the two dyes is visible located at the centre of the bridge on the symmetry axis between the two droplets. In time, the position of this "front" changes as the dyes are transported across the bridge by diffusion.

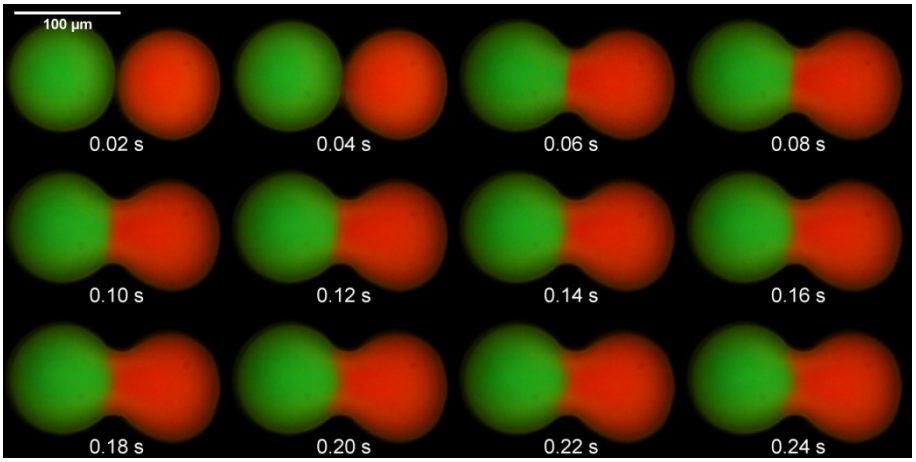


**Figure 3.11: Montage of coalescing droplets of equal volume just before and after coalescence (filmed at 50 fps). (The scale bar for all images is 100 µm).**

To evaluate the transport of the dyes over the bridge, the relative position (*x(t)/L)* of the concentration ratio $C/C_0=0.1$ is derived from each frame and compared with the 1D approximation of Fick's law of diffusion (equation (3.4)) over the length of the droplet. The results are shown in Figure 3.12(a) and (b). As stated earlier, for coalescing droplets of equal volume, the net material flow of the dyes due to surface tension induced flows across the bridge is expected to be negligible along the length of the droplet. For both dyes, it can be seen in Figure 3.12a that *x(t)/L* follows the same behaviour for the first 10 seconds after coalescence. The difference in *x(t)/L* for the green dye compared to the red dye after 10 seconds is due to quenching of the green dye for this particular experiment. In order to distinguish between diffusion based transport and convective transport, the experimental data is plotted versus Fick's Law, as is shown in Figure 3.12b. The diffusion coefficient $D = 2 \times 10^{-9}\, m^2 s^{-1}$ was found for both dyes by fitting the data to equation (3.4). In the early stages of the coalescence, i.e. under one second or $x(t)/L<0.25$, any deviations from the line $y=x$ would indicate the possible contributions of convective flows due to the bridge formation. Figure 3.12b shows that the experimental *x(t)/L* follows *x(t)/L* derived from equation (3.4) very well in this early stage indicating no significant contributions of convective flows are present. At longer periods, it is more difficult to follow the gradient correctly due to nearing the edge of the droplet and quenching of the dyes. This results in the deviation of the experimental data compared to the modelled data in Figure 3.12b for $x(t)/L_{model}>0.8$, especially for the green dye.

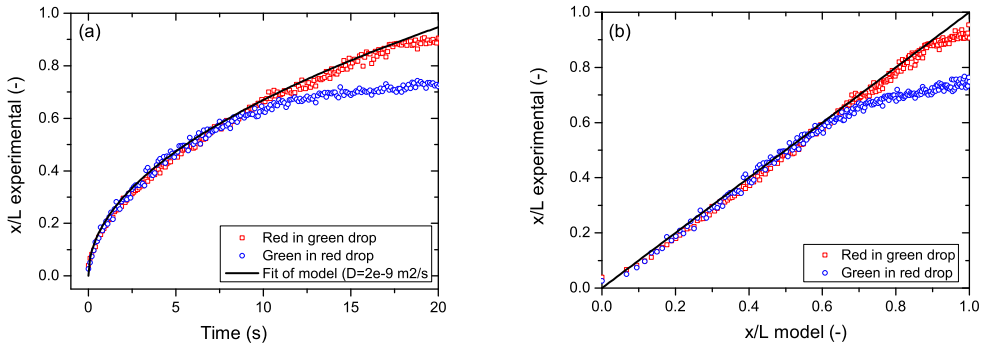


**Figure 3.12: Experimentally determined relative position *x(t)/L* of the concentration ratio (*$C/C_0$=0.1*) of the red and green dye for equally sized drops. (a) versus time, (b) versus calculated *x(t)/L* from 1D model for *$D=2\cdot10^{-9}$* $m^2 \cdot s^{-1}$.**

In Figure 3.13, the first moments after coalescence are shown for two coalescing droplets with volume ratio 4:1. Visible is the inflow of red dye across the bridge from the small droplet into the larger droplet, indicating convective material flow. According to Young-Laplace, the internal pressure in the smaller droplet is higher compared to the pressure in the larger droplet. Upon coalescence, this pressure difference will create a net convective material flow from the smaller to the larger droplet, proportional to the surface tension. According to Lee et al., the bridge width forms much faster than the bridge height [12].This will account for higher velocities of the liquid along the edges of the bridge compared to flows on the top of the droplet. For the unequal sized droplets, due to the internal pressure difference, more material will be transported along the edges of the bridge compared to the centre of the bridge from the small droplet to the larger one. This effect, although not quantitatively measured, can be seen at 0.24 s in Figure 3.13, as the red dye penetrates the bridge further along the edges compared to the centre of the bridge. When the pressure difference subsides and the drop shape becomes stable, the convective flow stops. As the coalescence regime occurs in the viscosity-dominated regime, the drop shape will not reach a complete hemisphere, as it would if the process is dominated by the surface tension. In reality, we observed that the drop shape stabilizes when the bridge radius is approx. equal to the initial drop radii for equally sized droplets, and to approx. the average of the initial drop radii for the unequally sized drops. We found experimentally that this final state, after which the droplet shape hardly changes, is reached less than one second after the coalescence starts.

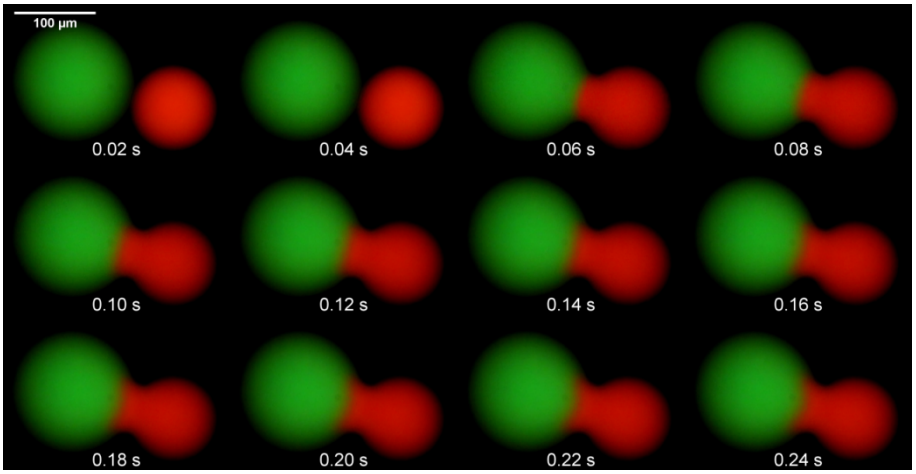


**Figure 3.13: Montage of video-frames just before and after coalescence (filmed at 50 fps) of two droplets with volume ratio 4:1. (The scale bar for all images is 100 µm) .**

Figure 3.14a shows the time-resolved transport of the red and green dyes. In the first two seconds, $x(t)/L$ of both dyes deviate from the curve indicating the expected $x(t)/L$ if only diffusion would be present. This is even more evident in Figure 3.14b in which the experimental $x(t)/L$ is plotted against $x(t)/L$ calculated from equation (3.4). For $x(t)/L$ <0.25, i.e. the first 2 seconds, the transport of the red dye from the small droplet to the large droplet travels faster than expected by diffusion only. This indicates, as expected from the non-symmetry between the droplets, a net flow of material due to convective flows from the small to the large droplet. This small amount of mixing due to convective flows for coalescing droplets is also mentioned by Castrejón-Pita in the case of droplets impacting with each other [17]. For some applications, this effect can be beneficial, like for graphical applications, but for other applications, further mixing might be needed. This can be achieved by diffusion, but this is a slow process regulated by the diffusion coefficient. In our experiments, it took several minutes to achieve complete mixing after the initial coalescence. For the transport of the green dye from the large droplet to the small droplet, a more complex convective flow contribution is seen. For $x(t)/L < 0.1$ or $t < 0.4$ *s*, the convective flows indicated by the green dye from the large to the small droplet appear to move into this direction as well.

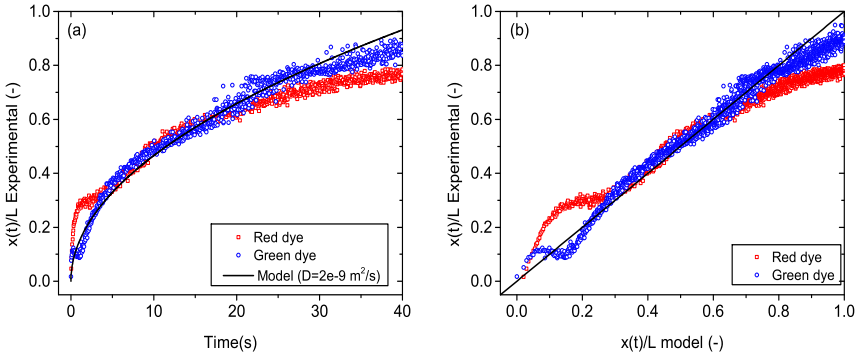


**Figure 3.14: Experimental relative position *x(t)/L* versus (a) time and (b) relative position *x(t)/L* calculated from Fick's law with $D=2\cdot10^{-9}$ $m^2\cdot s^{-1}$ at a concentration ratio of $C/C_0=0.1$ for the volume ratio Green: Red droplet 4:1.**

This is followed by a flow "reversal" from *0.1< x(t)/L<0.25*. This is counterintuitive with the expected convective flows due to the internal pressure difference. This effect is also visible at a lower volume ratio of 2:1 in Figure 3.15. Figure 3.15 shows the combined results of the dye transport for the volume ratios of 1:1, 2:1 and 4:1 for both dyes moving from the small droplet to the large droplet (Figure 3.15a) and vice versa (Figure 3.15b) in the period the convective flows are strongest, i.e. as the bridge is still growing. For the red dye, moving from the small droplet into the larger, the convective contribution is as predicted by the internal pressure difference. It is absent at equally sized droplets, and grows as the internal pressure difference increases, due to the increasing volume ratios. However, the convective contribution for the green dye shows the same complex trend for both 2:1 and 4:1 volume ratios and is equal in size, but smaller compared to the convective flow of the red dye. This indicates a different type of flow, like vortices, might be present, made at the early formation of the bridge. Liu et al. numerically show vortices can occur for unequally sized droplets [32]. Also Gelfgat et al. numerically show the existence of transverse flows along the interface between the moving liquids creating so-called Dean vortices [33]. These vortices enhance local mixing on a small scale in the range of a few micrometres along the interface, which could be the reason of the disagreement between the expected convective flows. As the experimental method used can only analyse the droplets from above, it is not possible to visualize these flows in further detail.

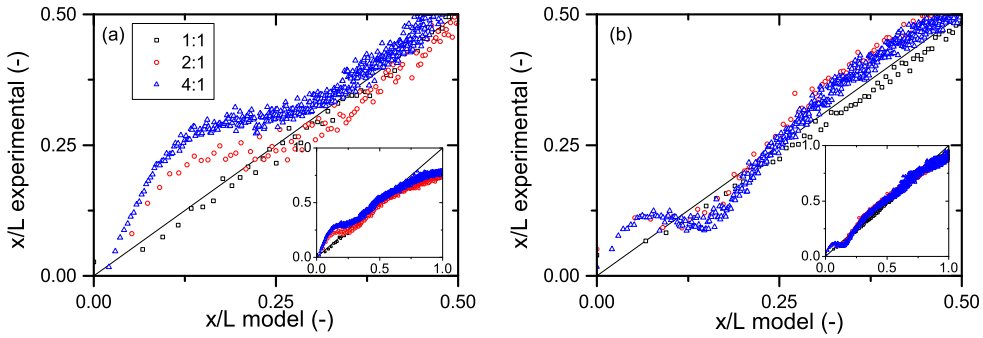


**Figure 3.15: Experimental relative position *x(t)/L* versus relative position *x(t)/L* (*D=2·10*$^{-9}$ m$^2$·s$^{-1}$) for the volume ratios Green: Red droplet 1:1, 2:1 and 4:1. (a) Transport of red dye into (larger) green droplet, (b) transport of green dye into (smaller) red droplet. Inset in both graphs shows the full range of the experiment.**

Further analysis with a different test setup is recommended, but will be extremely challenging due to the small nature and position of these potential vortices within the droplet. As the bridge expansion slows down, the flow along the interface also slows and the flow from the smaller droplet pushes into the larger droplet, reversing the initial mixing of the green dye along the interface until the bridge expansion stops and the convective flows stop as well at $x(t)/L \approx 0.25$. For $x(t)/L > 0.25$, diffusion based transport remains and both dyes are transported into each other's droplet in good agreement to equation (3.4).

## *3.2.5 Conclusions and recommendations*

In this study, the material flows of fluorescent dyes in coalescing small inkjet printed droplets of different volume ratios were experimentally investigated. The focus of the investigation was on both the early time mass transport due to convective flows of the bridge formation and the mass transport on longer time scales when the convective flows dissipate and diffusion becomes dominant. The coalescence of the small inkjet printed droplets was initiated by changing the wettability of the glass substrates under UV-exposure. For droplets of equal volume ratio, it was found that the transport of the dyes could be described fully by diffusion only along the centre axis of the coalescing drops. For unequally sized drops, the contribution of convective flows was shown to be present and have a significant influence in the first moments after coalescence. The convective flow from the small into the large droplet increases in size for increasing volume ratios and is in agreement with current research standings. At the initial moment of coalescence, a counterintuitive flow from the large drop into the small drop was observed. The origin of

this flow might be due to the presence of vortices along the interface of the bridge, due to the strong transverse flow to create the bridge. Further investigation to study this phenomenon is recommended. After the initial bridge formation, we showed that the convective flows stop as the bridge stops growing. From this moment, the mixing continues by diffusion. We found that this could be well described by a 1D approximation of Fick's second law of diffusion.

## 3.3 Simulation of coalescing and mixing small droplets

### 3.3.1 Introduction

In the two previous paragraphs, we investigated the coalescence and mixing behaviour of liquids on (partially) wetting substrates experimentally. We studied the dynamics of the bridge, as well as the time-resolved material transport across the bridge due to convection and diffusion. In this paragraph we will continue these studies by numerical simulation in Comsol Multiphysics [34]. Comsol Multiphysics is a general-purpose software platform, based on the finite elements method, for modelling and simulating physics-based problems. In specific, the experiments performed in paragraph 3.2 will be the basis for the numerical simulations. The transport of the dyes during coalescence will be numerically studied for both droplets of volume ratios 1:1 and 4:1. The simulation will be evaluated by comparing the numerical results with the experimental results from the previous two paragraphs.

### 3.3.2 Simulation Model

The bases of the numerical simulations within Comsol Multiphysics are two physics models to describe the coalescence dynamics and the material transport due to convection and diffusion, respectively. The coalescence dynamics, i.e. the formation of the bridge and ensuing convective flows in the merging droplets are described by the “laminar two-phase flow model”, using a level set interface method. The transport of the dye by convection and diffusion is described by the “transport of diluted species interface”. Both physics models are standard models integrated in Comsol Multiphysics and will be described below.

#### *Laminar Two-Phase Flow, Level Set Interface.*

The laminar two-phase flow model is used to track a (moving) interface between two fluid phases. The interface is based on the Navier-Stokes equations for the conservation of momentum and a continuity equation for the conservation of mass (equations (3.8) and (3.9)).

$$\rho\left(\frac{\delta u}{\delta t}+(u\cdot\nabla)u\right)=-\nabla p+\eta\left(\nabla^2\cdot u\right)+\rho g+F_{st} \tag{3.8}$$

$$\nabla\cdot u=0 \tag{3.9}$$

In equation (3.8), $\rho$ represents the density (kg/m$^3$), $u$ the velocity (m/s), $p$ the pressure (Pa), $\eta$ the viscosity (Pa·s). The force term $F_{st}$ in equation (3.8) represents the surface tension acting on the interface between the liquid and the air and is defined by Lafauri as [35]:

$$F_{st}=\nabla\cdot\left(\sigma\left(I-\left(nn^T\right)\right)\delta\right) \tag{3.10}$$

In equation (3.10) $\sigma$ represents the surface tension (N/m) and $\delta$ the Delta dirac function. The position of the interface is tracked by solving the transport equation for the level set function as depicted by equation (3.11).

$$\frac{\delta\phi}{\delta t}+u\cdot\nabla\phi=\gamma\nabla\cdot\left(\varepsilon\nabla\phi-\phi(1-\phi)\frac{\nabla\phi}{|\nabla\phi|}\right) \tag{3.11}$$

Where $\gamma$ is the re-initialization parameter (equal to 1 m/s) and $\varepsilon$ the interface thickness (1 μm). The density and viscosity in the model are defined by the level-set parameter $\phi$ as:

$$\begin{aligned}\rho&=\rho_1+(\rho_2-\rho_1)\phi\\ \eta&=\eta_1+(\eta_2-\eta_1)\phi\end{aligned} \tag{3.12}$$

Where $\rho_1$, $\rho_2$, $\eta_1$ and $\eta_2$ are the respective density and viscosity of fluid 1 and fluid 2. From the level-set parameter it follows that fluid 1 corresponds to $\phi$<0.5 and fluid 2 corresponds to $\phi$>0.5 [36].

## *Transport of Diluted Species*

The Transport of Diluted Species model describes time evolution of the concentration field of a dilute solute in a solvent. The driving force of the transport of the dye is either convection or concentration gradient. The physics model is governed by the following mass balance equation for a solute [37]:

$$\frac{\delta c}{\delta t}+u\cdot\nabla c-D\cdot\nabla^2 c=0 \tag{3.13}$$

The concentration of the solute is represented by c in mole/$m^3$ with diffusion coefficient *D* in the solvent ($m^2$/s). The velocity, u, derived from the equation (3.8), is only present as long as the bridge grows, after which equation (3.13) equals Fick's law of diffusion as presented in paragraph 3.2. The transport of the diluted species model does not directly account for two phase flow. The diffusion coefficient *D* of the dye therefore has to be modified to take in account both phases using the level-set parameter $\phi$:

$$D = D_1 + (D_1 - D_2)\phi \tag{3.14}$$

## *Geometry and physics settings*

Two geometries were used to define the simulation model. One for the equally sized droplets, the other for the droplet volume ratio of 4:1. Both geometries are shown in Figure 3.16.

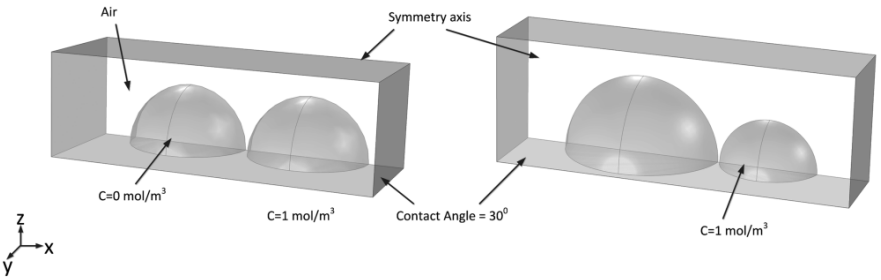


**Figure 3.16: Geometry for coalescing droplets with volume ratio 1:1 and 4:1. Droplets on the right are filled with 1 mol/$m^3$ of dye (distances in µm), initial distance between the droplets equal 2 µm.**

**Table 3.1: Material properties of Air and Di-Ethyleneglycol-dimethacrylate (DEGDMA).**

| Material (solvent) | Parameter | | |
|---|---|---|---|
| **Fluid 1: Air** | Density | 1.25 | kg/$m^3$ |
| | Viscosity | $1.9\cdot10^{-5}$ | Pa·s |
| | Diffusion coefficient | $1\cdot10^{-50}$ (≈0) | $m^2$/s |
| **Fluid 2: DEGDMA** | Density | 1030 | kg/$m^3$ |
| | Viscosity | 0.0067 | Pa·s |
| | Contact angle on glass | 30 | degrees |
| | Diffusion coefficient | $2\cdot10^{-9}$ | $m^2$/s |

The material properties of the two phases, air and DEGDMA are presented in Table 3.1. To prevent diffusion of the dye from the solvent DEGDMA to air in the simulation, the diffusion coefficient in air is set to the minimal allowed value of $1 \cdot 10^{-50}$ $m^2/s$. For the diffusion coefficient of the dye in DEGDMA the value from paragraph 3.2 is used. The coalescence is initiated by gravity forces and a higher initial contact angle ( approx. $60^o$) than the equilibrium contact angle ($30^0$) on the XY-plane. The YZ-plane is defined as symmetry axis to speed up the calculations. At the remaining outside boundaries, the no slip and no flux conditions are imposed. One droplet, i.e. the small droplet in case of the 4:1 volume ratio, contains an initial concentration of 1 $mol/m^3$ of dye. The other droplet contains no dye at the start of the simulation. The simulation is solved with a time dependent solver in the range of $10^{-6}$ to 20 s. The physics settings as well as the domain dimensions are summarized in Table 3.2.

**Table 3.2: Model settings.**

| **Physics** | **Parameter** | | **Settings** |
|---|---|---|---|
| **Laminar two phase flow, Level set** | Interface thickness | | $2 \cdot 10^{-6}$ m |
| | Absolute pressure | | $10^5$ Pa |
| | Temperature | | 293.15 K |
| | Gravity | | 9.81 m/s (all domains) |
| | Domains | Droplet 1 | P=600 Pa |
| | | (DEGDMA) | r= 50 µm |
| | | Droplet 2 | P=600 Pa |
| | | (DEGDMA) | r= 50 µm |
| | | | r= 80 µm (ratio 4:1) |
| | | Air | P= 0 Pa |
| | Boundaries | Outside walls | No slip |
| | | Wetted wall | $\theta=30^0$ (XY , z=0) |
| | | Symmetry | YZ (x=0) |
| | Point | Pressure point | 0 Pa (x=y=z=0) |
| **Transport of diluted species** | Transport mechanism | Diffusion constant in DEGDMA | $2 \cdot 10^{-9}$ $m^2/s$ |
| | Domains | Droplet | C=1 $mol/m^3$ |
| | | Other droplet, Air | C=0 $mol/m^3$ |
| | Boundaries | Outside walls | No flux |
| | | Symmetry | YZ (x=0) |
| **Mesh** | | Fluid dynamics | Tetrahedral, Fine |
| **Solver** | Time Dependent | Range | 10^(range(-7,0.1,-3)) s |
| | | | 10^(range(-4,0.1,1.6)) s |
| | | Method | Generalized alpha |
| | | Iterative | GMRES |

### 3.3.3 Results and discussion

Numerical simulations of coalescing droplets were performed for the volume ratio of 1:1 and 4:1. The origins of the simulations were the experiments performed in paragraph 3.2, to evaluate the contribution of the convective flow in the mixing of a (simulated) dye in the coalescing droplets. Comparable to the experiments, in one droplet a dye is present with a concentration of 1 mole/$m^3$. In the other droplet, the dye is absent. Upon coalescence of the two droplets, the bridge between the droplets is formed and convective flows in the droplets appear. Also due to the concentration gradient, diffusion of the dye will take place due to the presence of a concentration gradient over the bridge.

Recollecting the experimental results from the previous paragraph, the growth of the bridge occurs fast, expanding up to 60% of the original drop diameters in the first 20 ms. Next, the expansion slows down, and eventually stops at approx. 80% of the original drop diameters after 0.5 s. This occurred for the coalescence of both the droplets of equal and unequal size. Figure 3.17 and Figure 3.18 show the numerical simulations of both the equally and unequally sized coalescing droplets. Evaluating the time evolution of the droplet shapes for both simulations, the shapes follow the expected theoretical evolution from two singular drops to a hemispherical shape. However, when put next to the two equivalent experiments from the previous paragraph, the simulations differ in two aspects. First, the droplet shape in the experiments becomes pinned after approx. 0.5 seconds. This is not the case in the simulations. Second, the speed of the coalescence in the simulations also differs from the experiments. The simulation appears to be approx. ten times faster in the growth of the bridge when compared to the experiments as the width of the bridge is already larger than 80% after 0.1 ms in the simulation

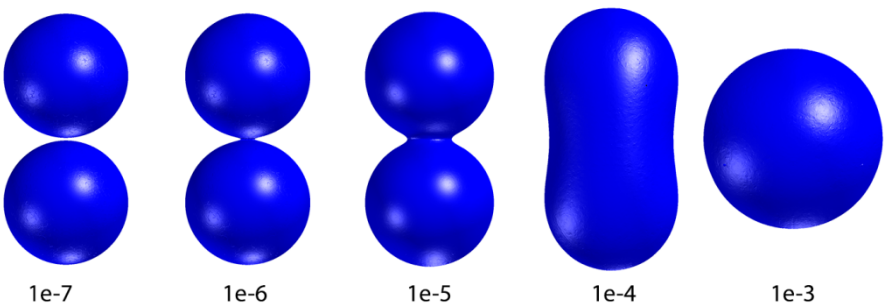


**Figure 3.17: Top view of the time-evolved droplet shape of two equally sized coalescing droplets (time in seconds).**

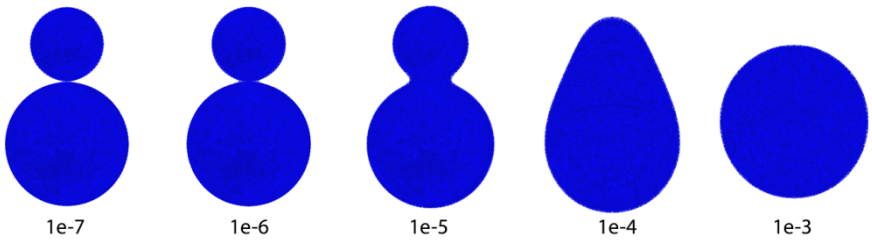


**Figure 3.18: Top view of the time-evolved droplet shape of two unequally sized coalescing droplets with volume ratio 4:1 (time in seconds).**

Even though the velocity of the coalescence is predicted faster in the simulation than in the real time experiments, still further evaluation of the velocity profile, perpendicular to the bridge over the centre axis of the droplet, can give important insight in the transport of the dye. In Figure 3.19, these velocity profiles for both simulations are shown for increasing time steps. For the droplets of equal volume, symmetry across the bridge can be seen with equal velocities on both sides of the bridge. At the bridge itself, the fluid velocity perpendicular to the bridge is zero. This is as expected, as the material flows near the bridge in this plane are flowing in opposite direction to feed the growth of the bridge. As the spherical shape is reached the material flows within the droplet also die out, as is shown in the bottom left figure. For the unequally sized droplets, the symmetry is non-existent. The material flow towards the bridge out of the smaller droplet is larger compared to the material flow out of the larger droplet. Comparable to the equally sized droplets, the material flows in the x-plane also change direction to the y-plane to feed the bridge. However, as the material flow from the smaller droplet is larger in the x-plane, especially near the substrate at $10^{-4}$ s, the area of low velocity is tilted slightly in the z-axis. This indicates that some fluid (including dye) is transported near the substrate from the small into the larger droplet, but also some fluid near the top of the droplet is transported towards the smaller droplet. The effect of the convective flows on the dye transport can be seen in the concentration profiles, $C/C_0=0.1$, at $10^{-4}$ s in Figure 3.20. For the equal volume ratio the dye has not been transported across the bridge as expected by the symmetry in the flows on either side of the bridge. For the droplets of unequal volume, this is also valid near the substrate and the top of the droplet. In between, at half the height of the droplet, the dye bulges slightly towards the larger droplet indicating a small contribution of convective transport of the dye. At $10^{-3}$ s, as the drop becomes spherical, the three-phase contact line of the smaller droplet moves towards the large droplet and a net material flow from the smaller in the larger droplet is calculated.

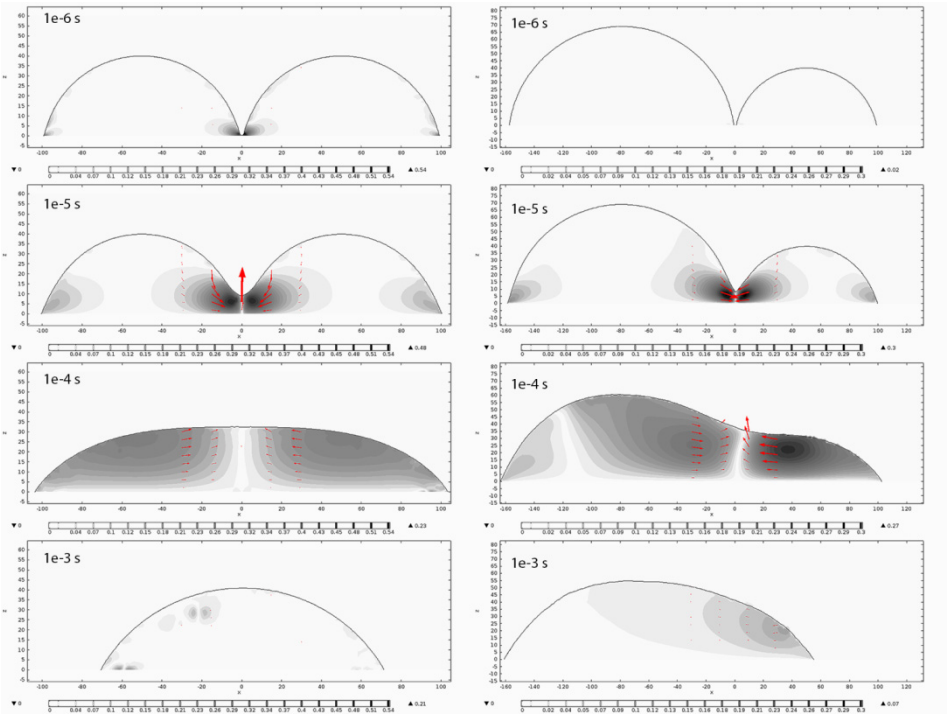


**Figure 3.19: Velocity profiles, perpendicular to the bridge, of coalescing droplets for vol. ratio 1:1 (left side) and vol. ratio 4:1 (right side). Darker contours indicate higher velocities of the fluid, arrows indicate direction and size of flow in xz-plane.**

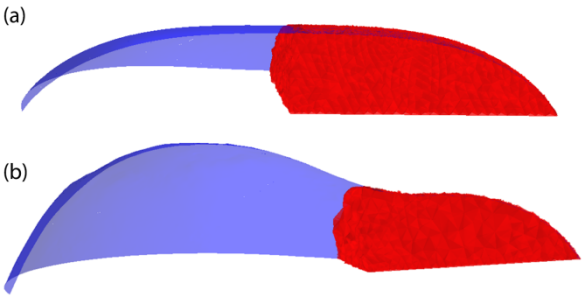


**Figure 3.20: Side view of concentration profile for $C/C_0=0.1$ at $10^{-4}$ s) droplet volume ratio 1:1, b) droplet volume ratio 4:1.**

As the numerical simulations start to diverge strongly from the experiments at $t>10^{-4}$ s, with the drops becoming spherical compared to being "pinned" in the experiments, an analogous evaluation of the dye transport over the full time range of the simulations is not

realistic. It is therefore decided to adapt the simulations by splitting them into two parts. The first part describes the time range up to $10^{-4}$ s, with both convective and diffusive flows present. The second part describes the time range from $10^{-4}$ s onwards. In this part, the droplet shape is "frozen" and the convective flows are set to zero, leaving only diffusive flows to remain present. The concentration profile within the droplet at $10^{-4}$ s is used as starting point in the second part of the simulation. The results of the two parts of the simulations are shown in Figure 3.21 and Figure 3.22 as a top view of the concentration ratio $C/C_0=0.1$.

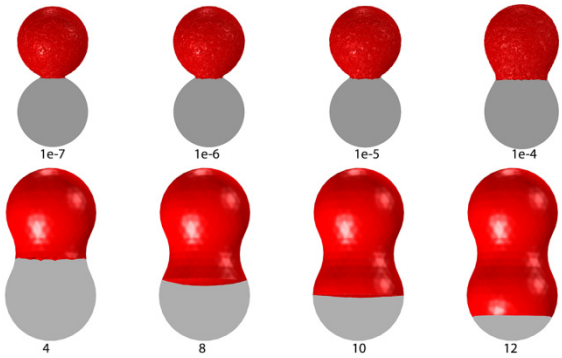


**Figure 3.21: Top view of droplet coalescence with 1:1 volume ratio. (Dark colour represents the position of the concentration ratio for $C/C_0=0.1$, light colour represents the drop contour, time in seconds).**

In Figure 3.21, the top four figures show the position of the concentration ratio for $C/C_0=0.1$ in the first part of the simulation with both convective and diffusive flows present. The bottom four images show the second part of the simulation with only diffusive flows present. As mentioned above, due to the symmetry over the bridge, the simulation predicts no dye transport across the bridge due to convective flows. At longer time periods, due to the concentration gradient of the dye over the bridge, diffusion takes place, transporting the dye across the bridge as can be seen in the bottom four figures. The numerical simulation follows the experimental observations reasonably well, with $C/C_0=0.1$ reaching the other side of the droplet after 14 s, compared to 20 s for the experiments.

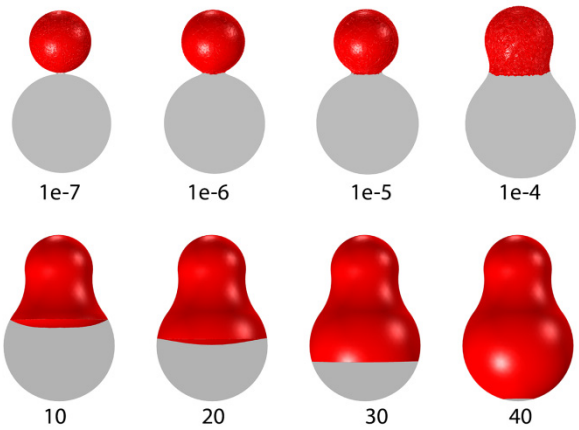


**Figure 3.22: Top view of droplet coalescence with 4:1 volume ratio. (Dark colour represents position of the concentration ratio for $C/C_0=0.1$, light colour represents the drop contour, time in seconds).**

Similarly to Figure 3.21, Figure 3.22 describes the numerical simulation of the position of the concentration ratio for $C/C_0=0.1$ for the volume ratio 4:1. Up to $10^{-4}$ s, with convective flows still present, the contribution of these flows is small but visible, resulting in a slight bulge of the position of the concentration ratio at $10^{-4}$ s. This effect was also seen in the experiments. With the absence of the convective flows, equal to the 1:1 volume ratio, diffusion becomes dominant due to the concentration gradient over the bridge. In time, the dye diffuse further into the large droplet with $C/C_0=0.1$ reaching the end of the large droplet after 42 s, compared to approx. 50 s for the experiments.

### *3.3.4 Conclusions*

Numerical simulations of the coalescence of two equally and unequally sized droplets were performed. The goal of these simulations was to verify the dye transport due to both convective and diffusive flows, and compare the results with the experimental work of paragraph 3.2. The numerical simulations were able to describe the droplet shape evolutions reasonably well for both volume ratios up to $10^{-4}$ s when compared to the experiments. The opening of the bridge, however, is predicted in the simulation approx. 10 times faster as compared to the experimental data. After $10^{-4}$ s, the droplet shape in the simulations diverges from the experiments as the droplets become spherical, whereas in the experiments, the drop shape stops changing. In order to follow the dye transport after $10^{-4}$ s, the simulations were split in to two parts based on the velocity profiles in the x-plane of the liquid within the droplet. The first part described the time range up to $10^{-4}$ s, with both convective and diffusive flows. The second part described the time range from $10^{-4}$ s up to 40 s, with only diffusive flows. Using this adaptation, the dye transport could be reasonably described in comparison with the experiments for both the equally and unequally sized droplets. Still, a single numerical simulation over the complete time range, which describes the droplet shape evolution correctly, was not obtained. Although, the droplet shape evolution in to a spherical drop is an expected calculation from the physics in the laminar two phase model used, it is unlike our experiments of small coalescing droplets in the inertial regime. Further investigation in revising the physics models within Comsol is recommended.

## *3.4 References*


1. Liberski, A.R., J.T. Delaney Jr, and U.S. Schubert, *"One Cell– One Well": A New Approach to Inkjet Printing Single Cell Microarrays.* ACS combinatorial science, 2010. **13**(2): p. 190-195.
2. Smith, P.J. and A. Morrin, *Reactive inkjet printing.* Journal of Materials Chemistry, 2012. **22**(22): p. 10965-10970.
3. van Oosten, C.L., C.W. Bastiaansen, and D.J. Broer, *Printed artificial cilia from liquid-crystal network actuators modularly driven by light.* Nature materials, 2009. **8**(8): p. 677-682.
4. Eggers, J., J.R. Lister, and H.A. Stone, *Coalescence of liquid drops.* Journal of Fluid Mechanics, 1999. **401**: p. 293-310.
5. Duchemin, L., J. Eggers, and C. Josserand, *Inviscid coalescence of drops.* Journal of Fluid Mechanics, 2003. **487**(1): p. 167-178.
6. Anilkumar, A.V., C.P. Lee, and T.G. Wang, *Surface-tension-induced mixing following coalescence of initially stationary drops.* Physics of Fluids A: Fluid Dynamics, 1991. **3**(11): p. 2587-2591.
7. Aarts, D. and H.N.W. Lekkerkerker, *Droplet coalescence: drainage, film rupture and neck growth in ultralow interfacial tension systems.* Journal of Fluid Mechanics, 2008. **606**: p. 275-294.
8. Menchaca-Rocha, A., F. Huidobro, A. Martinez-Davalos, K. Michaelian, A. Perez, V. Rodriguez, and N. CÂRjan, *Coalescence and fragmentation of colliding mercury drops.* Journal of Fluid Mechanics, 1997. **346**: p. 291-318.
9. Andrieu, C., D.A. Beysens, V.S. Nikolayev, and Y. Pomeau, *Coalescence of sessile drops.* Journal of Fluid Mechanics, 2002. **453**: p. 427-438.
10. Mingming, W., T. Cubaud, and H. Chih-Ming, *Scaling law in liquid drop coalescence driven by surface tension.* Physics of Fluids, 2004. **16**(7): p. L51-L54.
11. Ristenpart, W.D., P. McCalla, R. Roy, and H. Stone, *Coalescence of spreading droplets on a wettable substrate.* Physical review letters, 2006. **97**(6): p. 64501.
12. Lee, M.W., D.K. Kang, S.S. Yoon, and A.L. Yarin, *Coalescence of Two Drops on Partially Wettable Substrates.* Langmuir, 2012. **28**(8): p. 3791-3798.
13. Eddi, A., K. Winkels, and J. Snoeijer, *How geometry determines the coalescence of low-viscosity drops.* arXiv preprint arXiv:1307.7475, 2013.
14. Castrejón-Pita, J., E. Betton, K. Kubiak, M. Wilson, and I. Hutchings, *The dynamics of the impact and coalescence of droplets on a solid surface.* Biomicrofluidics, 2011. **5**(1): p. 014112.
15. Yang, X., V.H. Chhasatia, J. Shah, and Y. Sun, *Coalescence, evaporation and particle deposition of consecutively printed colloidal drops.* Soft Matter, 2012. **8**(35): p. 9205-9213.
16. Verdier, C. and M. Brizard, *Understanding droplet coalescence and its use to estimate interfacial tension.* Rheologica acta, 2002. **41**(6): p. 514-523.

17. Castrejón-Pita, J., K. Kubiak, A. Castrejón-Pita, M. Wilson, and I. Hutchings, *Mixing and internal dynamics of droplets impacting and coalescing on a solid surface.* Physical Review E, 2013. **88**(2): p. 023023.
18. Fathi, S. and P. Dickens, *Challenges in drop-on-drop deposition of reactive molten nylon materials for additive manufacturing.* Journal of Materials Processing Technology, 2013. **213**(1): p. 84-93.
19. Borcia, R. and M. Bestehorn, *On the coalescence of sessile drops with miscible liquids.* The European Physical Journal E: Soft Matter and Biological Physics, 2011. **34**(8): p. 1-9.
20. Laplace, P.S., *Traite de Mechanique Celeste* Vol. 4 Supplements au Livre X. 1805, Gauthier-Villars, Paris.
21. Young, T., *An Essay on the Cohesion of Fluids.* Philosophical Transactions of the Royal Society of London, 1805. **95**: p. 65-87.
22. Dongen, M.H.A., A. Loon, R.J. Vrancken, J.P.C. Bernards, and J.F. Dijksman, *UV-mediated coalescence and mixing of inkjet printed drops.* Experiments in Fluids, 2014. **55**(5): p. 1-9.
23. Dongen, M.H.A.v., A.v. Loon, H.J. Halewijn, and J.P.C. Bernards. *Simulation of the coalescence and subsequent mixing of inkjet printed droplets*. in *2013 Comsol Conference*. 2013. Rotterdam: Comsol.
24. Zahedi, S., *Numerical methods for fluid interface problems*. 2011, Umeå University.
25. Batchelor, G.K., *An introduction to fluid dynamics*. 2000: Cambridge university press.
26. Aarts, D., H.N.W. Lekkerkerker, H. Guo, G.H. Wegdam, and D. Bonn, *Hydrodynamics of Droplet Coalescence.* Physical Review Letters, 2005. **95**(16): p. 164503.
27. Tanner, L.H., *The spreading of silicone oil drops on horizontal surfaces.* J. Phys. D: Appl. Phys, 1979. **12**.
28. Vig, J. and J. LeBus, *UV/ozone cleaning of surfaces.* Parts, Hybrids, and Packaging, IEEE Transactions on, 1976. **12**(4): p. 365-370.
29. Jun, N., X. Ming, and H. Yong, *Research Progress in UV Curing Coatings.* Paint & Coatings Industry, 2009: p. 12.
30. Poulis, J., J. Cool, and E. Logtenberg, *UV/ozone cleaning, a convenient alternative for high quality bonding preparation.* International journal of adhesion and adhesives, 1993. **13**(2): p. 89-96.
31. Fick, A., *V. On liquid diffusion.* The London, Edinburgh, and Dublin Philosophical Magazine and Journal of Science, 1855. **10**(63): p. 30-39.
32. Liu, D., P. Zhang, C.K. Law, and Y. Guo, *Collision dynamics and mixing of unequal-size droplets.* International Journal of Heat and Mass Transfer, 2013. **57**(1): p. 421-428.
33. Gelfgat, A.Y., A.L. Yarin, and P.Z. Bar-Yoseph, *Dean vortices-induced enhancement of mass transfer through an interface separating two immiscible liquids.* Physics of Fluids 2003. **15**(2): p. 330-347.

34. Comsol, *Comsol Multiphysics User Guide*. 2013: USA.
35. Lafaurie, B., C. Nardone, R. Scardovelli, S. Zaleski, and G. Zanetti, *Modelling merging and fragmentation in multiphase flows with SURFER.* Journal of Computational Physics, 1994. **113**(1): p. 134-147.
36. Olsson, E. and G. Kreiss, *A conservative level set method for two phase flow.* Journal of computational physics, 2005. **210**(1): p. 225-246.
37. Bird, R.B., W.E. Stewart, and E.N. Lightfoot, *Transport phenomena*. 1962: J. Wiley.

# 4 Applications of µPlasma patterning and inkjet printing

In chapter two the principles of µPlasma patterning were introduced. We showed that plasma treatment has a large effect on primarily the wetting behaviour of liquids on substrates like glass or plastics. We also showed that µPlasma patterning, with its ability to locally treat selected areas with plasma, is an interesting technology as a pre-processing tool in the production of potential applications. In chapter 3, inkjet printing was used as a tool to deposit droplets for studies in coalescence and mixing. Inkjet printing technology is capable of much more, and is used in industry for numerous applications. In this chapter, we will discuss some applications which were developed at the Expertise Centre of Thin Films and Functional Materials, part of the Fontys University of Applied Sciences.

## 4.1 Localized tailoring of Ink-Surface interactions

For several decades plasmas or electrical discharges are widely being used in a variety of industrial applications. Applications range from ozone generation, pollution control, lasers, lighting, flat large area displays and surface treatment. In recent years the use of dielectric barrier discharge plasmas made it possible to operate plasmas at atmospheric pressure in a controlled manner, thus creating the possibility to treat materials which cannot sustain heat or vacuum [1, 2]. Advances in DBD plasma technology have made it possible to treat entire polymer surfaces rapidly, continuously and uniformly. However, for patterned plasma treatment most current plasma technologies require masking techniques to achieve satisfactory resolutions. Exceptions are plasma jets or plasma pens, which scan the surface of the substrate and are capable of patterned plasma treatment with resolutions of approx. 1 cm in diameter. These are, however, relatively slow processes. µPlasma pattering combines digital printing technology with atmospheric plasma treatment. With the speed and accuracy of the inkjet printing platform, patterned plasma treatment with resolutions down to 300 µm, is possible without the use of masks [3-6]. Figure 4.1 shows an example of the maskless µPlasma patterning capabilities. DBD plasmas are characterized by the presence of a dielectrically insulating layer between two

metal electrodes in addition to a discharge gap. Atmospheric DBD plasma modifies the chemical structure of the top surface layer of a substrate to promote or demote adhesion or wetting, dependent on the plasma gas composition, without modifying the bulk layer. For instance the use of air as plasma gas functionalizes the substrate surface by incorporating oxygen containing groups on the surface. This increases the polar part of the surface energy of the substrate, thus improving the wettability creating a hydrophilic surface. By using silanized or fluorinated precursor materials in the plasma gas like e.g. hexamethyl-disiloxane (HMDSO) or perfluorohexane ($C_6F_{14}$), it is possible to deposit a hydrophobic layer on the surface [5, 7, 8]. Combining "standard" atmospheric air plasma treatment and precursor plasma treatment with the patterned plasma capabilities of µPlasma patterning offers the opportunity to develop new applications.

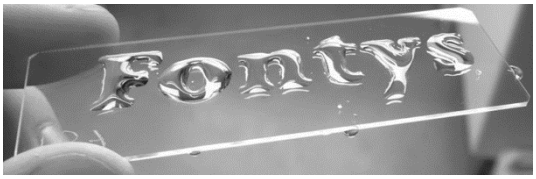


**Figure 4.1: Illustration of the maskless patterned µPlasma patterning technology. In this case, the logo of the Fontys University of Applied Sciences was printed on to a silanized hydrophobic glass slide to create a hydrophilic surface using nitrogen plasma. As the plasma treatment is not visible by eye, water was placed on the substrate to visualize the hydrophilic µPlasma treated area.**

Future applications for this technology can be found in the field of e.g. inkjet printing of functional materials, Lab-on-a-chip devices or microreactor engineering where localized tailoring of the surface can control the wetting behaviour of inks or other liquids. In this investigation we focus on the development of a Lab-on-a-chip device. A Lab-on-a-chip is a device capable of integrating one or more laboratory functions on to a single carrier material in the order of several millimetres to centimetres in size. Lab-on-a-chip technology is at the moment becoming increasingly important in healthcare. Lab-on-a-chip devices offer several advantages to current medical technologies, particularly as "point-of-care" applications in developing healthcare countries [9-11]. The basis for a Lab-on-chip is a carrier material of glass, ceramics, plastics or paper in which capillaries are created. These capillaries can be created by e.g. embossing, lithography, extrusion, or etching. Different shapes and sizes of the capillaries can assist in fluid handling by mixing fluids or transporting them to reactive sites. In this investigation, we will demonstrate that µPlasma patterning can be used as alternative method to create the capillaries for a Lab-on-a-chip device. It is not the intention to build a fully working Lab-on-a-chip device itself,

but to show the potential of µPlasma patterning to create micro channels capable of transporting fluids by capillary forces only.

### *4.1.1 Experimental*

For the construction of the Lab-on-a-chip capillaries standard microscopic glass slides (76x26 $mm^2$) were used. Because of the small contact angle of water on glass, i.e. less than 5 degrees, the glass slides were pre-treated with dodecyl-thiclorosilane (Sigma Aldrich), in order to make the glass hydrophobic. First the glass was thoroughly cleaned by rinsing with deionised water, and n-propanol before being dried in air. Next, the glass slides were placed in a solution of 0.001 M dodecyl-thiclorosilane in toluene at $3^0$C for 30 minutes under a nitrogen atmosphere to deposit a monolayer of dodecyl-thiclorosilane (DTS) on the glass slide. After coating, the glass slides were sequentially rinsed with toluene, ethanol and deionized water and dried with nitrogen. The hydrophobic nature of the glass slides was checked by measuring the water contact angle measurement using a Dataphysics OCA-30 contact angle measurement device. Contact angles over $100^O$ were measured for the treated glass slides. Comparable to the experiments in chapter 2.5, using µPlasma patterning, structures were printed on the DTS-treated glass slides. The plasma from the µPlasma printer selectively removes the DTS, exposing the original glass surface. Even though multiple structures were printed, in Figure 4.2 two examples of printed structures are shown. The structures were printed at 20 mm/s at 4.5 kV and 50 µm print height between print head and glass substrate with 90 dpi. A nitrogen flow of 200 ml/min at ambient pressure (99.999% Praxair) was used as plasma gas.

To create the hydrophilic capillaries, two glass slides were µPlasma patterned upon using, among others the mirror image structures from Figure 4.2. After printing, the capillaries were formed by placing the glass slides on top of each other. In between the glass slides, adhesive tape (3M Scotch tape, thickness 0.10 mm) is placed to create a space between the slides. To test the functionality of the capillary design, water coloured with a dye for better visual contrast was positioned at the opening of the design. Under capillary force the water enters the reactor and fills the channel. The progress of the liquid flow through the capillary is filmed and analysed.

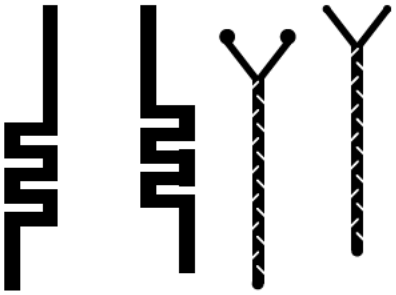

(a) (b)

**Figure 4.2. Two examples of µPlasma printed structures. (a) 3mm wide meandering line (b) dual inlet structure for two fluids (3 mm wide) with obstructions (1 mm wide) to enhance local mixing. Two mirror images were printed for the top and bottom side of the capillary.**

## *4.1.2 Results and discussion*

Figure 4.3 shows the top and bottom glass slides for the two designs presented above. For clarity the hydrophilic tracks are visualized with steam after µPlasma patterning. Water droplets form on the hydrophobic area of the glass slides, while on the plasma printed reactor design the water droplets fully wet leaving a clear surface, thus showing the printed design. On the design of Figure 4.3b, the hydrophobic obstructions are clearly visible. This shows that narrow tracks with high difference in wettability are obtainable through µPlasma patterning.

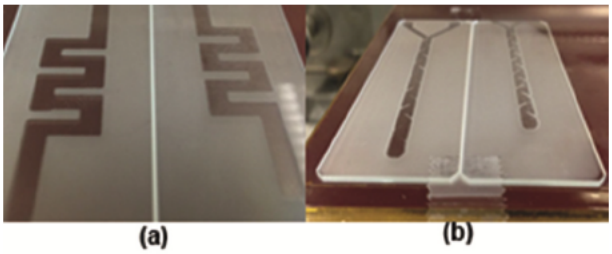


**Figure 4.3: Top and bottom of the two designs from Figure 4.2 directly after printing. For clarity the hydrophilic tracks are visualized with steam.**

After µPlasma patterning the glass slides with the two designs were placed on top of each other, 0.1 mm thick scotch tape was used as spacer between the slides to create a gap. Droplets of coloured water, for better visual contrast, were placed at the entrance of the designs. Under capillary pressure, the water is transported through the hydrophilic

channel. The large difference in surface energy between the DTS-layer and the µPlasma treated channel prevents the water to exit the channel. In Figure 4.4, the coloured water flowing through the printed channels can be seen. In Figure 4.4b, Water with two differently coloured dyes was used to show the mixing along the length of the design from Figure 4.2b. Due to the hydrophobic obstructions on the top and bottom of the capillary, the flow of the water is slightly restricted and mixing along the length is enhanced.

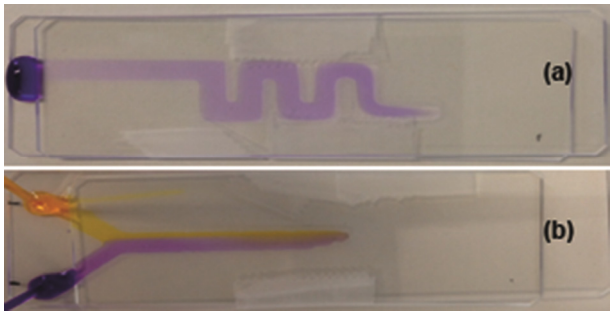


**Figure 4.4: Droplets of coloured water entering the two closed designs from Figure 4.2 (a) line structure, (b) mixer with dual inlet and hydrophobic obstructions.**

To investigate the quality of the capillary, the filling of the line design from Figure 4.2 was used to analyse the velocity of the water within the capillary and compared to the Lucas -Washburn equation [12]:

$$x^2 = \frac{\gamma \cdot D_H}{4 \cdot \eta} \cdot t \qquad (4.1)$$

In the equation, $x$ is the distance the water has entered the capillary (m), $\gamma$ the surface tension of water (72.8 mN/m), $\eta$ the viscosity of water (1 mPa·s) and $t$ the time (s). For the hydraulic diameter $D_H$, the dimensions of 3x0.10 mm$^2$ for the capillary are used, making $D_H$=0.192 mm and the constant $a = \gamma \cdot D_H / 4 \cdot \eta = 35$ cm$^2$/s. Figure 4.5 shows the result of the video analysis (filmed at 25 fps). Each measurement represents a single frame. After 2.2 seconds the capillary is completely filled. Fitting the experimental results according to (4.1) results in a constant of *a=38* cm$^2$/s and an adjusted R-square of 0.9975. From the Lucas-Washburn equation, the constant was calculated at *a=35* cm$^2$/s. As the µPlasma patterning setup in reality produces wider tracks than defined by the bitmap, as described in chapter 2.5, the hydraulic diameter in the Lucas-Washburn equation is underestimated. Taking this into account, the experiments show good agreement with equation (4.1).

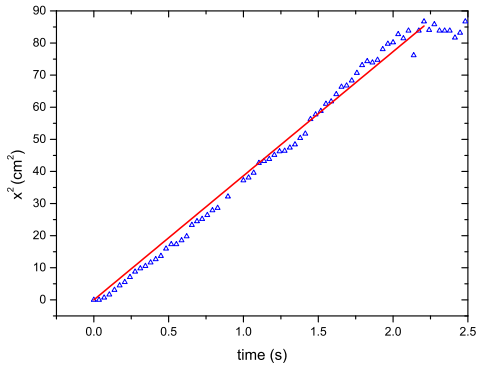


**Figure 4.5: Squared penetrated distance of liquid versus time for the meandering line. (△) experimental data, linear fit equals: $x^2=38 \cdot t\ cm^2$ with $R^2=0.9975$.**

## *4.1.3 Conclusions*

Overall, this shows that µPlasma patterning can be used to create hydrophilic tracks in between two hydrophobic surfaces. To work as capillary, the plasma printed tracks do not have to be closed on all sides, as the steep gradient in wetting between the printed track and surrounding area prevents leakage out of the printed tracks.

## *4.2 Radio Frequency Identification (RFID) tag*

In the packaging and transport industry, staying on top of the supply streams is of upmost importance to stay competitive in the market. Monitoring has to be efficient, quick and easily performed. Currently, barcode technology is the most used system worldwide as it is very cheap and easy to use. The main disadvantage of the barcode system is that it requires a line of sight to operate, which can decrease the efficiency and makes the equipment needed more complicated. With Radio Frequency Identification (RFID), no line of sight is required to obtain information from the supply streams, increasing both speed and efficiency [13]. Also, the embedded information in the RFID tag adds increased functionality to the products. Today, RFID tags are still more expensive when compared to barcodes, but are being used increasingly more, as new technologies arise to produce RFID tags in high amounts, lowering production costs. RFID is also increasing its market share by opening new markets like healthcare or finance. RFID technology consists of an RFID-antenna connected to an integrated circuit with embedded software present. RFID-tags can either be passive or active, referring to the method of operation. Active tags are powered continuously by a local power source, e.g. a battery. They have a typical emitting range of several hundred meters. Passive tags have no local power source, power in the integrated circuit is generated in the antenna by electromagnetic induction. As enough power is generated, the microprocessor will act as a transponder, emitting radio waves through the antenna. There are different kinds of passive tag/reader setups which operate in their own frequency ranges [14]. Ultra high frequency (UHF) tags work at 865-868 MHz in Europe or at 902-928 MHz in North America. They have a working range of 6-12 meters [15]. The range of the tag is not only determined by the frequency and thus the length of the antenna, but also by its ability to deliver the energy of the electromagnetic field to the integrated circuit. At UHF frequencies, the simplest geometry is a dipole antenna. Other more complex geometries are possible, but require more elaborate manufacturing and therefore higher production costs with only a marginal gain in omnidirectional reading ability. The energy transfer, from the electromagnetic induction fields via the antenna to the integrated circuit, is most efficient at the resonance frequency $f_0$. The relationship between the resonance frequency and length of the antenna is described by $f_0 = c / \lambda_0$ with c the speed of light and the wavelength at resonance $\lambda_o$, which equals the length of the antenna *l* times integer *n* ( $\lambda_0 = n \cdot l$ ). For tags operating in the UHF-band, the length of the antenna with *n=2* equals 16.4 cm. Optimal power output of the tag is not only dependent on the length of the antenna, but also on the impedance *Z* of the integrated circuit and attached antenna [16]. In Figure 4.6, the equivalent circuit of a RFID-tag with integrated circuit with

antenna is shown. The potential $V_A$ supplied by the antenna with impedance $Z_A$ delivers power to the integrated circuit $P_{IC}$. This power, in turn will drive the IC generating a voltage $V_{IC}$ and current $i$ to be used for transmission.

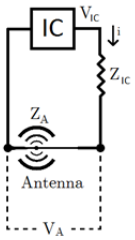


**Figure 4.6: The equivalent circuit of the interaction between the circuit and the attached antenna.**

In equation (4.2) the relationship between the generated power, antenna voltage and impedance of the antenna and integrated circuit is given. Equation (4.2) shows that if $Z_A$ is much larger than $Z_{IC}$, the power $P_{IC}$ delivered to the IC will be low and if $Z_A$ is much smaller than $Z_{IC}$ the delivered power will also be diminished. The maximum power output is reached when the impedances of the antenna and integrated circuit are perfectly matched with $Z_A=Z^*_{IC}$.

$$P_{IC} = V_{IC} \cdot i = \frac{V_A^{\,2} \cdot Z_{IC}}{\left(Z_A + Z_{IC}\right)^2} \tag{4.2}$$

The goal of this study is to develop a UHF-RFID tag which can be read without contact, or near contact. The integrated circuit used is a NXP TSSOP8 IC rated at $Z_{IC}$*= 16-148j* Ω at 915 MHz and *26-j160* Ω at 865-868 MHz [17, 18]. The antenna of the RFID tag will be inkjet-printed on paper using silver nanoparticle ink from Suntronics. For the tag to be able to function optimally, the design of the antenna needs to have an impedance of *26+j160* Ω for optimal performance. Different designs of the antenna will be numerically evaluated using Comsol Multiphysics. The best candidates will be inkjet printed and tested in combination with the integrated circuit as a working RFID tag.

## 4.2.1 Experimental

### Numerical simulations

The finite element software package Comsol Multiphysics is used to simulate the behaviour of antenna geometries. The "electromagnetic waves, frequency module" is used to describe the physics of the antenna. The IC is simulated as a lumped port. The effect of the antenna at a distance is simulated using a far-field domain. By changing the resonance frequency $f_0$ at constant voltage ($V_{IC}$=*1 V)* over the shortened port boundary, the transmission range of the antenna can be calculated. Different geometries of antennas are tested. The length of the antenna is 16.4 cm. The thickness of the antenna is chosen at 100 µm, as this is the minimum size for which it is still possible to reliably mesh the geometry of the antenna. The substrate is not simulated. Figure 4.7 shows an example of the geometry of the simulation of a shortened meandering dipole antenna.

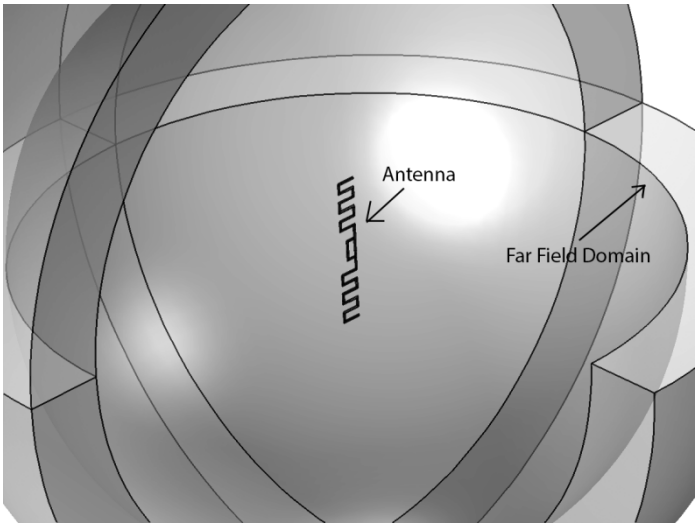


**Figure 4.7: Geometry of a shortened meandering antenna simulated in Comsol Multiphysics. Part of the far-field domain sphere is hidden, to be able to view the antenna.**

### RFID tag assembly

Selected geometries, optimised in Comsol Multiphysics, were inkjet printed with 20 wt% Ag-nanoparticle ink (Suntronics). Four layers of the silver ink were printed at 900 dpi on 220 gr/m$^2$ photo paper (Epson) using a Roth & Rau LP50 inkjet printer equipped with a

Konica Minolta 512 print head. After printing, the antennas were sintered for 60 minutes in an oven at $125^0$C. The TSSOP8 integrated circuit (NXP) was connected to the antenna using conductive epoxy resin (Ritelock SL65). A slight amount of toluene was added to the epoxy resin to lower the viscosity for better manageability. The antenna with connected IC was dried at $90^0$C for 90 minutes in order to evaporate the toluene and increase the conductivity of the resin.

### *Evaluation of the constructed RFID tags*

The resistance of the antennas was measured with a Fluke-37 multimeter over a distance of 4 cm. Layer thickness measurements on the antenna were performed by an Ambios XP1 profilometer. The antennas with integrated circuits were tested by reading the tag using a USB RFID-reader EVO and software package (IdTRONIC) supplied with the USB-reader [19]. This reader has an operating range of 830 to 950 MHz. Both distance vs readability measurements as well as frequency response measurements were performed using the IdTRONIC software.

## *4.2.2 Results and Discussion*

For best performance of the antenna, its impedance needs to be the conjugate of the impedance of the integrated circuit, i.e. $Z_A=16+148j\ \Omega$ or $Z_A=26+160j\ \Omega$ in North America and Europe, respectively. Normally, the IC would be constructed around an antenna, however in our case, as the IC was preselected, the antenna design needed to be optimised. Consequently, simulations on the performance of a series of antenna designs were performed. The goal of these simulations was to find an optimal geometry and impedance, as to maximize the reading distance. In the simulations a voltage ($V_{IC}$) of 1 V is used to power the antenna. Impedance ($Z_A$) is calculated over the connection points of the lumped port. The maximum reading distances of the antennas are derived from polar plots of the field strength. This is an indicative value for comparison only, as the real voltage generated by the antenna in the presence of a transmitter is not known. Also the thickness of the simulated antenna was 100 µm, which is much larger when compared to the inkjet printed average layer thickness of approx. 2 µm. Table 4.1 shows an overview of the simulated antenna designs with their derived impedance and maximum reading distance. Although none of the simulated impedances equal the optimal impedance needed for best performance, based on the calculated impedance at 915 MHz, the shortened dipole, shortened bowtie or shortened square look most promising.

**Table 4.1: Impedance ($Z_{IC}$) and reading distances for the simulated antenna designs for $V_{IC}$=1 V [20, 21].**

| Antenna design | Impedance $Z_A$ at 915 MHz (Ω) | Maximum reading distance (m) |
|---|---|---|
| **Dipole** | *120+102j* | 1.2 |
| **Dipole (shortened)** | *29+290j* | 0.6 |
| **Rectangular (shortened)** | *97+50j* | 1.0 |
| **Bowtie** | *114+84j* | 1.1 |
| **bowtie (shortened)** | *20+136j* | 1.75 |
| **Meandering** | *51 – 488j* | 0.01 |
| **meandering (shortened)** | *12 – 112j* | 0.01 |
| **Square** | 13 – 145j | 0.10 |
| **Square (shortened)** | 10 + 144j | 1.05 |

To test the functionality of the different antennas, the shortened versions of the dipole, rectangular and bowtie antennas were inkjet printed as most promising candidates. Also the shortened meandering antenna was inkjet printed as a least promising candidate for comparison. After printing and sintering, the IC was connected and the completed antennas were read with the UHF-reader. A resistance *R* of 0.9 Ω/cm was measured for the Ag-nanoparticle ink, printed at 900 dpi with four layers after sintering for 1 hour at 125$^0$C on Epson photo paper. On average, the layer thickness of the printed antennas was measured to be 2 µm (Ambios X1 profilometer). Although lower values of resistance could possibly be reached, this value is low enough to be usable in this application. Figure 4.8 shows examples of inkjet printed antenna designs of the dipole, meandering and bowtie antenna, without the integrated circuit. The integrated circuit is placed over the opening in the silver tracks, as is shown in Figure 4.9 for the meandering antenna. A DC resistance measurement was performed to ensure the contact was conductive.

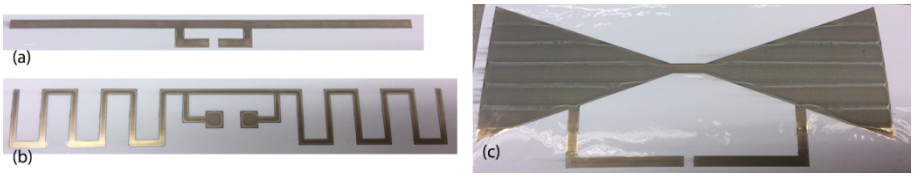


**Figure 4.8: Antenna designs without IC (a) shortened dipole antenna, (b) shortened meandering antenna, (c) shortened bowtie antenna. Inkjet printed at 900 dpi, 4 layers on Epson photo paper.**

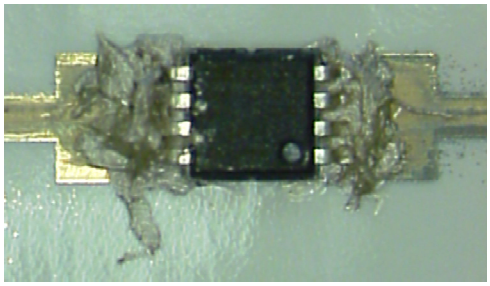

**Figure 4.9: Detail of IC connected to the antenna.**

Upon placing the completed RFID-tags near the RFID-reader, all printed antenna designs showed to be readable and writable. The shortened dipole, meandering and bowtie design functioned up to 1 m away, the rectangular design functioned up to approx. 5-10 cm from the reader. Several tags were found to stop functioning after some time, probably due to handling issues, like excessive bending. Slight to moderate bending did not influence the working ability.

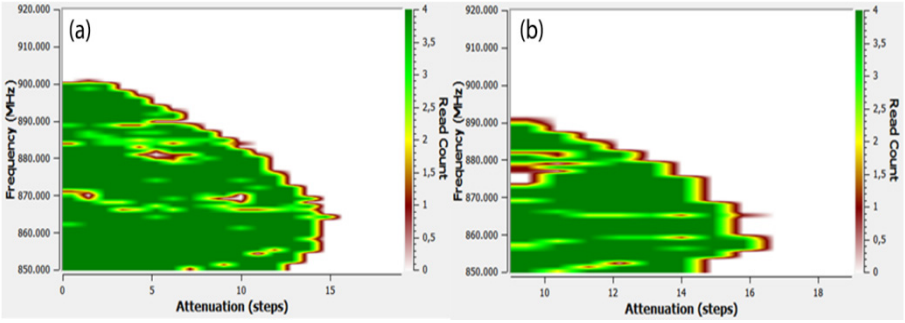


**Figure 4.10: Frequency response and read count vs attenuation of the RFID-antennas for (a) shortened dipole antenna and (b) shortened meandering antenna.**

At the design frequencies of European and United States regulations, the antenna designs are tested on their efficiency over the complete frequency range, as shown in Figure 4.10 for the dipole and meandering antenna. At a set frequency, the reader will attenuate the transmitted power from maximum to zero. If the power of the reader is high enough, the tag will start broadcasting and the reader will count the number of times the IC-code is received. The number of counts is an indication of the range of the tag in relation to the operation frequency. For both tested antennas, the optimal operating frequency is in between 860-865 MHz. No response is seen in the range of 902-920 MHz.

Consequently, the tags can potentially only be used in a European setting, and are not usable within North America.

### *4.2.3 Conclusions and recommendations*

Functional RFID-tags on paper were created via inkjet printing. The optimal operating frequency of the tags is in the range of 860-865 MHz, making them usable for the European market, although the working range of 1 m needs further improvement. Based on the impedance and range calculations from the simulated designs, it was anticipated that the dipole, bowtie and rectangle antenna design would achieve better functionality when compared to the meandering design. However, this could not be confirmed with the printed design, as the meandering design showed a similar working range as compared to the other designs. Still, modelling of the different tags resulted in a more rigorous understanding of the modifications to the simple dipole antenna geometry to incorporate an inductance and a capacitance. Impedance measurements of the printed tags should be performed, in order to better compare the simulated models to the printed tags.

## *4.3 The Development of a Flexible Gas Sensing Chemresistor*

Chemical sensors are at forefront of the detection of gases in the environment we live in. A large number of gas sensors uses conducting polymers because of the great design flexibility [22]. Conducting polymers have many improved characteristics compared to commercially available sensors based on metal oxides that operate at high temperatures. Some of these characteristics are: shorter response times and high sensitivity with both factors being applicable at room temperature. Also, the ease of synthesis by chemical or electrochemical processes and the ease in modifying their molecular chain structure make conducting polymers interesting. Their good mechanical properties facilitate the production of sensors. The most common type of chemical sensor is the chemresistor. A chemresistor consists out of two electrodes connected to a measuring device and a conductive sensing layer connecting the two electrodes. The sensing layer changes in resistance in the presence of a specific gas [23, 24].

In this study, we will show the development of a polyaniline (PANi) based chemresistor sensitive to water and ethanol vapour. PANi is known to be sensitive for a multitude of gases like: NO, $H_2S$, $SO_2$, $NH_3$, alcohols or water vapour. Selectivity can be obtained by doping PANi with e.g. camphor-sulphonic acids [25-29]. Lizarraga et al. showed that PANi layers change in volume when brought into contact with an electrolyte [30]. The volume change in PANi layers can be attributed to the interactions of small chain alcohols such as ethanol gas or water vapour with the amine bonds in the PANi. Here the design of the chemresistor using polyemeraldine salt is chosen. Polyemeraldine is PANi in the most conductive oxidation state, with a conductivity of approx. 15 S/cm. The polyemeraldine salt will be synthesized in house from aniline hydrochloride and ammonium persulphate according to the following chemical reaction:

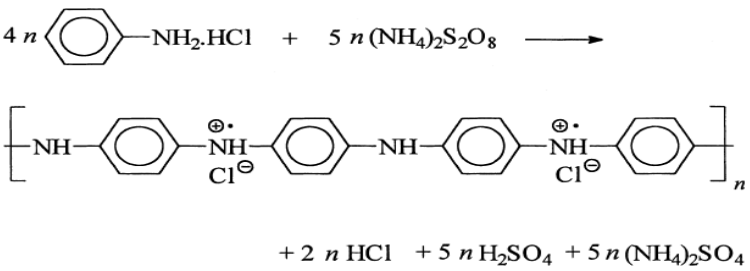


**Figure 4.11: Synthesis of polyemeraldine salt [25].**

The gas sensor will be constructed by inkjet printing of the silver electrodes, followed by hand coating of the polyemeraldine layer on top of the electrodes. Polycarbonate will

be used as substrate to create a flexible sensor. A schematic drawing of the electrodes of the sensor is shown in Figure 4.12. The comb-like structure consists of 8 interlocking fingers each, separated by 500 µm. The radius of the comb is 20 mm.

**Figure 4.12: Schematic drawing of the electrodes of the chemresistor (Dimensions after printing 4.5x 2.0 $cm^2$).**

## *4.3.1 Experimental*

### *Sensor construction*

Polyemeraldine salt was synthesized by dissolving 2.59 g of aniline hydrochloride (Sigma Aldrich) and 5.71 g ammonium persulphate (Sigma Aldrich) in 50 ml of deionized water each. Both solutions were kept at room temperature for 1 hour, then briefly mixed en left to polymerize for two hours. After polymerisation, the solution is filtered and washed with hydrochloric acid (37% in water, Sigma Aldrich). The filtered polyemeraldine salt is left to dry at room temperature. In approx. 7 days of drying at room temperature, the viscosity reaches approx. 0.5 Pa·s and is ready to be used. The silver electrodes were inkjet printed with Suntronic Jet Silver U5603 nanoparticle ink on a Roth & Rau Pixdro LP50 Inkjet printer with a Spectra SM-128 print head. The comb-like pattern from Figure 4.12 was inkjet printed at 450 dpi on 125 µm thick polycarbonate film (Goodfellow) and sintered at $150^0$C in an oven for 1 hour to achieve a sheet resistance of 3.0 ± 0.5 Ω/□ (Jandell four point probe). The sensor was coated by hand with a 30 µm thin layer of the polyemeraldine salt on the comb part of the electrodes. The completed sensors were stored at room temperature (~$22^o$C) at a relative humidity of 20%.

### *Sensor Analysis*

For analysis, the sensor was placed in an electrical circuit and connected in series to an AC-source (AFG 3021B, 1 kHz, 1 V). Both electric current and voltage over the sensor were measured with a Fluke 8846A multimeter. Gas flow and gas composition over the sensor was regulated by splitting dry compressed air (6 bar) into two conduits. One conduit was fed directly to the measurement chamber (volume≈0.5 l), the other conduit was fed to a gas bubbler filled with either ethanol or deionized water, saturating the gas

flow, before entering the measurement chamber. Gas flow through both conduits was regulated via two flowmeters (Bronkhorst) to a combined maximum flowrate of 500 ml/min. The flowrate of the two flowmeters was changed in steps of 20% to test the sensitivity of the sensor to water or ethanol present in the gas flow. A schematic view of both the electrical circuit and experimental setup is given in Figure 4.13.

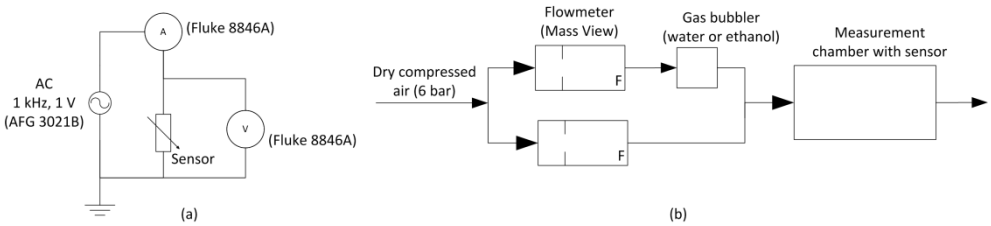


**Figure 4.13: (a) electrical circuit and (b) experimental setup for the gas sensor measurements.**

## *4.3.2 Results and Discussion*

Figure 4.14 shows an uncompleted and completed example of the constructed gas sensor. The PANi is hand coated onto the silver comb structure.

**Figure 4.14: gas sensor (a) before adding PANi layer, (b) with PANi layer. The area outside the comb structure is covered with scotch tape (3M).**

The resistance of the sensors as a function of time was measured for sensors stored at 20%RH and 50 %RH. The time dependence is shown in Figure 4.15. The resistance, after 24 hrs of drying, varies from 80-225 kΩ. No relationship between the thickness of the PANi-layers or relative humidity and the initial resistance was found. This variance in resistance is potentially due to differences in viscosity, i.e. drying time, of the PANi before application onto the electrodes, but was not further investigated. For all sensors stored at 20%RH and 50% the resistance decreases in time.

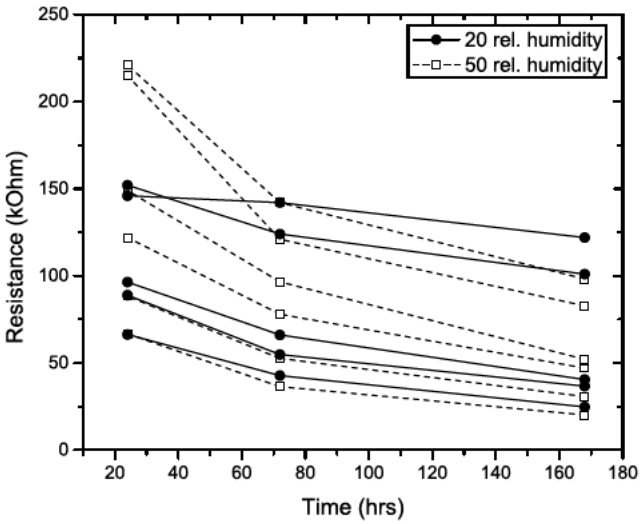


**Figure 4.15: Start resistance of sensors stored at 20%RH (lines) and 50%RH (dotted lines).**

The resistance of the sensors stored at 50%RH decreases with 50±20% in the time period from 1 to 7 days. In comparison, the sensors stored at 20%RH show a decrease of 37±4% in resistance in the same time period. Apparently, the higher humidity level of 50%RH delays the drying of the sensors, retaining more moisture within. According to Kahol et al. and Tobolkova et al., this increases the conductive effectiveness of the PANi, thus further lowering the resistance over time [29, 31]. The effectiveness of the gas sensor on detecting ethanol or humidity in air is tested by mixing saturated ethanol or water vapour with dry air at different flow ratios. In between each increase in flow ratio, the chamber containing the sensor is flushed with dry air for 10 min. In Figure 4.16, an example of such an experiment is depicted. The sensor is highly sensitive in detecting ethanol in the gas flow, as a sharp decrease in resistance can be seen as ethanol vapour is added to the gas flow. Although it is expected that the sensor would react almost instantaneous, a 3 second delay is seen in the resistance after changing flow ratios. This delay is caused by the response time of the measurement setup, as the gas conduit and measurement chamber needs to filled with (some of) the changed gas composition before the sensor can react. Upon flushing the measurement chamber with dry air, the resistance returns to its original value, also with some delay due to the residence time of the gas conduit and measurement chamber. Similar curves were measured for water vapour.

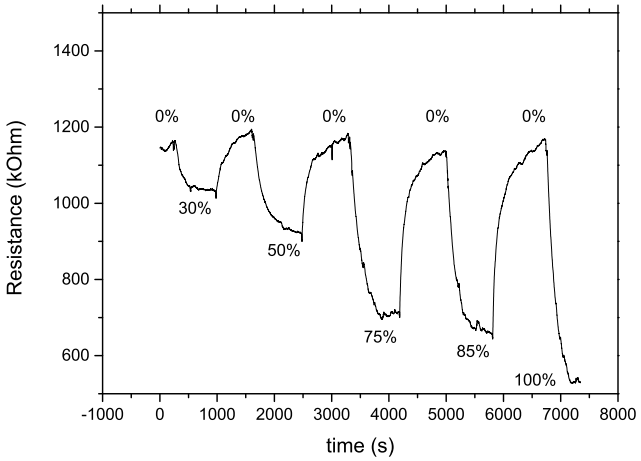


**Figure 4.16: Resistance of the gas sensor for different flow ratios of saturated ethanol vapour and dry air (total flow rate is 500 ml/min). The percentages indicate flow ratio.**

The change in resistance for both ethanol and water vapour was measured for different flow ratios and plotted in Figure 4.17. The gas sensor shows a similar trend in the change in resistance for both water and ethanol. The experimental data were exponentially fitted according to $R/R_o = e^{-Ax}$, with *A=0.038* and *A=0.045* for ethanol and water, respectively. For both vapours an adjusted R-square equal to 0.99 was derived.

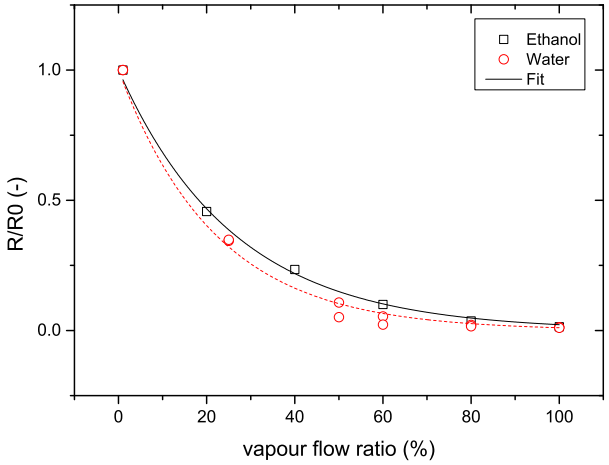


**Figure 4.17: Change in resistance of water and ethanol vapour as a function of the flow ratio of vapour saturated flow and dry air for a total flow 500 ml/min. Both curves were fitted according to $R/R_o = e^{-Ax}$ with *A=0.038* and *0.045* for ethanol and water, respectively.**

Surprisingly, the sensitivity of the PANi chemresistor to water and ethanol vapour is almost equal. This high sensitivity of the PANi for both ethanol and water can potentially create confusing results in “open-to-air” measurements situations if ethanol vapour needs to be detected. Clear consideration of the effect of the humidity on the measurement needs to be taken into account.

### *4.3.3 Conclusions*

In this paragraph, we demonstrated the ease of manufacturing of a polyaniline based chemresistor using inkjet printing of the silver electrodes and coating by hand of the PANi layer. Storage of the sensors in 20%RH and 50%RH, showed a decrease in resistance of the sensors in the time period from 24 to 168 hrs. by 37% to 50%, respectively. The initial resistance of the PANi layer after 24 hrs. of drying showed a large variance, potentially due to differences in viscosity of the PANi-layer upon application. The chemresistor showed to be highly sensitive to concentration changes in both ethanol and water vapour flows. The selectivity of the chemresistor in detecting ethanol or water vapour is low, as the chemresistor responds equally profound to both gases. Humidity has to be taken into account when measuring ethanol in “open-to-air” situations.

## 4.4 References


1. Kogelschatz, U., *Dielectric-barrier discharges: Their history, discharge physics, and industrial applications.* Plasma chemistry and plasma processing, 2003. **23**(1): p. 1-46.
2. Tendero, C., C. Tixier, P. Tristant, J. Desmaison, and P. Leprince, *Atmospheric pressure plasmas: A review.* Spectrochimica Acta Part B: Atomic Spectroscopy, 2006. **61**(1): p. 2-30.
3. M.H.A. van Dongen, E. Nieuwenhuis, L. Verbraeken, R. Verkuijlen, P. Ketelaars, and J.P.C. Bernards, *Digital printing of µPlasmas to selectively improve wetting behavior of functional inks for printed electronics*, in *NIP 28 and Digital Fabrication 2012*. 2012, IS&T: Quebec City, Canada. p. 436-439.
4. Brok, W., A. Stevens, E. Bos, T. Huiskamp, N.v. Hijningen, and H.d. Haan, *The potential of plasma printing.* Mikroniek, 2011(1): p. 32-39.
5. Dongen, M.H.A.v., R.O.F. Verkuijlen, and J.P.C. Bernards. *Inkjet Printing of Functional Materials on Selectively Plasma Treated Surfaces*. in *Proc. LOPE-C*. 2011. Frankfurt.
6. Huiskamp, T., W. Brok, A. Stevens, E. van Heesch, and A. Pemen, *Maskless Patterning by Pulsed-Power Plasma Printing.* Plasma Science, IEEE Transactions on, 2012. **40**(7): p. 1913-1925.
7. van Dongen, M., R. Verkuijlen, R. Aben, and J. Bernards, *Wettability and Aging of Polymer Substrates after Atmospheric Dielectrical Barrier Discharge Plasma on Demand Treatment.* Journal of Imaging Science and Technology, 2013. **57**(3): p. 30503-1.
8. Verkuijlen, R., M. van Dongen, A. Stevens, J. van Geldrop, and J. Bernards, *Surface modification of Polycarbonate and Polyethylene Naphtalate Foils by UV-Ozone treatment and µPlasma Printing.* Applied Surface Science, 2013.
9. Chin, C.D., V. Linder, and S.K. Sia, *Lab-on-a-chip devices for global health: past studies and future opportunities.* Lab on a Chip, 2007. **7**(1): p. 41-57.
10. Weigl, B.H., R.L. Bardell, and C.R. Cabrera, *Lab-on-a-chip for drug development.* Advanced drug delivery reviews, 2003. **55**(3): p. 349-377.
11. Whitesides, G.M., *The origins and the future of microfluidics.* Nature, 2006. **442**(7101): p. 368-373.
12. Washburn, E.W., *The Dynamics of Capillary Flow.* Physical Review, 1921. **17**(3): p. 273-283.
13. Pleshek, J. *RFID and bar codes: from competitors to teammates*. WTN NEWS, 2011.
14. Shepard, S., *RFID: radio frequency identification*. 2005: McGraw-Hill New York.
15. Rida, A., L. Yang, and M.M. Tentzeris, *RFID-Enabled sensor design and applications*. 2010: Artech House.
16. Staelin, D., *Antennas.* 2013: p. 72.
17. Semiconductors, N., *SL3ICS1002/1202 Product data sheet COMPANY PUBLIC*, in *UCODE G2XM and G2XL*, NXP, Editor. 2011.

18. Nikitin, P.V., K.S. Rao, R. Martinez, and S.F. Lam, *Sensitivity and impedance measurements of UHF RFID chips.* Microwave Theory and Techniques, IEEE Transactions on, 2009. **57**(5): p. 1297-1302.
19. iDTRONIC, *USB Stick Reader EVO*. 2012, iDTRONIC.
20. Weltjens, W., *RFID antenna design and tag assembly.*, in *Expertise centre Thin Films and Functional Materials*. 2014, Fontys University of Applied Science: Eindhoven.
21. Mies, M., *Printed RFID-Tag Assembly and Optimization*, in *Expertise centre Thin Films and Functional Materials*. 2014, Fontys University of Applied Science: Eindhoven.
22. MacDiarmid, A.G., *"Synthetic metals": A novel role for organic polymers (Nobel lecture).* Angewandte Chemie International Edition, 2001. **40**(14): p. 2581-2590.
23. Bai, H. and G. Shi, *Gas sensors based on conducting polymers.* Sensors, 2007. **7**(3): p. 267-307.
24. Gupta, N., S. Sharma, I.A. Mir, and D. Kumar, *Advances in sensors based on conducting polymers.* J. Sci. Ind. Res, 2006. **65**: p. 549-557.
25. Nicolas-Debarnot, D. and F. Poncin-Epaillard, *Polyaniline as a new sensitive layer for gas sensors.* Analytica Chimica Acta, 2003. **475**(1-2): p. 1-15.
26. Agbor, N., M. Petty, and A. Monkman, *Polyaniline thin films for gas sensing.* Sensors and Actuators B: Chemical, 1995. **28**(3): p. 173-179.
27. Wu, G. and H. Zhang, *Synthesis and Characterization of Camphor Sulfonic Acid Fully Doped Polyaniline.*
28. MacDiarmid, A.G. and A.J. Epstein, *Secondary doping in polyaniline.* Synthetic Metals, 1995. **69**(1): p. 85-92.
29. Kahol, P., A. Dyakonov, and B. McCormick, *An electron-spin-resonance study of polyaniline and its derivatives: polymer interactions with moisture.* Synthetic metals, 1997. **84**(1): p. 691-694.
30. Lizarraga, L., E. María Andrade, and F. Victor Molina, *Swelling and volume changes of polyaniline upon redox switching.* Journal of Electroanalytical Chemistry, 2004. **561**: p. 127-135.
31. Tobolková, E., J. Prokeš, I. Křivka, M. Trchová, and J. Stejskal, *Temperature- and humidity-related degradation of conducting polyaniline films.* Macromolecular Symposia, 2004. **212**(1): p. 447-454.

# 5 Concluding Remarks and Outlook

We started this thesis by introducing two topics concerning the deposition of functional materials for printed electronics. As the term printed electronics implies, functional materials are printed via, e.g. inkjet, flexo or gravure printing techniques, on to a substrate material. Applications are, among others organic light emitting diodes (OLED), sensors and radio frequency identification (RFID) tags and Lab-on-a-chip devices. For all these applications, in some way, the interaction of fluids with the substrate is of great importance. Control and understanding of wetting behaviour of liquids on the substrate, as well as liquid-liquid interaction is necessary in order to develop applications. Localized control of wettability was investigated using the novel µPlasma patterning technology. The interaction of two merging droplets of different volume ratios and/or compositions was studied, to gain a better understanding in the coalescence dynamics on the internal mixing of the two droplets. In this final chapter, we will look back on these two topics and briefly summarize the main conclusions and picture potential outlook toward future applications.

## 5.1 µPlasma Patterning

In chapter two, µPlasma patterning was introduced as a technology to selectively and locally treat the surface of a substrate with an atmospheric dielectric barrier discharge. Using the µPlasma patterning tool, we were able to functionalize the surface of the substrate, e.g. glass or polymer films, in such a way that areas of high and low wettability could be created on demand. A minimal resolution of 300 µm in diameter for a single pixel wide line was achieved using a POD24 plasma head with a needle diameter of 200 µm. We also showed that by varying the composition of the plasma gas, different effects on the surface could be reached. Using air as plasma gas, oxygen containing groups were incorporated in the top molecular layers of the substrate surface of polymer films. The incorporation of these groups leads to in an increase of the surface energy of the polymers, causing a broadening in the wettability envelope for liquids deposited on the surface. Five days after treatment the surface energy of the examined polymers had reverted to roughly 50% of the original change due to the treatment, remaining at that

level for at least 30 days afterwards. Even though the µPlasma tool works in an open to air environment at atmospheric pressure, different gasses and pre-cursor materials can be added to the plasma gas. This in turn changes the reactivity and effects of the plasma treatment. By adding hexamethyl-disiloxane (HMDSO) vapour to nitrogen, siloxane layers were successfully deposited on the surface of PC films as was confirmed by ATR-FTIR and XPS analysis. As a result of the deposition, the wetting envelope of the HMDSO-layer on PC-films was significantly smaller when compared to untreated PC.

In general, µPlasma patterning has proven to be an interesting new technology to locally treat the surfaces of materials which can be utilized in the development for a large variety of applications within the printed electronics market. The biggest advantage of the µPlasma tool, as compared to more conventional plasma tools, is the combination of the plasma tool with a digital printing platform. This enables the operator, to quickly change the plasma patterned area by just changing a bitmap image. Also the versatility in plasma gas composition creates a wide range of options in future applications. The potential in locally changing the wettability of substrates can be of great interest for printed electronics, especially if the resolution of the pattern is in the order of a millimetre. Smaller resolutions, however would ask for a more precise plasma head and control of plasma conditions to be sufficiently accurate. Also other types of applications are possible with the addition of pre-cursor materials in the plasma gas. Dependent of the gas composition, different functionalities can be added to the substrate. Applications could include for instance, the local deposition of sensing materials in Lab-on-a-chip devices. With the large interest in new innovative point-of-care applications this could be an interesting route for µPlasma patterning in the future.

## *5.2 Coalescence and mixing of small droplets*

In printing applications, coalescence of droplets is standard practice as consecutive droplets are printed onto, or close to each other. Understanding the behaviour of these droplets upon coalescence is therefore important, especially if the ink droplets are of different composition and/or volume. In case of different compositions, internal transport of the ink components can take place over time, either driven by convective, due to merging, or diffusive flows, due to concentration gradients inside the merged droplets. Gaining knowledge of the duration and intensity of these flows can be important in the development of specific kind of printing applications, like for instance in reactive or colour printing. In chapter 3, the time evolution of two coalescing droplets was investigated. For relatively large equally sized silicone droplets, the time evolution of the coalescence bridge was found to scale with a power law coefficient of 0.5. This is in good agreement

with current literature. For smaller inkjet printed droplets, the internal flows during coalescence were visualized using fluorescent dyes for the volume ratios 1:1, 2:1 and 4:1. We found that for the equally sized droplets, the dye transport across the bridge was dominated by diffusion only. Fitting the experimental data of the dye transport to the 1D approximation of Fick's second law of diffusion over the length of the droplet showed excellent agreement. Contributions in the dye transport across the bridge by convective flows were cancelled out by droplet symmetry. For two coalescing droplets of different volumes, we experimentally found a significant contribution of the convective flows across the bridge. During the period that the bridge was widening, we found a substantial contribution of the convective flow in the dye transport from the small to the large droplet. This convective flow from the small into the large droplet was also found to increase in size for increasing volume ratios. Also a small convective flow from the large into the small droplet was identified. The origin of this flow might be due to the presence of vortices along the interface of the bridge, due to the strong flow to create the bridge. Further investigation to study this phenomenon is recommended. After the initial bridge formation, we showed that the convective flows stop as the bridge stops growing. From this moment, the dye transport is governed by diffusion. Numerical simulations in Comsol Multiphysics of the dye transport in the small inkjet printed droplets were also performed to verify the experimental results. Although the time evolution of the droplet shapes showed good reasonable agreement, two differences stood out. First, the bridge evolved in the simulation approx. 10 times faster in comparison to the experiments. Second, the bridge continued to grow until a hemispherical drop was achieved. From a pressure, i.e. surface tension, driven point of view this is as expected. However, in the actual experiments the bridge expansion is slowed and stopped due to the viscous behaviour of the liquid. In order to track the time evolution of the (simulated) dye transport across the bridge, the droplet shape was pinned at $10^{-4}$ s. Using this adaptation, the dye transport could be reasonably described in comparison with the experiments for both the equally and unequally sized droplets. Still, a single numerical simulation over the complete time range, which describes the droplet shape evolution correctly, was not obtained.

Although the subject of mixing within the droplets has become more of academic interest during this doctoral study, the basic problem originated from a practical application. In this application, the goal was to create a controlled concentration gradient in deposited material via inkjet printing. Although, differences between the application and this experimental work exist, looking back we can conclude the following. Even though the surface tension induced flows have a large impact on the final shape of the coalescing droplets, the material transport across the bridge is primarily governed by

diffusion. In the relatively simple case of the presented experiment, with a non-evaporating solvent, following the concentration gradient was achievable. In the complex inks, used in printed electronics of the original application, the solvent evaporates, pinning the solutes on the substrate. In order to be able to control the deposition along the coalescing drop, a good understanding of the diffusion coefficients of the solute in relation to the evaporation rate of the solvent is needed, as well as other influencing aspects like e.g. the coffee stain effect.

# *Summary*

In the development of applications for printed electronics, the interaction of fluids with substrates is of great importance. Control and understanding of the wetting behaviour of fluids on substrates, as well as fluid-fluid interaction on the substrate is necessary to develop new applications. This thesis represents the work done on two topics concerning the deposition of functional materials for printed electronics. In the first topic, we discuss a novel plasma patterning technology. This technology enables selective and localized plasma treatment on a wide range of substrate materials by combining plasma treatment with digital printing. In the second topic, the coalescence of droplets on a (partially) wettable substrate is investigated. The thesis ends with a showcase of potential applications of the µPlasma patterning and inkjet printing. Below, the most important conclusions are summarized.

Plasma technology has had a long history in treating materials in order to improve wetting or promote adhesion. Most plasma applications, however, are only able to treat the complete surface of a substrate. The µPlasma patterning tool described in this thesis combines a digital inkjet printing platform with an atmospheric dielectric barrier discharge plasma tool. The versatility of the digital printing platform combined with the plasma tool, allows for selective and local plasma treatment, at atmospheric pressure, of substrates without the use of any masking materials. Also the ease in changing the plasma gas composition makes it possible to switch, without much effort, from plasma functionalization to plasma deposition. With air as plasma gas, we found that the surface energy of all tested polymer films, i.e. PC, PET, PEN, PI and FEP, substantially increased after plasma treatment for up to 4-5 identical treatments. Further treatments showed no additional effect on increasing the surface energy. The changes in surface energy were mainly due to a strong increase in the polar part of the surface energy, and a small decrease in the dispersive part. Surface analysis of µPlasma treated PC and PEN films by ATR-FTIR and XPS showed an increase in oxygen containing groups incorporated on the surface and a decrease in aromatic bonds on the surface with increasing intensity of the

treatment. In comparison with UV-ozone plasma treatment, we found that µPlasma patterning is less aggressive in attacking the aromatic bonds and incorporates less oxygen containing groups on the surface. Apart from FEP, after one month of storage, the µPlasma treated polymer films lost approximately 50% of the change in surface energy. The majority of this loss was already reached in the first 5 days. FEP, however, showed only little recovery in surface energy after one month of storage. By changing the gas composition being fed to the µPlasma tool, also deposition of materials on the surface is possible. We investigated the addition of hexamethyl-disiloxane (HMDSO) precursor to nitrogen in the plasma gas. Plasma deposition of HMDSO leads to the formation of silicon dioxide layers on the surface. By ATR-FTIR and XPS analysis of µPlasma treated PC, the presence of silicone dioxide layers on the surface were detected, whereas peaks of the original surface material (PC) in the spectra became less pronounced with increasing number of treatments. The surface energy of PC films was also substantially lowered, reducing the wetting envelope considerably. The maximum change in the surface energy was reached after 2 treatments. In contradiction to air plasma treatment, the dispersive part of the surface energy was lowered, whilst the polar part remained the same. This verifies the difference in chemical activity of the plasma gasses. On glass, deposition of HMDSO changed the contact angle of water from less than 5 degrees to over 90 degrees. Localized changes in wettability were achieved by utilizing the µPlasma tool together with the digital printing platform on which the tool was mounted. A range of bitmap images were used to create µPlasma patterns on the substrate in order to investigate the smallest resolution in wettability changes. For a single µPlasma treatment of a one pixel wide line, patterned with a discharge gap of 75 µm, the smallest resolution of 300 µm wide was achieved.

Overall, µPlasma patterning shows promise as a surface treatment tool in the development for a large variety of applications. The biggest advantage of the µPlasma tool, as compared to more conventional plasma tools, is the ability to locally treat substrates without the need for masking materials. In applications where local control of wettability is of importance, like e.g. inkjet printing, the plasma patterning capability can contribute to the enhancement of the resolution of the deposited materials, though it is advised to further decrease the minimum patterning resolution. The option to deposit materials to the surface by changing plasma gas composition creates a new range of potential applications. Dependent of the gas composition, different functionalities can be added to the substrate.

Next to the control of wettability of an ink on a substrate in printed electronics is the interaction of ink droplets with themselves of importance. In printing applications, coalescence of droplets is standard practice as consecutive droplets are printed onto, or close to each other. Understanding the behaviour of these droplets upon coalescence is therefore important, especially when the ink droplets are of different composition and/or volume. In case of different compositions, internal transport of the ink components can take place over time, either driven by convective, due to merging, or diffusive flows, due to concentration gradients inside the merged droplets. Gaining knowledge of the duration and intensity of these flows can be important in the development of specific kind of printing applications, like for instance in reactive or colour printing. We started the investigation in the coalescence dynamics by studying relatively large silicone droplets merging on a fully wettable glass substrate. The time evolved radius of the bridge was found to scale with a power law coefficient of 0.5, which is in agreement with previous findings in literature. Next the internal flows of merging small inkjet printed droplets were investigated. By adding different fluorescent dyes to each of the two droplets, the internal transport of the dye could be tracked over time as the droplets coalesce distinguishing between contributions due to convective and diffusive based material flows. Coalescence of the inkjet printed droplets was initiated by exposing the substrates and droplets to UV-light. For droplets of equal volume, it was found that the dye transport across the bridge could be fully described by diffusion only. This is as expected, as due to the droplet symmetry on either side of the bridge, the convective flows towards the bridge are of equal size but opposite in direction. Consequently, at the bridge the net convective contribution to the dye transport is expected to be zero and the dye transport across the bridge is fully dominated by diffusion. For droplets with volume ratios of 2:1 and 4:1, symmetry across the bridge is no longer present. Pressure differences between the small and large droplet are anticipated to generate a surface tension driven convective flow across the bridge upon coalescence, especially in the early stages as the coalescence bridge widens. Experimental analysis of merging droplets of unequal volume confirmed this hypothesis as well. In the early stages, a significant contribution of convective based dye transport was successfully identified directly after the formation of the bridge. This flow was largest from the small to the large droplet. Also, a small convective flow of shorter duration from the large into the small droplet was identified. The origin of this flow might be due to the presence of vortices along the interface of the bridge, due to the strong transverse flow to open the bridge. Further investigation on this phenomenon is recommended. After the initial fast bridge formation as the curvature becomes less, viscous forces slow the widening of the bridge and eventually the bridge stops expanding. At this point the convective flows within the droplet cease, and the dye transport is

further governed by diffusion. Comparison of the experimental data with a 1D approximation of Fick's second law of diffusion across the bridge supports this finding. Numerical simulations in Comsol Multiphysics of the dye transport in the small inkjet printed droplets were also performed to understand the experimental results. Although the time evolution of the droplet shapes showed good reasonable agreement, two differences stood out. First, the bridge evolved in the simulation approx. 10 times faster in comparison to the experiments. Second, the bridge continued to grow until a hemispherical drop was achieved. From a pressure, i.e. surface tension, driven point of view this is as expected. However, in the actual experiments the bridge expansion slows and eventually stops as mentioned above. In order to track the time evolution of the (simulated) dye transport across the bridge comparably to the experiments, the droplet shape was therefore pinned at $10^{-4}$ s. Using this adaptation, the dye transport could be reasonably described in comparison with the experiments for both the equally and unequally sized droplets. Still, a single numerical simulation over the complete time range, which describes the droplet shape evolution correctly, was not obtained.

To conclude, three potential applications were showcased. In the first application we used µPlasma patterning to create hydrophilic patterns on hydrophobic dodecyl-trichlorosilane (DTS) covered glass. Capillaries for a Lab-on-a-chip device were successfully created by placing two µPlasma patterned glass slides on top of each other separated by scotch tape. In the second application we showcased the production of a RFID tag via inkjet printing. Functional RFID-tags on paper were created via inkjet printing of silver nanoparticle ink connected to an integrated circuit. The optimal operating frequency of the produced tags is in the range of 860-865 MHz, making them usable for the European market, although the small working range of 1 m needs further improvement. Lastly, we showed the production of a chemresistor based gas sensor. In house synthesised polyemeraldine salt (PANi) was coated by hand on top of inkjet printed silver electrodes. The sensor proved to be equally sensitive to ethanol and water vapour, reducing its selectivity in detecting changes in gas composition.

# *Samenvatting*

De interactie van vloeistoffen met substraten is een belangrijk aspect in de ontwikkeling van toepassingen voor geprinte elektronica. Het begrijpen en sturen van het vloeigedrag van vloeistoffen op substraten, alsmede de interactie tussen de vloeistoffen onderling op een substraat is noodzakelijk om nieuwe toepassingen te kunnen ontwikkelen. In dit proefschrift worden twee onderwerpen behandeld die te maken hebben met het gestuurd deponeren van functionele materialen voor geprinte elektronica. In het eerste deel, wordt een nieuwe plasma techniek besproken, waarmee het mogelijk is om selectief en plaatselijk substraten te behandelen door plasma behandeling aan digitale print technologie te koppelen. In het tweede deel wordt het samenvloeien van druppels op gedeeltelijk bevochtigende substraten onderzocht. Het proefschrift eindigt met een aantal voorbeelden van toepassingen van gepatroneerd plasma behandelen en inkjet printen. De belangrijkste conclusies uit het proefschrift worden hieronder samengevat.

Plasma technologie heeft een lange historie in het verbeteren van het vloei- en hechtingsgedrag van materialen. De meeste plasma toepassingen behandelen hierbij het totale oppervlak van het substraat, slechts enkele zijn in staat om plaatselijk oppervlakken te behandelen. De µPlasma techniek, combineert de veelzijdigheid van een digitaal print platform met plasma behandeling. Hierdoor wordt het mogelijk om selectief en plaatselijk, onder atmosferische druk, substraten met plasma te behandelen zonder gebruik te hoeven maken van maskers. Daarnaast biedt de µPlasma techniek ook de mogelijkheid om eenvoudig van gas samenstelling te veranderen. Naast activering van het oppervlak, is het hierdoor ook mogelijk om materiaal op het substraat aan te brengen. Door het gebruik van een lucht plasma neemt de oppervlakte-energie van alle geteste polymere folies, i.e. PC, PET, PEN, PI en FEP, significant toe na behandeling. Na 4-5 opeenvolgende plasma behandelingen wordt een maximum in de oppervlakte-energie bereikt. De toename van de oppervlakte-energie is voornamelijk een gevolg van de toename van het polaire deel gekoppeld aan een kleine afname in het dispersieve deel van de oppervlakte-energie. ATR-

FTIR en XPS analyses van het oppervlak, van met plasma behandelde PC en PEN folie, laten zien dat er een duidelijke toename is in het aantal zuurstofhoudende groepen en een afname in aantal aromatische verbindingen met toenemend aantal µPlasma behandelingen. µPlasma behandeling blijkt, in verhouding met een UV-ozon behandeling, minder zuurstof groepen te vormen en minder aromatische verbindingen te verbreken op het oppervlak van PC en PEN. Hierdoor lijkt de µPlasma behandeling iets milder te zijn in vergelijking met UV-ozon. Uitgezonderd FEP-folie, blijken de behandelde polymeer folies na een maand opslag circa 50% van de verandering in oppervlakte-energie weer te hebben verloren. Het grootste deel van deze terugval is al in de eerste vijf dagen bereikt. FEP-folie laat na een maand opslag deze terugval in oppervlakte-energie niet zien. Met het gebruik van andere gassamenstellingen dan lucht, kan het µPlasma tool ook gebruikt worden voor het deponeren van functionele materialen op een substraat. Door toevoeging van hexamethyl-disiloxane (HMDSO) als precursor aan stikstof in het plasmagas kunnen lagen van siliciumdioxide op het substraat worden aangebracht. ATR-FTIR en XPS oppervlakte-analyses van PC-folie behandeld met HMDSO hebben aangetoond dat deze siliciumdioxide lagen ook daadwerkelijk zijn gevormd op het oppervlak, deels doordat in de spectra de aanwezigheid van siliciumoxide is aangetoond, maar ook doordat het originele spectrum van PC zwakker wordt. De µPlasma behandeling met HMDSO zorgt voor een duidelijke verlaging van de oppervlakte-energie, waarbij de maximale verandering al naar twee behandelingen is bereikt. De verlaging is voornamelijk gerelateerd aan een vermindering in het dispersieve deel, terwijl het polaire deel van de oppervlakte-energie gelijk blijft. Dit is duidelijk afwijkend met een lucht plasma behandeling, waarmee het verschil in chemische activiteit tussen de verschillende plasma gassen duidelijk zichtbaar is. Op glas zorgt plasma depositie van HMDSO voor een verhoging van de contacthoek van minder dan 5 graden voor behandeling, tot een contacthoek van groter dan 90 graden na behandeling. Plaatselijke veranderingen in bevochtiging op substraten zijn bereikt door gepatroneerd substraten te behandelen met behulp van het digitale printplatform waarop het µPlasma tool is gemonteerd. Middels een serie van digitale afbeeldingen kunnen verschillende patronen met verschillende resoluties op substraten worden aangebracht. De kleinste resolutie van een enkele pixel brede lijn is 300 µm breed op het substraat. Hiervoor is het substraat eenmaal behandeld met een plasma ontladingsafstand van 75 µm en een enkele behandeling.

Over het geheel genomen blijkt µPlasma printen een interessante ontwikkeling te worden voor het ontwerpen van nieuwe toepassingen voor geprinte elektronica. Het grootste voordeel van µPlasma printen, in vergelijking met conventionele methoden, is de mogelijkheid om substraten plaatselijk zonder gebruik van maskers te kunnen

behandelen. In toepassingen waar sturing van plaatselijke verschillen in bevochtiging van belang zijn, zoals bv. inkjet printen, zijn de patroneringsmogelijkheden van deze tool van meerwaarde. Daarbij is het echter wel gewenst om te onderzoeken of de minimale resolutie nog verder omlaag kan worden gebracht. De optie om flexibel met andere gassamenstellingen te kunnen werken om bijvoorbeeld lagen te deponeren biedt de ruimte om nieuwe toepassingen te ontwikkelen, waarbij nieuwe functionaliteiten op het substraat worden toegevoegd.

Naast de controle over de bevochtiging van een inkt op een oppervlak, is tevens de interactie van inktdruppels met elkaar van belang bij de ontwikkeling van geprinte elektronika. In printtoepassingen, worden vele opeenvolgende kleine druppels vaak dicht naast, of op elkaar geprint waarbij ze al of niet samenvloeien. Het begrijpen van de processen die plaatsvinden tijdens dit samenvloeien zijn belangrijk, zeker als het gaat om druppels van ongelijke grootte of verschillende samenstellingen. In het geval van verschillende samenstellingen, zullen de componenten in de inkten zich in de tijd in de samengevloeide druppel verspreiden. Dit kan zowel plaatsvinden door convectieve stroming, veroorzaakt door het samenvloeien van de druppels, als ook door diffusie, middels aanwezige concentratie verschillen. Voor specifieke printtoepassingen, zoals het deponeren van reactieve materialen of kleuren, kan het begrijpen van de duur en intensiteit van deze stromingen van grote waarde zijn. In het tweede deel van dit onderzoek zijn we begonnen met het kijken naar het samenvloeien van relatief grote druppels siliconenolie op een volledig bevochtigend glazen substraat. De groei van de brug tussen twee samenvloeiende druppels blijkt goed te kunnen worden beschreven met een wortelfunctie in de tijd. Dit is in goede overeenstemming met literatuurreferenties. Vervolgens is gekeken naar het tijdsafhankelijke transport van opgeloste fluorescente kleurstoffen in kleine samenvloeiende druppels. De druppels zijn door middel van inkjet printen dicht naast elkaar op glazen substraten geprint, waarna middels UV-belichting het samenvloeien van de druppels is geïnitieerd. Bij druppels met gelijk volume blijkt dat de het transport van de kleurstof over de brug volledig met diffusie kan worden verklaard. Gezien de symmetrie van de samenvloeiende druppel over de brug, is dit zoals verwacht, aangezien de convectieve stromingen gelijk van grootte zijn, maar tegengesteld in richting. Op de brug heffen ze elkaar dan ook op en is het transport van de kleurstof over de brug volledig door diffusie gedomineerd. Voor druppels met een volumeverhouding van 2:1 en 4:1 is deze symmetrie niet meer aanwezig. Door het interne drukverschil tussen de kleine en grote druppel wordt er een netto convectieve stroming verwacht van de kleine naar de grote druppels op het moment van samenvloeien. Experimentele analyse van samenvloeiende druppels met ongelijke volumina bevestigen dit. In het eerste moment na

coalescentie wordt een significante bijdrage aan het transport van de kleurstof waargenomen van de kleine naar de grote druppel. Daarnaast is er tevens een kleine, korter durende stroom van de grote naar de kleine druppel. De oorzaak van deze stroming ligt mogelijk in de aanwezigheid van wervelingen op het grensvlak tussen de twee druppels op het moment dat de druppels samenvloeien als gevolg van de sterke stromingen tijdens het vormen van de brug. Verder onderzoek naar dit verschijnsel is wenselijk. Na de initiële snelle vorming van de brug, neemt de groeisnelheid af doordat de kromming van de brug kleiner wordt en de relatieve invloed van de viscositeit toeneemt. Uiteindelijk zal hierdoor de brug stoppen met groeien en de convectieve stromen nul worden. Vanaf dat moment kan het transport van de kleurstof over de brug goed met een 1D vereenvoudiging van de tweede wet van Fick worden beschreven. Om de experimenten van het transport van de kleurstof beter te begrijpen zijn tevens numerieke simulaties met Comsol Multiphysics in de kleine samenvloeiende druppels in 3D uitgevoerd. Ondanks dat in de simulatie de druppelvorm redelijk overeen kwam in de tijd met de experimenten, vielen er twee aspecten op. Ten eerste, de simulatie voorspelt de vorming van de brug een factor 10 sneller dan de experimenten. Ten tweede, groeit de brug door tot een ronde druppelvorm op het substraat is verkregen. Ondanks dat dit door de oppervlaktespanning aanwezige drukverschillen modelmatig correct is, komt dit niet overeen met de experimenten. De viskeuze effecten, waardoor de bruggroei in de experimenten stopt, worden door de numerieke simulatie niet correct berekend. Om het transport van de kleurstof alsnog vergelijkbaar te kunnen modelleren met de experimenten, is om deze reden in de simulatie de druppelvorm vastgezet op $10^{-4}$ s. Met deze aanpassing kon vervolgens succesvol, en vergelijkbaar met de experimenten, het transport worden beschreven voor zowel de druppels van gelijke en ongelijke grootte. Eén complete simulatie over het volledige tijdsrelevante gebied kon echter niet worden gerealiseerd.

Tenslotte zijn er drie potentiele toepassingen van µPlasma patroneren en inkjet printen behandeld. In het eerste voorbeeld, wordt µPlasma patroneren gebruikt om hydrofiele sporen te maken op met dodecyl-trichlorosilaan (DTS) hydrofoob gemaakt glas. Glasplaatjes met daarop deze sporen zijn vervolgens op elkaar geplaatst om een voorbeeld van een “Lab-on-a-chip” device te maken. Als tweede voorbeeld zijn functionerende RFID-tags geproduceerd met behulp van inkjet printen. De RFID-tags zijn geproduceerd door antennes van zilver-nanoinkt te printen op papieren substraten. Op de antenne werd vervolgens een IC geplaatst. Het optimale werkgebied van de antennes ligt in het frequentiegebied van 860-865 MHz. Hierdoor zijn ze potentieel bruikbaar op de Europese markt, al vraagt de werkafstand van 1 meter nog verdere optimalisatie. In het

laatste voorbeeld presenteren we een gassensor. De sensor bestaat uit twee inkjet geprinte zilver elektroden waarop een polyemeraldine zout (PANi) is aangebracht. De sensor blijkt even gevoelig te zijn voor waterdamp en ethanol.

# *Acknowledgements*

In the years I've worked at the Fontys University of Applied Sciences, I'd always been pleasantly surprised at the nice working atmosphere. Although, it can be very hectic environment with numerous "important" things happening at the same moment, it is never dull and there is always time to get some new perspectives at the 040. For this, I would like to thank first and foremost all my colleagues and the students from "Toegepaste Natuurwetenschappen".

I would like to thank Marthie Meester as my former director, as initiator to start my PhD after having worked for a couple of years as an educational developer. She convinced me to return to my roots as chemical engineer. Also, during the PhD study she remained positive in me finishing it. Next I would like to thank Jan Bernards and Peter Ketelaars for both being my mentors at the Expertise Centre "Thin Films and Functional Materials". Their involvement and support in this project were motivated by genuine interest in the topics of this thesis. I'm grateful for the many fruitful discussions in helping to solve many of the challenges posed along the way. Also, I appreciate their genuine concerns to guard me from giving too many classes in order to spend more time on my thesis. The other members and former members of the Expertise Centre I would like to thank as well. Jan van Lierop for his handy work as well as taking over practical courses. Renee Verkuijlen, Roel Aben, Tim Beekman, Antje van de Berg, Jan van Geldrop, Gerard Brands, Roeland van Klinken, Jacomien Brocaar and Willie van Helvoort-Hardeman for their insight, discussions, experimental work and pleasant working atmosphere. For the discussions and help with the numerical simulations in Comsol, I would like to thank Helger Halewijn. I would like to thank the members of the IBIS team of which I have become part in the last year. Their support for me to keep my work place at the expertise centre, enabled me to finalize this project whilst still making me feel part of the team.

Of course, I would like the many students, who over all these years, contributed in some way to parts of the experimental and theoretical work behind this thesis, in no particular order, Guido van Rooij, Jasper Nab, Tijm de Wild, Tom Vercoulen, Tom Verstraaten, Rendy Nieuw, Koen van de Wiel, Merel Eland, Richard van Hout, Erik

Nieuwenhuis, Richard Janssen, Rene de Lepper, Stefan Vermeer, Kevin van de Wiel, Andreas van Loon, Swen Doesburg, Harald Emmers, Patrick Gerris, Guus Hutschemakers, Lise Verbraeken, Wim Weltjens, Robbert Nagelkerke and Maarten Mies as well as the many more student who did their internship at the Expertise centre during this period for their nice collaborations.

I would like to especially thank Frits Dijksman for becoming my promotor in the last six months. His vast experience in inkjet was very helpful in understanding the coalescence of droplets. Also without his support, I wouldn't have been able to finish this thesis.

From the TU/e and Friedrich Schiller Universität in Jena, I would like to thank Ulrich Schubert for being my promotor during a long period of my studies. Unfortunately, we were not able to finish is to the end. I would like to thank the members of the inkjet group for the many fruitful discussions. Especially, Jolke for always being helpful when needed

For the funding of this project, I would like to thank Fontys Hogescholen and the Stichting Innovatie Alliantie within the Raak Pro project "Inkjet printtechnologie voor het MKB".

I would like to thank Robert Vrancken from Validus for introducing the secretive mixing of droplets problem to me. What seemed to be a simple problem to investigate soon appeared to be very elusive to reproduce. When we were finally able to recreate and trace the mixing of the dyes, his drive and interest in the understanding the topic was inspiring.

I would like to thank Innophysics for the introduction of the µPlasma printer. Alquin and Peter, thank you for the many discussions about plasma printing. Also, you were always ready to support when something went wrong with the printer or have some students come to do experiments.

I would like to thank the people from Roth and Rau, Pixdro for their help with the LP50 inkjet printer. Also Wouter and Joost , currently working at PixDro, but whom I learned to respect from Innophysics and Neodec. Their sharing of knowledge on plasma, wetting and inkjet in the many discussions were always helpful.

And of course, thank you Huub, Rommert, Rene, Adri, Jan, Ad, Atze, Ilona, Hein, Jan, Ton and all the others of Falcon Air, for the joint time in the air and the pleasant get-togethers and friendship at the field.

Tijdens mijn promotie was mijn familie een grote steun voor mij, ook al liet ik zo nu en dan wel eens een verjaardag schieten. Ik wil mijn ouders, mijn zus en broer en hun gezinnen speciaal bedanken voor hun geduld en steun. De rest van de familie wil ik graag bedanken voor hun oprechte interesse.

# *About the Author*

Martijn van Dongen was born on March 16, 1970 in Eindhoven to Ad and Nannie van Dongen-Wijn. In 1988, he joined the Eindhoven Technical University to study chemical engineering. For his master thesis he investigated the influence of an inhomogeneous electric field on drop formation and material transfer in a modified bubble column and graduated in 1994. After military service, in 1995 he joined Philips Research and worked on the development of polymer masking materials on glass to prevent damage due to powder blasting. From 1997 and onwards, he is working at Fontys University of Applied Sciences. Here, he is working as lecturer in chemical engineering and physics courses. He has been involved in the development of the Applied Science studies from 2000 to 2003. During this period, on a national level, he was one of the authors of the national competence profiles for the bachelor of chemical engineering and applied science degrees which is still being used up to this day. In 2003, he joint a team to help the reorganisation of the technical studies, Engineering, ICT and technical business management within Fontys from an educational point of view. Since 2008, he re-joined the department "toegepaste natuurwetenschappen" as lecturer for the Applied Science and Applied Physics studies, as well as researcher at the expertise centre "Thin film and Functional materials" as part of his PhD project. The PhD project resulted in a study on µPlasma patterning and inkjet printing. On these topics, articles have been published in scientific journals and have been presented on international congresses.